Etude du noyau très riche en neutrons 10He par réaction de transfert d'un proton 11Li(d,3He)

Adrien Matta

Université Paris-Sud XI

Institut de Physique Nucléaire d'Orsay

Ecole Doctorale Particules, Noyaux, Cosmos

Specialité Physique Nucléaire

THÈSE

Soutenue le 27 Fevrier 2012
par

Adrien MATTA

pour l'obtention du grade de
Docteur en Sciences de l'Université Paris-Sud XI

Study of the very neutron-rich ^{10}He by one-proton transfer reaction ^{11}Li(d,^{3}He)

Directeur de thèse : Didier Beaumel (IPN Orsay)
Co-Directeur de thèse : Takashi Nakamura (Tokyo Institute of Technology)

Composition du jury :

Président du jury	Pr. Pierre Desesquelles	CSNSM - Université Paris-Sud XI
Examinateur	Dr. Nicolas Alamanos	CEA Saclay
Rapporteur	Dr. Nigel Orr	LPC Caen
Rapporteur	Dr. Wilton Catford	University of Surrey (United Kingdom)
Co-Directeur	Pr. Takashi Nakamura	Tokyo Institute of Technology (Japan)
Directreur	Dr. Didier Beaumel	IPN Orsay

Contents

Aknowledgment

The three years and half of my PhD, and the eight years I spend at the university, were rich of social interaction with many remarkable people I would like to thanks in this preamble.

First I would like to thanks my PhD supervisor, Didier, for the opportunity he gave me. This PhD between two countries was an amazing experience on the human side. I also enjoy the great freedom he gave me to overwhelm all the challenges that constitute a PhD. Of course I did not only work with one person at IPN and found many great co-workers within my NESTER group. Among them I have a special thought for Laurence and her amazing availability for the annoying always late physicist I (and most of us) am when it come to prepare a mission. Speaking about IPN I am gratefull to Dominique and then Faiçal to welcome young students in there lab and spending a great deal of money for their formation in various schools and missions to let them present their new results themselves.

One of this school was of course the Geant4 school that play a decisive role in my PhD, leading to the birth of NPTool. This lead to my interaction with someone I would like to thanks deeply, Nicolas. I hope to continue interacting with you in the future, since you always shed light in such a striking yet full of wisdom manner on every problem. That depth of field and rigorous approach make you someone appreciable by far beyond the working area. In a similar way thanks to Fairouz and Pierre R. for their fruitful discussion and in-depth point of view on the physics and politics. Thank you to Marlene for her late notice correction of my manuscript and her effort to give me correction during the last weekend. I deeply appreciate your comments on my work. Thanks Jean-Antoine for his care about my future and his kindness.

I also thanks the other students and friends that were along during those years. Sandra, Baptiste, Simon, Jeremy and Freddy which I know since a long time now. Whatever path you choose in your personal and professional life I am confident in your success. Thanks to Pierre M., Laurent L. and Marine that are now experiencing the life of research. I have a special though for Alexis which shared all is experience with me while he was in his third year.

An important event, should I say collection of events, in my PhD was of course my one year stay in Japan. I thanks Nakamura san for welcoming me in his group at TITech. Japan was a brand new and challenging world for me and integration was sometime difficult. In the end it was a great experience that lead me to some introspection. I thanks Otsu san for his investment on the MUST2 campaign and

his help. Many thanks to the people from Nakamura lab and Mizuki san for their work on the cryogenic target. I thanks all the people I worked with at TITech and Riken for their help and support.

But this campaign would never be possible without my colleagues from CEA, and especially Valérie. I really enjoy working with you, and it was a great experience. I hope to mount experiments with you again in the future and go ahead to some drip-line nuclei. I should also thanks Laurent N. for all he teach me during the ^{14}O experiment at GANIL. The preparation in small community with Freddy is a great souvenir. I thanks Lolly for all the discussion on the electronic but mostly for his kind personality. Finally I thanks Alexandre for his straight to the point approach that thrill up all the online analysis I have done with him.

I thanks my jury for their careful reading of my work, their comments and remarks. I am especially grateful to Nigel and Wilton whose remark help me to get a more critical view on my results. Many thanks to Pierre D. who accepted to preside my jury and Nicolas for reading the manuscript in the very limited time I gave him.

Before all, a scientific carrier is made up of encounters and I would like to address a special thought to two people that fed up my research ambitions. Thank you to Azzedine and Birgit, working with you was decisive in my way of apprehending experimental physics and more generally research. I wonder how many people get the chance to meet twice in their life such great people. Thank you for you support and confidence. I would also thanks some of my teacher, and through them the whole teaching of my university. Thank you to Elias and Corrine for their contagious enthusiasm on sub atomic physics and thank you to Laurent A. for his wise teaching of C++.

The six months living at Komaba was a great experience where I met some very special people. I thanks Yannick and Xavier for our nights spend in the Shibuya karaoke, the swimming session followed by tabeodai shabushabu and all the small moment spend together from the kitchen of the 1st floor to the top of Kumotorisan. Thank you to Sandra, Doris and Ben for their support, you are all great people I enjoy to meet and wish all the best for you in the future.

Speaking about off work people I should thanks the WIPS team for their indefectible support in every situations. Our “Never swim alone” motto found all his sense during those years and I will remember for a long time the road trips to far off destinations.

Mes derniers mots, les seuls en français de ce manuscrit, s’adresseront à celle qui partage ma vie et qui m’a soutenue pendant trois ans, et ce même durant les longs mois passés loin d’elle. Merci du fond du coeur pour ton soutient.

Chapter 1

Motivations

During decades, physicist have studied only the stable or nearly stable nuclei available on earth. That fruitful study gave us models that describe well the three hundred and some nuclei that form the so-called valley of stability. The last 30 years, new techniques offered us the opportunity to study new nuclei and enlighten new phenomena, as the number of accessible nuclei grew from 300 to 3000. The short life times of these nuclei make impossible the realization of target. For this reason, physicists use the inverse kinematics, where the heavier and unstable beam is impinging onto a lighter stable target. The development of radioactive beams allows the test of our models on new degrees of freedom, such as isospin, representation of the asymmetry between protons and neutrons. In order to study these new nuclei with our range of well-known reactions, new detectors and new methodologies have been developed. If radioactive beams allow the study of very short lived nuclei, their intensity, many orders of magnitude lower than stable beams, is challenging our experimental methods. The direct reactions are one of this experimental method, where the nucleus of interest is formed in its ground state or an excited state, through a one step process. New detectors, such as MUST [BAS+99] and MUST2 [PBRC+05], dedicated to the study of direct reactions on light targets have been designed and used successfully during the last decade. Direct reactions give us information on various aspect of the studied nuclei, such as the matter density, through the proton scattering, and the energy and spin of excited state through inelastic scattering and transfer reactions. The experimental study of light nucleus is a key stone to test microscopic models. It is the part of the nuclear chart where the nucleus can be theoretically described using our very fundamental knowledge of the nucleon-nucleon interactions. Moreover, the drip-line, where nuclear binding energy vanishes, is accessible experimentally.

1.1 Physics of light neutron-rich nuclei near the drip-line

Physics at the drip-line offers the opportunity to study nuclei at the limits of the nuclear landscape, where additional protons or neutrons can no longer be kept in the nucleus. In the vicinity of the drip-lines, the structural features of the nuclei change with respect to the more stable nuclei, the normal shell closure of particles disappears and new phenomena appear, such as particle radioactivity and beta-delayed particle emission. Threshold effects such as the halo structures, discovered 20 years ago is a very interesting feature because of its consequences on the interplay between theory and experimental work during the last decades.

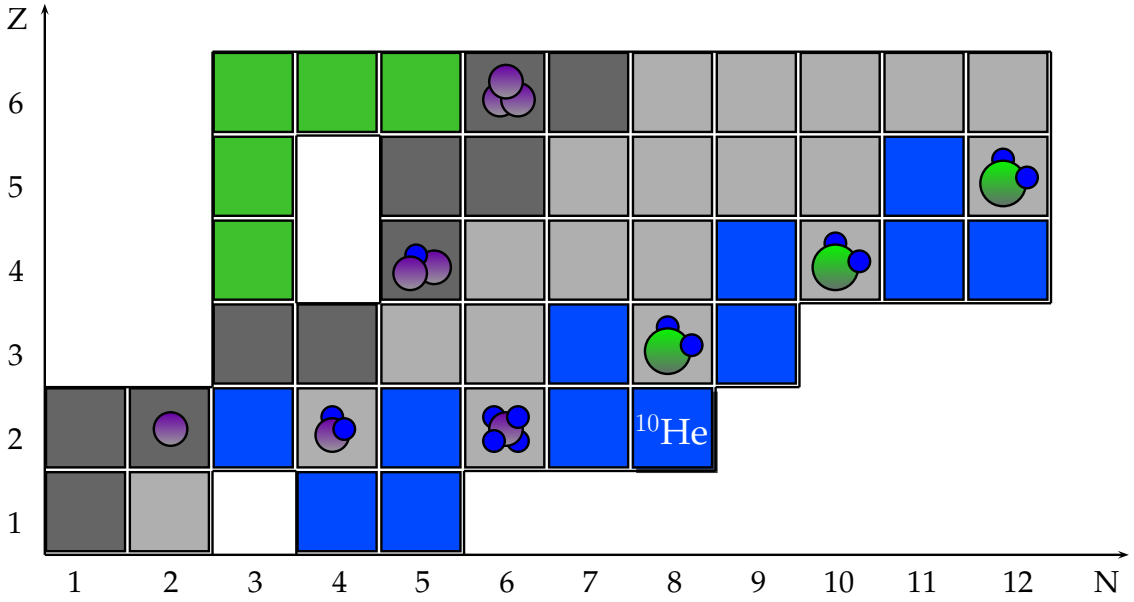

Figure 1.1: *Close-up view of the nuclei chart in the light nuclei region. This area of the nuclear chart exhibit various phenomena such as clustering and halo. Dark grey nuclei are stable nuclei, light grey and green ones are respectively β^- and β^+ unstable nuclei, while the blue one are neutron-rich resonances.*

1.1.1 Shell closure breakdown

One of the main features of the nuclei along the stability line is the nuclear shell structure and the associated *magic numbers*. This structure was successfully described after the work of by Maria Goeppert-Mayer, Haxel, Mayer, Suess and Jensen [May48, May49, HJS49] using a mean-field approach, the shell model, where non-interacting nucleons occupy eigenstates up to the Fermi surface of an Harmonic oscillator plus spin-orbit potential. A noticeable effect of the shell structure is how

full occupancy of the major shells afford extra stability to nuclei having the corresponding number of valences nucleons, referred as *magic numbers* (2,8,20,28,...).

This description of the nuclei became a *de facto* dogma as it successfully predicted the nuclear binding energy and explains spin and parity of states of particle stable nuclei. Since nearly two decades, the development of facilities capable of producing nuclei away from the stability line provided the opportunity to investigate nuclei with a very unbalanced proton-neutron ratio, for which isospin induced noticeable effects on the mean-field description. Strong modifications in the shell structure with appearance of new magic numbers and new regions of deformation induced by large changes of the gaps have been observed. An emblematic case of strong shell structure evolution is the reduction of the N=20 gap in neutron-rich isotopes, giving rise to *e.g* particle instability of the double closed shell $^{28}_{8}O_{20}$ and region of deformed N=20 nuclei. Within the shell model, Otsuka *et al* have proposed an interpretation in terms of evolution of shell-model effective single-particle energies due to the properties of the nucleon-nucleon interactions [OA07, OSF$^+$05, OFU$^+$01].

In light nuclei, a strong evolution of the N=8 and Z=8 shell closures is also observed despite the relative " rigidity "of the magic number 8. Indeed, as stressed in [SP08] the magic number 8 appears in any phenomenological mean-field description using Hamiltonians based on central potentials of various forms (square well, harmonic oscillator, Wood-Saxon,...). However, for Z$\leq$6, a strong reduction of the N=8 shell gap occurs when removing protons from the $0_{p3/2}$ shell. Schematically this behaviour can be explained by the fact that the $\left[\pi_{p_{3/2}} - \nu_{p_{1/2}}\right]$ proton-neutron interaction is strongly attractive so that the neutron shell $0_{p3/2}$ becomes much less bound when the $\pi_{p3/2}$ shell empties, reducing the $\nu 0_{p_{3/2}}$-$\nu 0_{d_{5/2}}$ and $\nu 0_{p_{1/2}}$-$\nu 1_{s_{1/2}}$ gap. This reduction of the N=8 gap has been evidenced experimentally by the abnormally low excitation energies of the 2^+ [NAA$^+$00], 1^- [IMA$^+$00] and 0^+[SSM$^+$03] states measured in the ^{12}Be as well as p and sd neutron configurations mixing [NAA$^+$00, PCO$^+$06]. More recently, the same effect has been observed for Z=8 in the mirror nucleus ^{12}O [SIB$^+$09].

All the above description in terms of single-particle energy evolution is essentially qualitative since it does not take into account correlations that play an important role as we shall see in the following.

1.1.2 Clusters

In the regions of light nuclei, correlations produces specific effects such as strong clusterization. The emergence of compact subsystem of nucleons, clusters, from the mean-field give rise to peculiar spatial configuration [Fre07]. Also some light systems can be described in terms of the covalent exchange of neutrons between α-clusters, resulting in so-called nuclear molecules, an example of which is the ^{9}Be nucleus, which has a $\alpha - n - \alpha$ structure.

While clusterization is manifested essentially in excited states at an energy close to the cluster emission threshold in ^{8}Be, ^{12}C and ^{16}O among other α-conjugate nuclei [ITH68], the situations might well be different near the drip-line. Figure 1.2

show calculations performed in the framework of the Anti-symmetrized Molecular Dynamics (AMD) performed for the Boron isotopes [KH01].

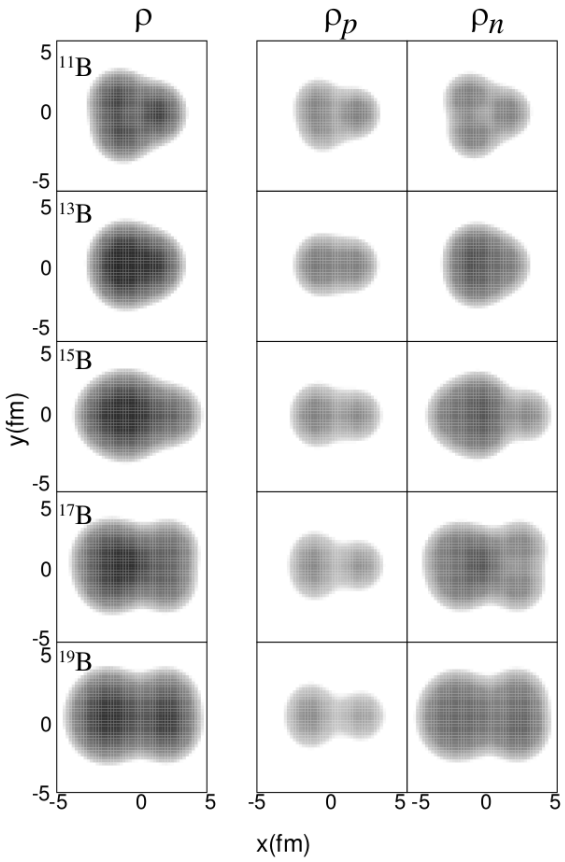

Figure 1.2: *Ground-state matter density distribution in Boron isotopes from [KH01]. The proton ρ_p and neutron ρ_n matter distribution are extracted from the AMD wave functions.*

AMD models are sophisticated tools to investigate the formation of cluster since it does not require the pre-existence of clusters, so that cluster and shell-model type systems are treated in a single framework. In Fig.1.2 we see the evolution from a stable ^{11}B up to the neutron drip line where the ^{19}B appear highly clustered. One can note the large changes in the spatial configuration after addition of two neutrons.

1.1.3 Halos

Approaching the drip-line, the separation energy of valence nucleons decreases gradually. Considerable tunnelling into the classically forbidden region occurs as combination of the short range nuclear force and low separation energy of these nucleons. This tunnelling is traduced by a large spatial extension of one or more nucleons, forming a more or less pronounced halo. Of course all nucleons have a

non-zero probability to be located at distance of the core, and arise the difficulty to define properly a halo nucleus. Björn Jonson proposed to defined halo nuclei as one where the probability for a valence nucleon to be located outside of the potential well is over 50% [BJ04]. From the point of view of quantum physics, the valence nucleons can be described as trapped within the short range potential well formed by the core. In the case of halo nuclei, the valence nucleons binding energy is so low that they have a very extended wave function outside of the core, the evanescent wave function vanishing slowly. This spectacular effect, which gives a ^{11}Li the same root mean square radius as ^{48}Ca, as illustrated in Fig.1.3, requires the angular momentum of the valence nucleons to be small, otherwise the centrifugal barrier would not allow the extension. Similarly, the protons, because of the Coulomb barrier, are kept closer to the core, explaining why a pronounced halo structures is not yet observed in proton rich nuclei. More complicated structures exist, such as the five-body system ^{8}He described as a tightly bound ^{4}He core surrounded by four neutrons forming a *neutron skin*.

The neutron halo has been discovered by Tanihata *et al.* at the Laurence Berkeley National Laboratory [THH^{+}85] during systematic study of interaction cross sections and deduced root mean squared radius R_{rms} along the Helium, Lithium and Beryllium isotopic chains.

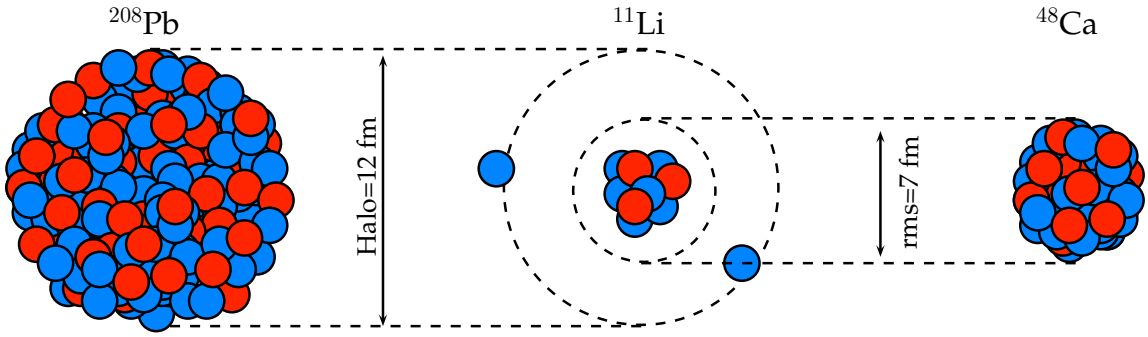

Figure 1.3: *The size of ^{11}Li and its two neutrons halo compared to the size of stable nuclei. Value of the halo radius and rms came from [BJ04].*

Among halo nuclei, ^{11}Li occupies a special place as the first two-neutron halo nucleus discovered. It is described as a so-called borromean nucleus which corresponds to a three-body system ^{9}Li+n+n where none of the binary subsystems are bound. ^{11}Li has been the subject of many experimental and theoretical works. As a neutron closed-shell nucleus N=8 being at the drip-line, ^{11}Li is expected to present strong correlations in its ground state due to the closeness of the *p* and *sd* neutron shells, as discussed above. An early attempt to describe the neutron halo was performed by Sagawa, Takigawa and van Giai using the Random Phase Approximation (RPA) and describing the oscillation of the halo's nucleons around a nearly inert core [STvG92]. This study lead to the prediction of soft dipole resonances in ^{11}Li and ^{10}He around 1 Mev above the two neutron separation energy S_{2n}.

A recent calculation [SJZ09] predicts the ^{11}Li ground state to be dominated by $(\nu_{s_{1/2}})^2$ and $(\nu_{p_{1/2}})^2$ components. A theoretical analysis of data from the ^{11}Li(p,t) reaction [PBVB09] evidences components involving the quadrupole vibration of the ^{9}Li core as well as the dipole vibration associated with the neutron halo. Such new modes called soft dipole states are often considered as dynamical modes associated with excess neutrons in neutron-rich nuclei. In the case of ^{11}Li, strong low-lying E1 excitations have been observed at low energy in a Coulomb dissociation experiment [NVS$^+$06].

The structure of the ^{11}Li nucleus is of importance for the present work since it will constitute our initial state to investigate ^{10}He.

1.1.4 Neutron-rich Helium isotopes

The case of the neutron-rich Helium isotopes represents an illustration of the above mentioned phenomena. ^{4}He is well known for being one of the most bound of all nuclei, with nearly 20MeV separation energy of its nucleon. Therefore the Helium isotopic chain offer the opportunity to understand how neutrons behave in the field of a tightly bound core. Extensive study of the Helium isotopes has been carried shading light on the neutron interaction in nuclear matter. A first feature of the Helium isotopic chain is the so-called *Helium anomaly*, demonstrating how the correlations between valence neutrons play an important role in the binding mechanism of neutron-rich nuclei. Adding more neutrons increase the neutron binding energy by 800 keV when going from ^{6}He ($S_n = 1.7$ MeV) to ^{8}He($S_n = 2.5$ MeV) as can be seen in Fig.1.4.

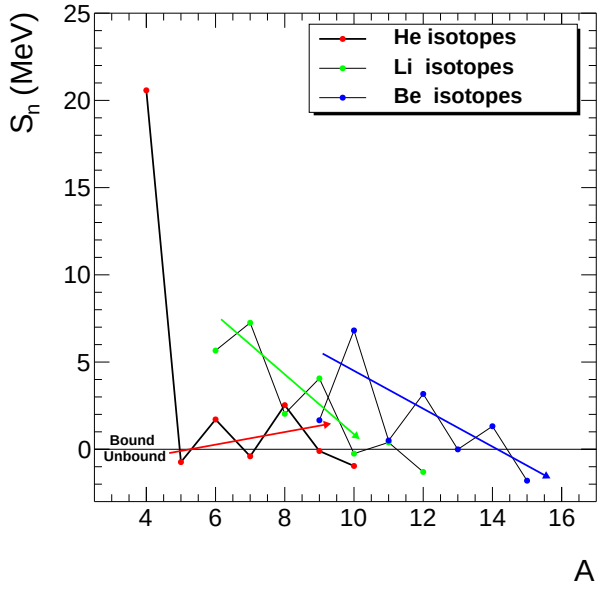

Figure 1.4: *The one neutron separation energy of He, Li and Be isotopes from [AWT03]. The red (He), green (Li) and blue (Be) arrows show off the abnormal trend for He isotopes.*

Another interesting feature is the unbound nature of ^{5}He, ^{7}He, ^{9}He, and ^{10}He, accessible experimentally and allowing a systematic study. The study of ^{5}He has

been carried out in the 80's and lead to the conclusion of a pure $0_{p_{3/2}}$ neutron configuration. The ^{6}He case shows different features. While a pure ^{4}He is expected to be surrounded by two $0_{p_{3/2}}$ neutrons, the calculation reproduce the experimental data only by taking into account a coupling to the $0_{p_{1/2}}$ and *sd*-shell up to 20% of the ground state component. The unbound ^{7}He and its small neutrons spectroscopic factor is an ^{4}He core surrounded by valence neutrons in mixed state in the $p_{3/2}$ and $p_{1/2}$ configuration. The neutron skin of ^{8}He also shows significant mixing of $(p_{3/2})^2(p_{1/2})^2$ configuration in the $(p_{3/2})^4$ one. Mean-field calculations within the Hartree-Foch-Bogoliubov model also indicate sizeable contributions of the $(p_{3/2})^2(s_{1/2})^2$ and $(p_{3/2})^2(d_{1/2})^2$ configurations (see [JAA$^+$10b] and reference therein for more details).

Concerning clustering in the neutron-rich Helium a theoretical study in the AMD framework [AIO06] of the role of the t+t clustering on the binding energy of the Helium isotopes has pointed out the important role of this component. Experimentally, the weight of the t+t configuration in the GS of ^{6}He was found much smaller than theoretical predictions in [GRCD$^+$05] a study of the ^{6}He(p,t) transfer reaction.

Beyond the dripline, the case of ^{9}He remains unresolved experimentally. As explained above, the N=8 shell gap vanishes far from stability, leading to the inversion of the $\frac{1}{2}^-$ and $\frac{1}{2}^+$ states (so-called parity inversion) in the neutrons-rich N=7 isotones ^{11}Be and ^{10}Li. Despite quite a few experimental works, the spectroscopy of resonances in ^{9}He is not firmly established yet. A recent compilation of the last experimental results can be found in [Kal10].

1.2 Theoretical approaches

1.2.1 Three-body models

Light neutron-rich nuclei show off spectacular effects such as halo states and strong clusterization. These effects come from the complex interplay between an important coupling, responsible for cluster formation, and a weak-coupling, responsible for loosely-bound valence nucleon to go far from the classically allowed range of the nuclei. Three-body models have been developed in order to describe and understand the interplay of these two couplings and how they affect the bound mechanisms leading in loosely-bound nuclei, like ^{6}He and ^{11}Li, or resonant system like ^{10}He. For that purpose, an assumption on the clusterization is the beginning of the study, here a strongly bound core plus two valence nucleons weakly interacting.

In the three body model calculations for such nuclei, the knowledge of the resonances of the unbound core+neutron system is a key ingredient. As we pointed out above, this is the case for the barely known ^{9}He, which limits the predictive power of such calculations

In a calculation using the method of analytic continuation in the coupling constant allowing to solve the unbound three-body model of ^{8}He+n+n, Aoyama predicted the level scheme of the ^{10}He resonances [Aoy03, Aoy02], based on the

work by Chen *et al* [CBB+01]. The latter claimed the observation of a s-wave ground state, observed as a virtual state in ^{9}He. Results of the calculation are shown in Fig.1.5. A never observed ground-state located a few keV above the two-neutron threshold with a $\left[s_{1/2}s_{1/2}\right]^{0+}$ configuration and a narrow width of 210 keV. The first exited state is a resonance located at E = 1.68 MeV with a decay width Γ = 1.12 MeV and a main component $\left[p_{1/2}p_{1/2}\right]^{0+}$.

We note that in the framework of this model, ^{11}Li represents a favourable initial state to populate the predicted ground-state because of their similar structure.

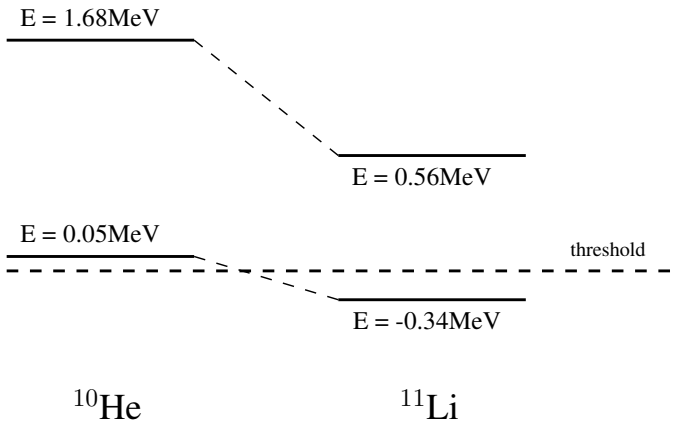

Figure 1.5: *Level predicted by Aoyama in [Aoy03] for ^{10}He and ^{11}Li.*

1.2.2 *Ab initio* approaches

Ab initio calculations constitute an attempt to describe the nuclear structure of all nuclei using consistent n-body bare interactions between nucleons. If the nuclear forces are not completely known, nucleon-nucleon scattering experiments, as well as structure of two- and three-body system, such as di-neutron, ^{2}H and ^{3}H, are sources of informations to obtain realistic two- and three-body interactions.

Solving the many-body problem analytically is possible up to four-body system, but not for more bodies. However, the last decade showed a great improvement in the numerical techniques, such as the Quantum Monte Carlo (QMC), combination of the Variational Monte Carlo (VMC) and Green Function Monte Carlo (GFMC) methods, which managed to calculate nuclei as heavy as ^{12}C. The method also demonstrates the decisive effect of the three-nucleons forces in nuclei structure as shown in Fig.1.6, allowing to evaluate the masses of light nuclei with 1-2% accuracy. Model like the No Core Shell Model (NCSM) [NQSB09] gave result for heavier nuclei such as ^{16}O.

The method tries to find a solution of the Schrödinger equation using the

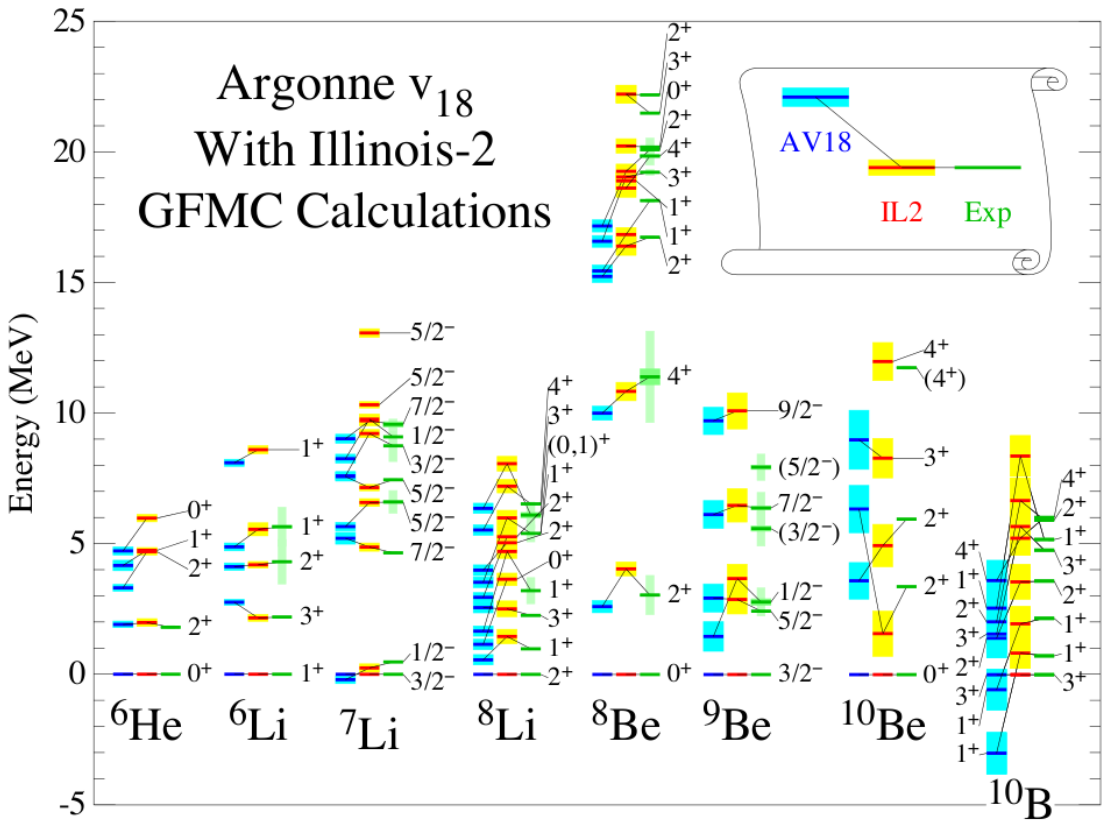

Figure 1.6: *GFMC result from [Pie05] are compared to experimental spectroscopy (green) of light nuclei using two-body av18 interaction only (blue) and using additional Illinois-2 three-body interaction.*

non-relativistic Hamiltonian :

$$H = \sum_i (-\frac{\hbar^2}{2m}\nabla_i^2) + \sum_{i<j} \nu_{ij} + \sum_{i<j<k} V_{ijk} \tag{1.1}$$

The Quantum Chromodynamics (QCD), is the fundamental theory describing the strong interaction, responsible for the nucleon-nucleon interaction. In the case of nuclear physics, the low energy does not allow a perturbation treatment and the nucleon-nucleon interaction can not be deduced directly from this theory. *Ab initio* approaches rely on Yukawa-like model [Yuk35] where the nucleon-nucleon interaction is described in terms of meson exchanges.

Unfortunately no *ab initio* calculations are available now for the studied nuclei ^{10}He nucleus of interest. However, great progress in this kind of large-scale calculations gives hope that predictions might be soon available. In the following, we shall see that other predictions from these models that the states energies, namely

overlap functions, constitute extremely relevant quantities to interpret the results from our experimental approach based on direct reactions.

1.3 The ^{10}He spectroscopy

During many years experimentalists tried to find evidence of a bound ^{10}He. The doubly-magic shell structure, systematics on the Helium isotopic chain as well as model predictions let think of a bound nuclei, would it be the highest neutron-proton ratio observed. Experiments on the spontaneous fission of ^{252}Cf as early as 1967 [WT67][CCG67], were unable to give these evidences. During the same period, spallation of Uranium using high energy protons beam showed again no indication of a measurable bound ^{10}He. Nearly twenty years later an ^{18}O fragmentation experiment at 30 MeV/A, lead to a general agreement on the particle unstable nature of the ^{10}He nucleus.

Studying an unbound nuclei is particularly challenging. Many experimental ways are naturally closed, keeping the structure observables, such as radius or matter density, away from us. Therefore, many experiments and approaches are required until a general agreement on the understanding of the nuclei structure will be obtained.

There are two ways to study an unbound nuclei, either product through fragmentation into ^{8}He+n+n+X, where X is the rest of the projectile, and measured the momentum of the three particles ^{8}He,n,n reconstructing the invariant-mass spectrum of ^{10}He. This method limits to only one decay channel since the detection in coincidence of ^{6}He+n+n+n+n is limited by the efficiency of neutron detectors. The second technique consist in populating ^{10}He through a two body reaction where ^{10}He is the recoiling system, all the information about ^{10}He is therefore carried way by the quasi-target particle. This method has no limitations in term of decay channels, but is strongly limited in statistics both due to low cross section and the necessity of thin targets. The two methods have been used to study ^{10}He, and gives complementary, sometimes contradictory, results on its spectroscopy.

The following section will detail the different experiments performed previously to study the ^{10}He resonances. A summary of the observed resonant state is presented in Table 1.1 at the end of the section.

1.3.1 ^{11}Li +CD2 $\rightarrow$ ^{10}He+X

The first experimental evidence of the ^{10}He system forming a resonant state was obtained from the study of the ^{11}Li +CD2 $\rightarrow$ ^{10}He+X reactions at 61 AMeV performed at RIKEN, on the RIPS line [KYA^{+}94]. The experiment [KYA^{+}94] was carried out using the *invariant mass method* in the ^{8}He+n+n channel. Through this technique, the decay fragments of the resonant ^{10}He are detected and the invariant mass formula allow the reconstruction of its initial energy. The resonances appears in the spectra as a narrow increase of cross section at specific energies.

The ^{11}Li +CD2 system can produce ^{10}He through different processes, such as the ^{11}Li(d,^{3}He) proton transfer reaction, or the ^{11}Li break-up on deuterons and carbon nuclei of the target. In the later case, the ^{10}He resonances are manifested as final state interaction of the ^{8}He+n+n system. The two reaction mechanisms could not be separated in this experiment because of the thick target used, forbidding the detection of the recoil ^{3}He produced in the transfer reaction.

A dipole magnet was setup after the reaction target to detect the fragment with bending a drift chamber followed by a scintillator hodoscope. Neutrons were detected in coincidence by means of a wall of scintillator placed in the beam direction a few meters downstream the target.

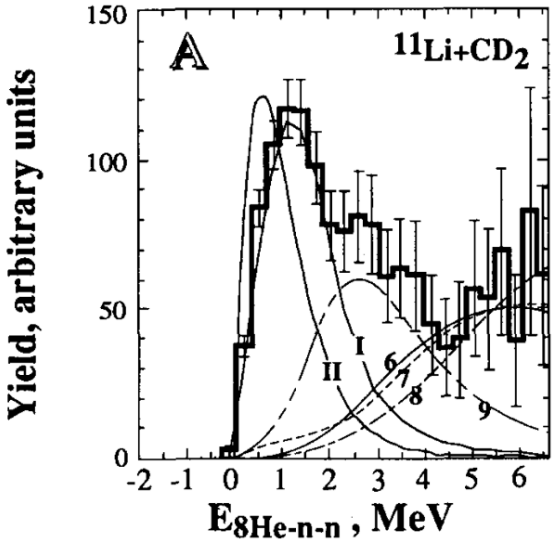

Figure 1.7: *Result of the ^{11}Li break-up experiment. The spectra is obtained as the excess energy of the ^{8}He+n+n system detected in coincidence. Line I show the resonance position, while line II show the expected background if no resonance is present. The other line represent various physical background as explained in [KYA^{+}94].*

The invariant mass spectrum of ^{8}He+n+n is presented in Fig.1.7. A strong peak located at $E_{^{8}He+n+n}$=1.2 (3) MeV above threshold is observed and attribute to the resonance of ^{10}He. An upper limit of the width is deduced as $\Gamma \leq 1.2$ MeV.

1.3.2 Double charge exchange reaction

Shortly after the ^{11}Li +CD2 were published, Ostrowski *et al* presented their result of a study using the double charge exchange reaction ^{10}Be(^{14}C,^{14}O) at E_{Lab} = 334.4 MeV using a radioactive ^{10}BeO target [OBG^{+}94]. In this missing mass measurement, the ^{14}O residues are detected with the help of a magnetic spectrograph

At the incident energy the reaction corresponds essentially to a four-nucleons transfer (a two-protons pick-up and a two-neutrons stripping). If the very low cross section of such a process is compensate by the use of a stable beam, this approach suffers of the presence of several contaminants in the reaction target.

Fig.1.8 show the obtained spectrum after subtraction of the contributions from other target constituents. A first peak located at 1.07 (7) MeV above the ^{8}He+n+n threshold is observed in agreement with the result of [KYA^{+}94]. A relatively narrow width of Γ = 0.3 (2) MeV is reported. Two other resonances are found at E = 4.31

(20) MeV and E = 7.87 (7) MeV. Tentative spin assignments were made from the comparison of the measured width to R-matrix calculation.

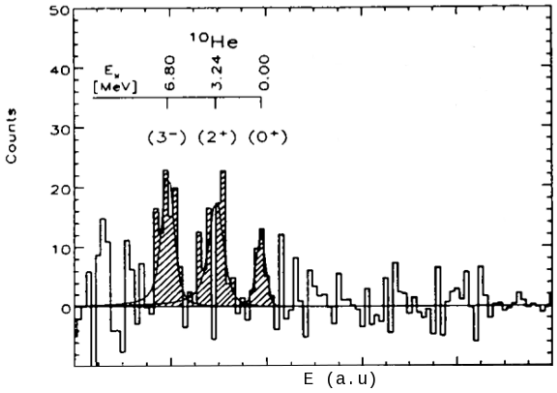

Figure 1.8: *Excitation spectra of ^{10}He from double charge exchange reaction [OBG$^+$94] obtain after subtraction of all the physical background. The first resonant state, located 1.07 MeV above the ^{8}He+n+n threshold, is taken as reference for the other states.*

1.3.3 (p,2p) reactions

An early attempt to study ^{10}He using a (p,2p) process on a ^{11}Li beam was conducted by Kobayashi *et al* in 1997 at RIKEN [KYO$^+$97]. The separation energy spectrum of protons in ^{11}Li deduced from the measurement of the 4-momenta of two protons from the (p,2p) process is shown in Fig.1.9 (right panels). When gating the single spectrum by the detection of a forward ^{8}He fragment in coincidence, a broad peak appears at an energy corresponding to E = 1.7 (3) MeV above the ^{8}He+n+n threshold, close to the result of [KYA$^+$94]. Nevertheless, the quasi free conditions for the knock-out of a 20 MeV-bound proton at the low energy of 83 AMeV is questionable.

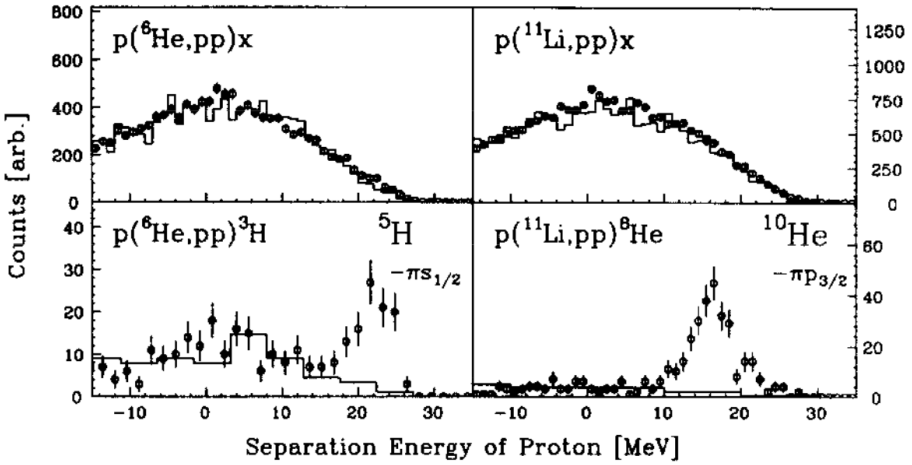

Figure 1.9: *Proton seration energy spectra leading to resonant structure of ^{10}He from (p,2p) experiment (top and bottom right quadrant) and other light nuclei from [KYO$^+$97] . The solid histograms are Carbon background.*

More accomplished results for the same reactions have been published very recently [JAA+10b, JAA+10a]. The experiment was performed at GSI using a relativistic ^{11}Li beam at 280 AMeV impinging a CD2 liquid hydrogen target. The ALADIN magnet was used to bed the charged residues and the LAND setup fro the detections of neutrons.

Figure 1.10 and Fig.1.11 present the results of this invariant mass measurement. Within experimental uncertainties, the shape of the obtained relative energy spectrum of the ^{8}He+n+n system from the ^{1}H(^{11}Li ,^{8}He+n+n) is identical to the one of [KYA+94]. Initially, two decompositions of the spectrum were proposed, providing fits to the data of equivalent quality:

- Sum of Breit-Wigner shaped resonance located at 1.42 (10) MeV above the ^{8}He+n+n threshold (with a width Γ = 1.04 (16) MeV) and a so-called correlated background determined by the structure of the ^{11}Li ground-state (see Fig.1.10).

- Sum of two resonances at 1.54 (11) MeV (Γ = 1.91 (41) MeV) and 3.99 (26) MeV (Γ = 1.64 (59) MeV) above the ^{8}He+n+n threshold (see Fig.1.11).

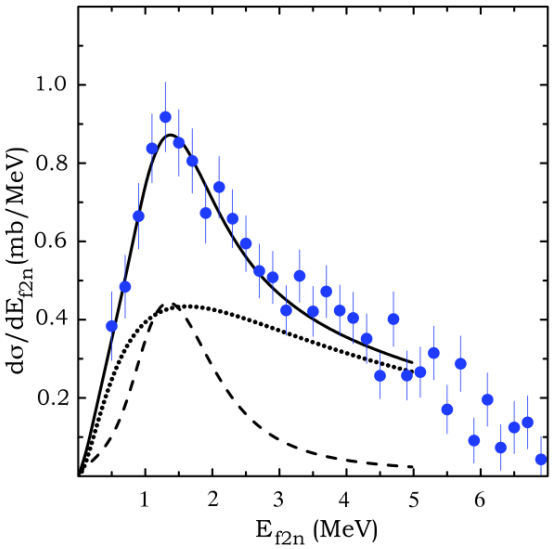

Figure 1.10: *Excitation spectra of ^{10}He ,from [JAA+10b] ,interpreted as a narrow resonance at 1.42 MeV (dashed line) and a correlated background (dotted line).*

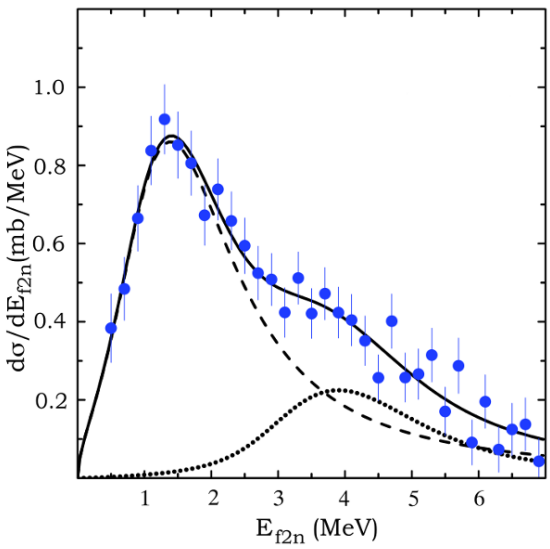

Figure 1.11: *Excitation spectra of ^{10}He ,from [JAA+10b] ,interpreted as a two resonances around 1.54 MeV (dashed line) and 3.99 MeV (doted line).*

In a forthcoming paper [JAA+10a], Johanson *et al* have shown by exploiting the experimental energy and angular correlations between the decay products ^{8}He+n+n that the data can be interpreted with the second decompositions only. Proposed spin-parity is $I^{\pi} = 0^{+}$ for the first resonance and $I^{\pi} = 2^{+}$ for the second one.

1.3.4 ^{8}He(t,p) transfer reaction

The only attempt to study ^{10}He by mean of transfer reactions was held on the ACCULINNA separator where ^{8}He(t,p) reaction at 27.4 AMeV was investigated in inverse kinematic using a cryogenic gaseous tritium target. The recoil protons were detected by a silicon annular telescope placed in the backward hemisphere, and the heavy residues by a silicon telescope integrating strip detectors. The ^{6}He(t,p) reaction was used as reference.

The low statistics accumulated during the experiment makes difficult the interpretation of the obtained missing-mass spectrum of ^{10}He shown in fig1.13. The noticeable absence of count below 3 MeV rises questions about the selectivity of the (t,p) mechanism to populate the ^{10}He first resonance. A theoretical interpretation [GZ08] has proposed the 3 MeV peak observed in the presently discussed work as corresponding to the 1.2 MeV state of [KYA^{+}94] "if one takes into account the peculiar reaction mechanism for the ^{11}Li beam used in [KYA^{+}94] ".

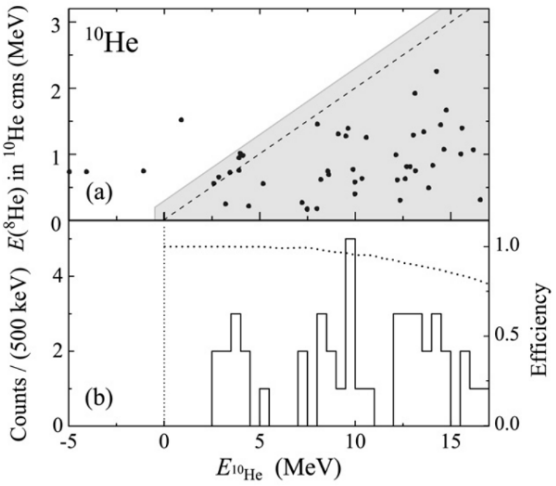

Figure 1.12: *Result from (t,p) reaction presented in [GGTA^{+}09]. The (a) panel show off the correlation between the ^{8}He laboratory energy and the ^{10}He excitation energy. The shaded area represent the kinematically allowed area. The (b) panel show the associate ^{10}He excitation spectra, with no count below 3MeV.*

A second experiment has been performed recently using the same setup [Sid11]. A preliminary spectrum exhibits sizable number of counts in the 0-3 MeV region of the missing mass spectrum.

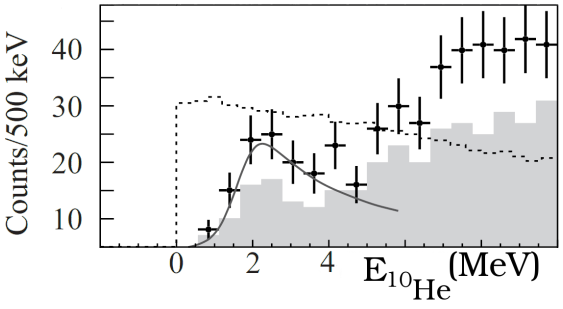

Figure 1.13: *Result from (t,p) reaction presented in[Sid11]. The ^{10}He new excitation spectra is interpreted by a resonant state located at 2.1 MeV above the two neutrons emission threshold.*

	^{11}Li+C			^{11}Li+CD_2	^{10}Be(^{14}C,^{14}O)	^{11}Li(p,2p)
	^{11}Li(p,2p)	^{11}Li(p,2p)	^{8}He(t,p)	^{11}Li+CD_2	^{10}Be(^{14}C,^{14}O)	^{11}Li(p,2p)
	[JAA$^+$10a]	[JAA$^+$10a]	[GGTA$^+$09]	[KYA$^+$94]	[vBG$^+$95]	[KYO$^+$97]
E_r	1.42(10) MeV	1.54(11) MeV	No state	1.2(0.3) MeV	1.07(7) MeV	1.7(3)(3) MeV
Γ	1.11(76) MeV	1.91(41) MeV	—	$\leq$ 1.2 MeV	0.3(2) MeV	—
E_r	—	3.99(26) MeV	$\geq$ 3 MeV	—	4.3(2) MeV	—
Γ	—	1.64(89) MeV	—	—	1.0(3) MeV	—
E_r	—	—	—	—	7.87(6) MeV	—
Γ	—	—	—	—	0.6(3) MeV	—

Table 1.1: *Summary of observed states in* ^{10}*He.*

1.4 Proposed approach

We proposed to investigate the ^{10}He resonances throughout the proton transfer reaction ^{11}Li(d,^{3}He) at 50 AMeV, taking advantage of the relatively high intensity of the ^{11}Li beam at intermediate energies available at the RIPS line at RIKEN, as compared for instance to the LISE line at GANIL. Using the same setup we have also studied the same reaction induced by a ^{9}Li beam at 50 AMeV in view of providing complementary results as well as a reference reaction in order to check the calibration and detectors positioning. As we will see in the following, this later point is crucial when spectroscopy of the nucleus of interest is not well-established.

As compared to previous invariant mass studies in proton knock-out experiments using ^{11}Li, one can expect a spectrum with different physical background and not dependent on the decay channel. Above all, the (d,^{3}He) transfer reaction gives access to important spectroscopic informations, namely the nuclear overlaps $\langle {}^{A}X|^{A-1}Y\rangle$.

The cross section for a one-step transfer reaction a+A $\rightarrow$ b+B is usually calculated using the Distorted Wave Born approximation (DWBA). As we will see in the following, the nuclear overlap $\langle B|A\rangle$ is an important ingredient of the DWBA transition amplitude since it carries most of the nuclear structure information[1]. In that sense, overlap functions provide the interface between nuclear structure and direct reaction theories.

Spectroscopic factors are defined as the norm of the radial part of the nuclear overlap $\langle A|B\rangle$:

$$S_{lj} = \int_0^\infty r^2 I_{lj}^2(r) dr \tag{1.2}$$

Spectroscopic factors factorizes in the DWBA cross section so that they can be extracted from the transfer data through a normalization procedure:

$$S_{AB} = \frac{d\sigma_{exp}}{d\Omega}(\theta_{CM}) \left(\frac{d\sigma_{DWBA}}{d\Omega}(\theta_{CM}) \right)^{-1} \tag{1.3}$$

In standard DWBA calculations the radial overlap function is often approximated by:

$$I_{ij}(r) \approx S_{ij} \cdot \frac{u_{nlj}(r)}{r} \tag{1.4}$$

Where $u_{nlj}(r)$ is obtained by solving the Schrödinger equation with a Wood-Saxon potential whose depth is adjusted to reproduce the binding energy of the transferred particle. Recently, overlap functions deduced from *ab initio* calculations of nuclear wave-functions of light nuclei become available [BPW11]. In the latter reference overlap functions from state of the art GFMC wave functions are calculated for A $\leq$ 7. Similar calculations for nuclei up to A=10 are expected in the near future.

[1]For a reaction where a and b correspond to light particles such as p,d,t,^{3}He

From a general point of view, the comparison of DWBA cross section calculation using *ab initio* overlap functions with experimental data of transfer reactions with light nuclei represents a priori a stringent test for these models. In a recent study of knock-out reactions from p-shell nuclei, the neutron spectroscopic factors for $\langle {}^{10}Be|{}^{9}Be\rangle$ and $\langle {}^{10}C|{}^{9}C\rangle$ overlaps have been compared to values calculated in Variational Monter Carlo (VMC) with inclusion of three body forces and N Core Shell Model (NCSM) [GBG$^+$11]. VMC overlaps have been used in the analysis of recently performed transfer reaction studies on ^{7}Li and ^{8}Li [WSR$^+$08] that will be discussed in the following. These results illustrate the relevance of experimental studied of reaction giving access to nuclear overlap functions to discriminate between *ab initio* models. The present work aims to provide differential cross sections from proton pick-up reaction (d,^{3}He) on ^{9}Li and the halo nuclei ^{11}Li from which the above nuclear structure information can be deduced.

Chapter 2

Experimental Set-up

The RRC66 experiment was held in July 2010 at the RIKEN Nishina Center accelerator facility , in the framework of a campaign of experiments using the MUST2 detector at RIKEN. The chief goal was the production and study of the ^{10}He resonances through the ^{11}Li(d,^{3}He) transfer reaction.

The RIKEN facility is a unique place to produce high intensity ^{11}Li beam at low and intermediate energy. The ^{11}Li beam used in this experiment was produced by fragmentation in the RIPS (RIKEN Projectile-fragment Separator) line at the RIKEN Nishina Center and sent on a CD2 target at 50 AMeV. In addition a ^{9}Li beam was produced in the same way, to provide a reference reaction as well as complementary data. The low quality of the fragmentation beams requires the use of beam tracking detectors in order to track the beam position on target as well as its incident angle. For this task, a set of four Parallel Plate Avalanche Counter (PPAC) developed at RIKEN was used (see Sect.2.2).

Fig.2.1 presents the setup installed around the reaction target. It was designed to study three different kinds of reactions in parallel, using all presently available (eight) MUST2 telescopes. Four telescopes were placed at forward angles in wall-type configuration to study pick-up reactions, complemented by four thin silicon detectors. Two more telescopes were placed at backward angles to investigate (d,p) reactions. One telescope around ninety degrees allowed the study of elastic and inelastic scattering. Plastic detectors and one MUST2 telescope were added around zero degrees for the detection of heavy products of reactions. A detailed description of the setup will be given in Sec.2.5.

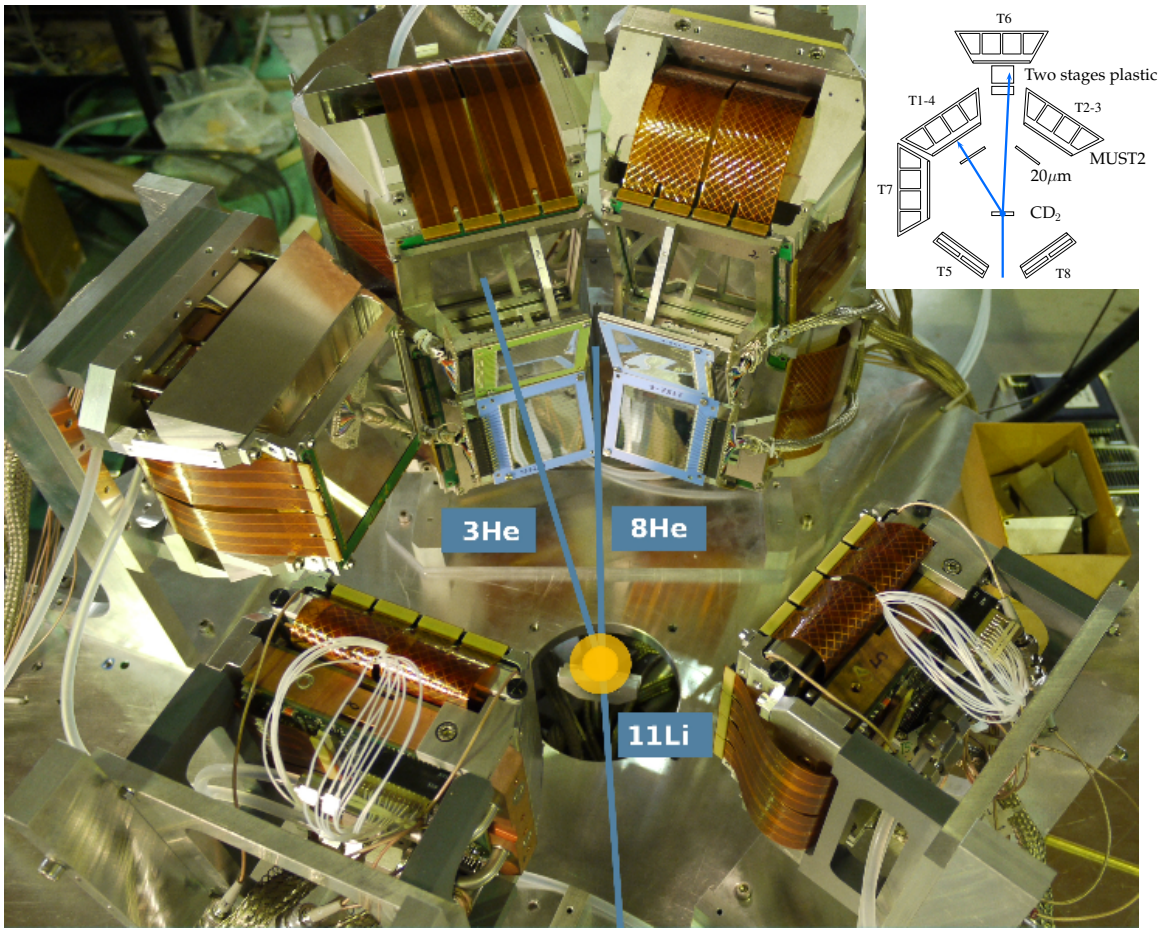

Figure 2.1: *A picture of the setup around the reaction target in E6 experimental hall. The upper right corner show a top view scheme of the complete setup.*

2.1 Beam production

The RIKEN Accelerator Research Facility Facility (RARF, see Fig.2.2) delivers secondary beams of unstable isotopes of intermediate energy at the RIPS line using the fragmentation method. In our case a ^{18}O beam was fragmented at 100 AMeV on a ^{9}Be production target mounted on a water-cooled holder. The ^{18}O was extracted from an ECR ion source and then accelerated in the AVF cyclotron, transported to the RIKEN Ring Cyclotron (RRC) where it was accelerated up to 100 AMeV. The fragmentation produced a cocktail beam of many stable and unstable nuclei, the purification of the beam was performed by the RIPS fragment separator.

A schematic layout of the RIPS is presented in Fig.2.3. The line can be split into three independent segments [KII^{+}92]. The first QQQ-SX-D-SX-Q segment, placed at zero degrees after the production target, provides a dispersive focal plane F1 and analyses the magnetic rigidity of the fragments. This focal plane offers a separation of the fragment following their A/Z ratio. The second QQ-SX-D-SX-QQQ segment, compensates the first section's dispersion and provides a doubly

achromatic focus at the F2 focal plane. A wedge-shaped degrader placed at F1 allows the separation of ions according to their $A^{2.5}/Z^{1.5}$ ratio.

The last QQQ section, provides a third achromatic focus at the F3 focal plane where the detection will lay. This last section gives a better flexibility on the beam focusing, independently of the former first two segments that select the beam particles, and provide a time of flight measurement using plastic scintillator at F2 and F3 to determine the beam energy on a ∼7 m long path.

The RIPS line offers a large maximum rigidity, up to 5.76 T.m. At F1 and F2 a set of adjustable slits allows to perform a selection of the nuclei. When the slits are fully opened, the maximum angular acceptance of 80 mrad and a 6% momentum acceptance are reached.

The parameters used for the beams production in the present experiment are summarized in Table 2.1.

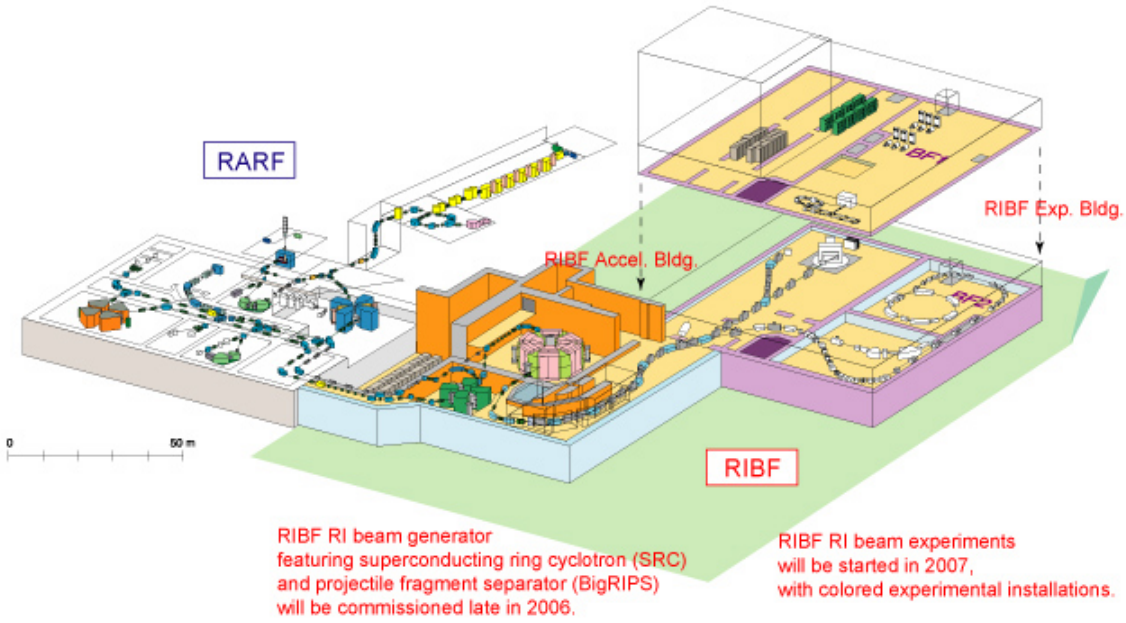

Figure 2.2: *An overview of the RIKEN Nishina Center facility. On the right, the newly constructed RIBF, and on the left, the RARF facility where the experiment was conducted.*

Beam	^{11}Li	^{9}Li
Wedge Number	6	
Wedge Material	Aluminium	
Wedge thickness (mg/cm^2)	816	
Wedge angle (mrad)	4.46	
Bρ_1 (Tm)	4.14153	3.4008
Bρ_2 (Tm)	3.905	3.1829
Total Rate F3	$1.74.10^4$	$1.0.10^5$
main contaminant	^{15}B	^{3}H

Table 2.1: *Production parameters for the two beams used during this experiment.*

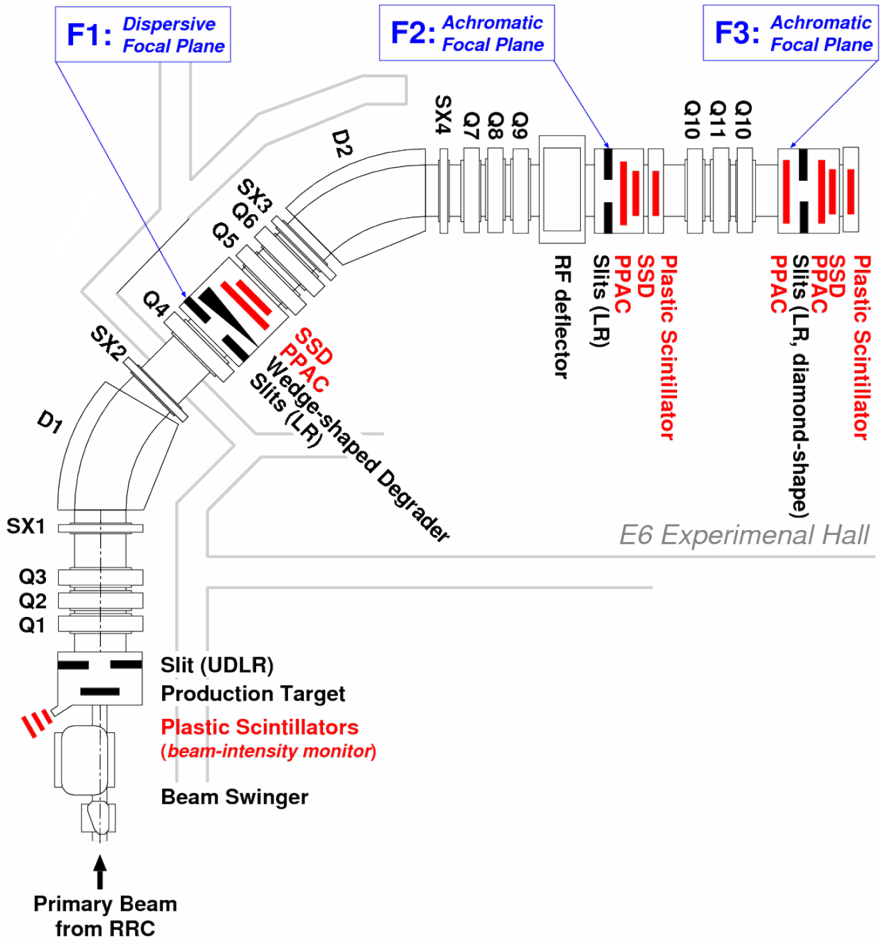

Figure 2.3: *Schematic view of the RIPS Line. The beam coming at the bottom left hit the primary target. The experimental setup is placed at the right side, after the F3 PPAC chamber.*

2.2 Beam tracking Device

The Parallel Plate Avalanche Counter (PPAC) is a Beam Tracking Device (BTD) that collects the charge produced by ions from the beam when crossing a volume of gas [KOF$^+$01]. The PPAC device used at RIPS is schematically shown in Fig.2.4. The charges are collected by two layers of aluminized stripped Mylar, one for X and one for Y direction placed in front and at the back of an anode plate. The PPAC specificity over other BTD is the fact that it relies on a time-based measurement instead of a charge-based one. All the strips are bound together through delay lines and only one signal, sum of all the delayed contributions, is available at each end. A good adjustment between the signal rise time, electrode spacing and delay line is mandatory to achieve a continuous reading of the position. The early version of the detector only allowed a discrete reading. Each PPAC needs only five electronic channels, two for X or Y and one fast anode signal used for timing measurement. The PPAC simplicity is a sake for data analysis. However this device offers a limited efficiency for very light particles at high energy, for example, during the experiment, only 56% , for ^{9}Li and 71% , for ^{11}Li, at 50 A/MeV, of events were reconstructed on target despite the use of four detectors.

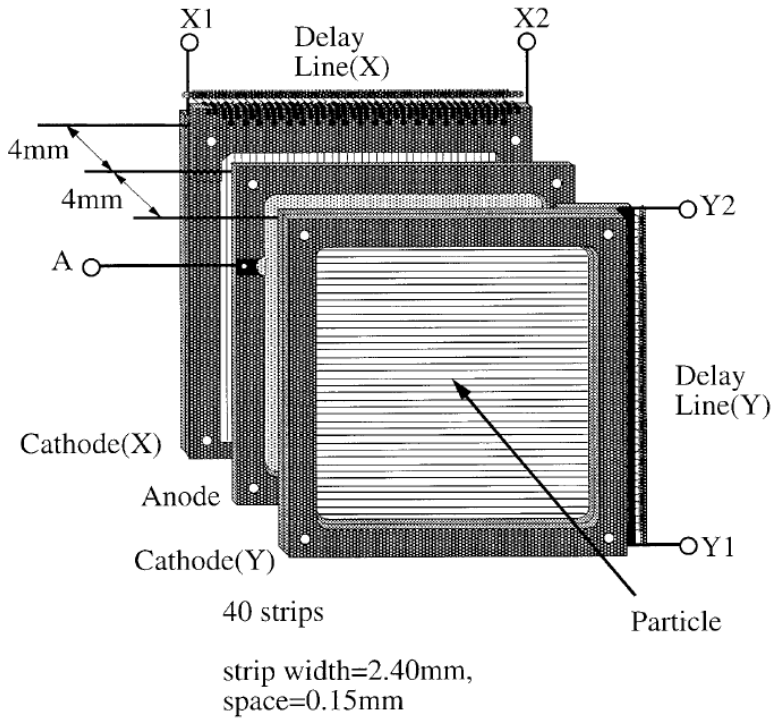

Figure 2.4: *PPAC detection layout as illustrated in [KOF$^+$01].*

2.3 Reaction targets

The Lithium beam was impinging a deuterated polypropylene (CD_2) target. We chose a thickness of 1.5mg/cm^2, as a good compromise between resolution and statistics. A more detailed study about the target choice can be found in the next chapter on simulations performed during the preparatory phase of the experiment. The main issue about these targets is that one third of their matter is made of ^{12}C, producing an important background from *e.g.* break-up reactions on Carbon. The latter's structure favored the α-particles production during such reactions that need to be separated from the ^{3}He coming from the (d,^{3}He) reaction of interest. The background contributions of the reactions on Carbon was evaluated using a pure Carbon target of 1.0mg/cm^2.

2.4 Reaction chamber

In order to host the MUST2 telescopes which were developed with different standards of mechanics and connectics than those available on site at RIKEN, an hybrid solution has been implemented. It consisted in the coupling of different parts of the M2C chamber, commonly used in MUST2 experiments, and of a chamber available at RIKEN. The base plate of M2C has been shipped with the MUST2 detectors and electronics, offering four DN-160 (European standard) flanges for the detectors signals and cooling. The top of the RIKEN chamber, offered three VG-250 (Japanese standard) ports for the vacuum system and probes, as well as a central port for cryogenic target. The cylinder was mechanically coupled to the bottom flange using additional mechanical clamps to properly compress the O-ring seal. All the signal were output from the chamber through the bottom plate equipped with the standard MUST2 electronics and cooling flanges, allowing easy opening of the chamber during the preparation phase. A new support for the chamber was designed and built, allowing pre-alignment of the mechanical ensemble.

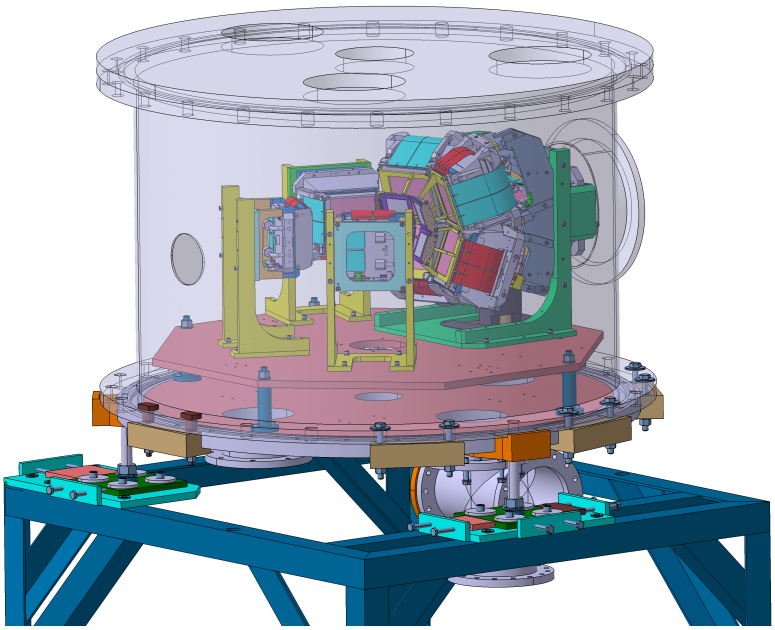

Figure 2.5: *CAD view of the reaction chamber and the detection layout. The RIKEN top of the chamber is here represented in transparent gray allowing to see the M2C chamber plate and detection base plate where all the detectors stand. The adjusting tool, allowing to move the chamber in any direction is also visible at the interface between chamber and frame.*

2.5 The detection

This work focuses on the (d,^{3}He) reaction as well as on the elastic and inelastic scattering. The detection setup was optimized for the specific kinematics of the reactions studied. The simulation study which lead to the present setup is detailed in the next chapter (see chap.3).

Most of the ^{3}He of interest are produced at low energies, from around 7 MeV and up to 30 MeV, inside the production target as shown in Fig.2.6 which presents the reaction kinematics from the ^{11}Li(d,^{3}He)^{10}He reactions 1 MeV above the ^{8}He+n+n threshold. These low energy ^{3}He particles will undergo energy loss, straggling and multiple scattering in the reaction target. They need to be separated from the α-particles background expected to be large.

As detailed in the next chapter, the yield of the particles according to a L=1 transfer cross section show off the region of interest, in the 7-15 MeV region, corresponding to 10-40° in the laboratory. All the particles are kinematically confined in the 0-47° degrees region. A close-up view of the region interest is visible in Fig.2.6.

In this experiment, we used 5 telescopes at forward angles, with DSSD and CsI stages only. T1-4 insured detection of ^{3}He particles between 10° and 50° at

17cm from the CD2 target, whereas T7 was placed around 80° in order to detect the deuterons from elastic and inelastic scattering. A 6th telescope, T6, was placed at 0° for detection and identification of the heavy residues of reaction. A set of two plastic detectors was installed at zero degrees to prevent most of the beam particles from hitting T6.

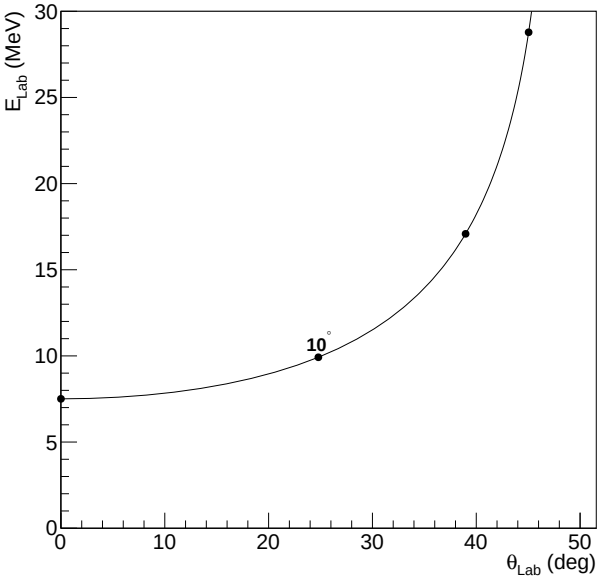

Figure 2.6: *Kinematical line of the reaction at 50 AMeV in the region of interest. Dots on the line indicate an increment of* 10° *center of mass.*

2.5.1 The MUST2 detector

The MUST2 array is made of several (up to eight) telescopes and designed for the study of direct reactions of exotic nuclei on light targets using inverse kinematics [PBRC+05]. Each telescope is made of three detection stages listed below and represented in Fig.2.8:

300μm Silicon The first layer is a Double Sided Stripped Detector (DSSD) of 300 μm thickness and 100x100 mm^2 area. Each side of the detector features 128 strips, with a 0.76 mm strip pitch. The nominal metallization of the strips is 0.4 μm of Aluminum, separated from each other by an inter-strip of SiO_2. A schematic view of the DSSD structure is presented on Fig.2.7. The typical strip resolution in energy is around 40 keV and time resolution 500 ps. At this distance of 17cm the angular resolution is about 0.1°.

Si(Li) The second stage is a Lithium-doped Silicon (Si(Li)) of 4.5mm thickness, composed of two detectors themselves divided in 8 pads each. These detectors offer a resolution of 130 keV, allowing a good energy measurement of particle crossing the first stage and an E-ΔE identification using both first and second stages. Their geometrical coverage correspond to about 65% of the surface

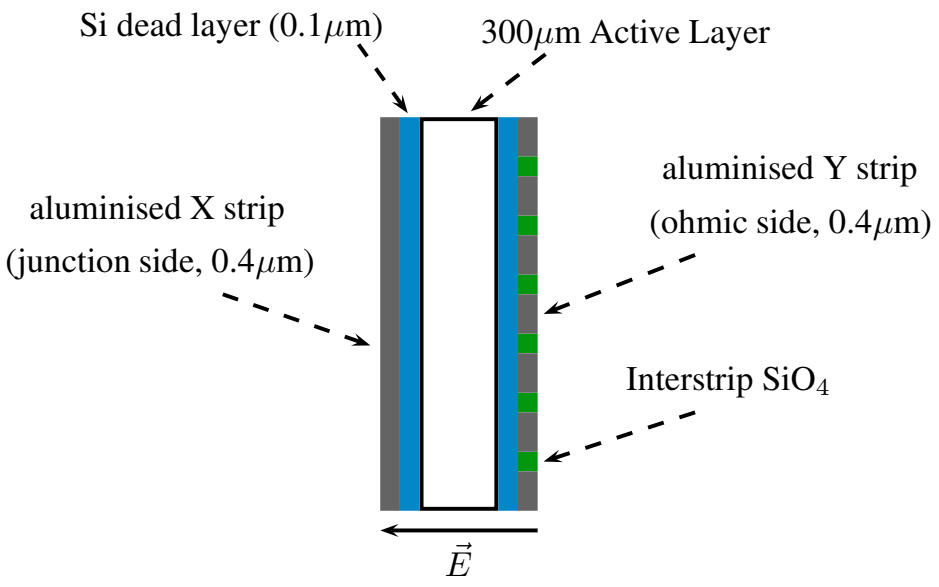

Figure 2.7: *A schematic view of the layout of the DSSD p-n junction detector and its different dead layers.*

of the DSSD. Because the DSSD provides a sufficient resolution and energy range in our case, we did not use the Si(Li) stage for telescopes placed at forward angles. We used them for the telescopes placed are the backward angles, dedicated to (d,p) study.

CsI The third stage of detection is made of 16 CsI crystal scintillator modules, read by 16 photo-diodes. Each crystal is 40 mm thick, able 115 MeV proton. Their energy resolution is rather low with respect to Si(Li) detectors, and moreover, the signal amplitude depends on the type of particles, making the detectors harder to calibrate. The typical CsI resolution depends on the energy deposit and is given by the formula $\sigma_{\text{CsI Energy}} = 0.08\sqrt{\text{CsI Energy}}$ (MeV).

The above-mentioned three stages are held together by an Aluminum frame which presents a complex shape. At the rear of each telescope a massive copper block, coupled to a cooling circuit, cools down the two MUST2 Front End Electronic (MUFEE) boards. The MUFEE card host nine Application-specific Integrated Circuit (ASIC), designed to provide all the necessary analog electronics from pre-amplification to amplification, as well as a time measurement using an external stop. Eight ASIC are dedicated to the strip signals of one side of the DSSD and one ASIC is used for either the CsI or Si(Li) stage. The ASIC has been designed specifically for the MUST2 detection system. It provides energy and time measurement for the three different types of detectors. The multiplexing capabilities of the MUFEE boards, allow a strong reduction of the analog and logic lines.

The analog and logic signals are sent via serial cables to the MUst in VxI (MUVI) digital mother board, installed in a VXI crate outside the chamber. The

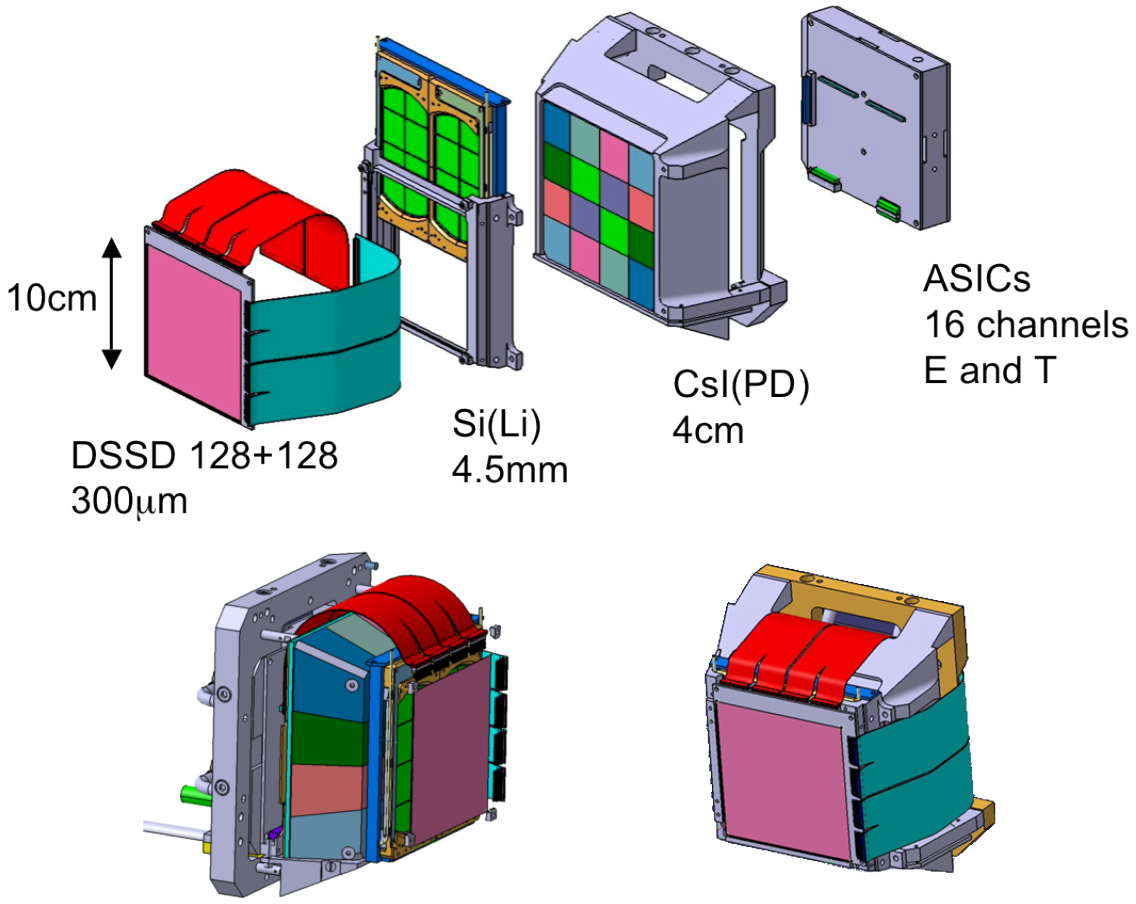

Figure 2.8: *Top: Scattered view of the different stage of a MUST2 telescope. Bottom left: the three stage assembled without frame. Bottom right: a complete telescope.*

MUVI board can digitalize the signals from 4 telescopes and perform low level filtering such as pedestal subtraction. 4 DNL cables are needed per telescope (High Voltage, Low Voltage, Digital Signals Out, Analogue Signals Out) for the 576 channels of one telescope.

All the electronics is parametrized through the standard DAS interface of the GANIL acquisition system. A scheme of the logic electronic associate to the MUST2 detection can be found in App.C.

2.5.2 20μm Silicon detector

Figure 2.6 shows that most of the ^{3}He projectiles of interest are stopped in the first stage of MUST2. Therefore, with MUST2 alone they can be identified only by time of flight (TOF). The later identification separates only in mass, so ^{3}H and ^{3}He are mixed together, whereas the higher energy ^{3}He will mix with the ^{4}He particles. In order to perform an E-ΔE identification of low energy particles (^{3}He below 22MeV) we added a 20μm thick Silicon stripped detector in front of

each T1-4 MUST2 telescope. These detectors were Single Sided Striped Detector (SSSD), presenting 16 strips on the front side. Each detector has a 50 mm by 50 mm active area, surrounded by a 9mm wide frame. Energy resolution was around 100 keV. Those detectors were mounted on an aluminum frame screwed on the MUST2 frame. Because the detector offer half the detection surface of the MUST2 DSSD, they were deported by 65mm toward the target as shown in Fig.2.9. Therefore, almost all the surface of the MUST2 DSSD could be used in conjunction with the SSSD.

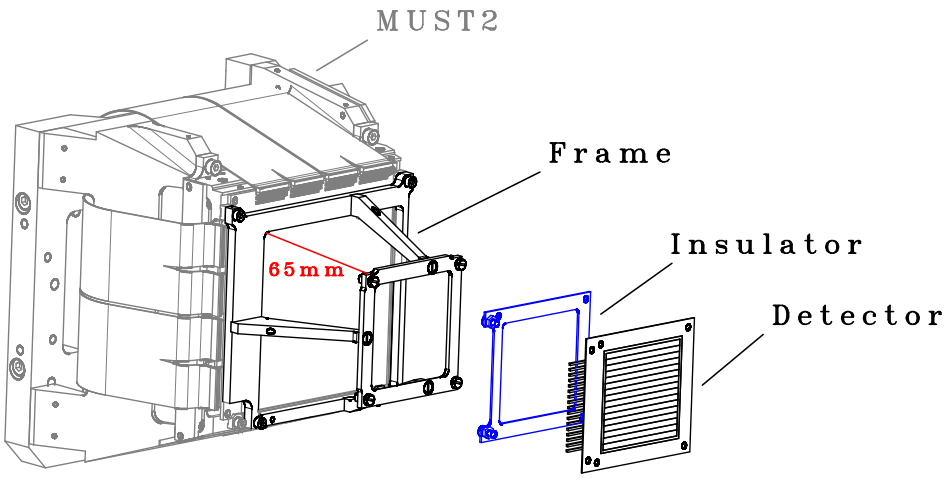

Figure 2.9: *A silicon Single Sided Strip Detector (SSSD) shown in front of the dedicated mechanical design for assembly with a MUST2 Telescope. The aluminium frame was held in front of the DSSD using screws directly on the telescope frame.*

2.5.3 Plastic detectors

To prevent damages to the 0° MUST2 telescope (T6) we used a two stages plastic telescope placed upstream the T6 telescope. The two stages were made of BC450 scintillator, coupled with two Hamamatsu photo-multipliers (PM) through light guides. The detectors were wrapped in aluminised Mylar and opaque material to avoid light leaks and cross-talk. An additional 2mm layer of lead was used at

the back to prevent the numerous low-energy beta decay electrons to trigger the MUST2 zero degrees telescope. The design of the mechanics holding the two plastic detectors was slightly complicated by the high density of detectors around zero degrees as illustrated in Fig.2.10. The detector thickness was 20 mm for the first stage and 30 mm for the second stage and covered an active surface of 70 mm by 40 mm in front of the zero degrees telescope.

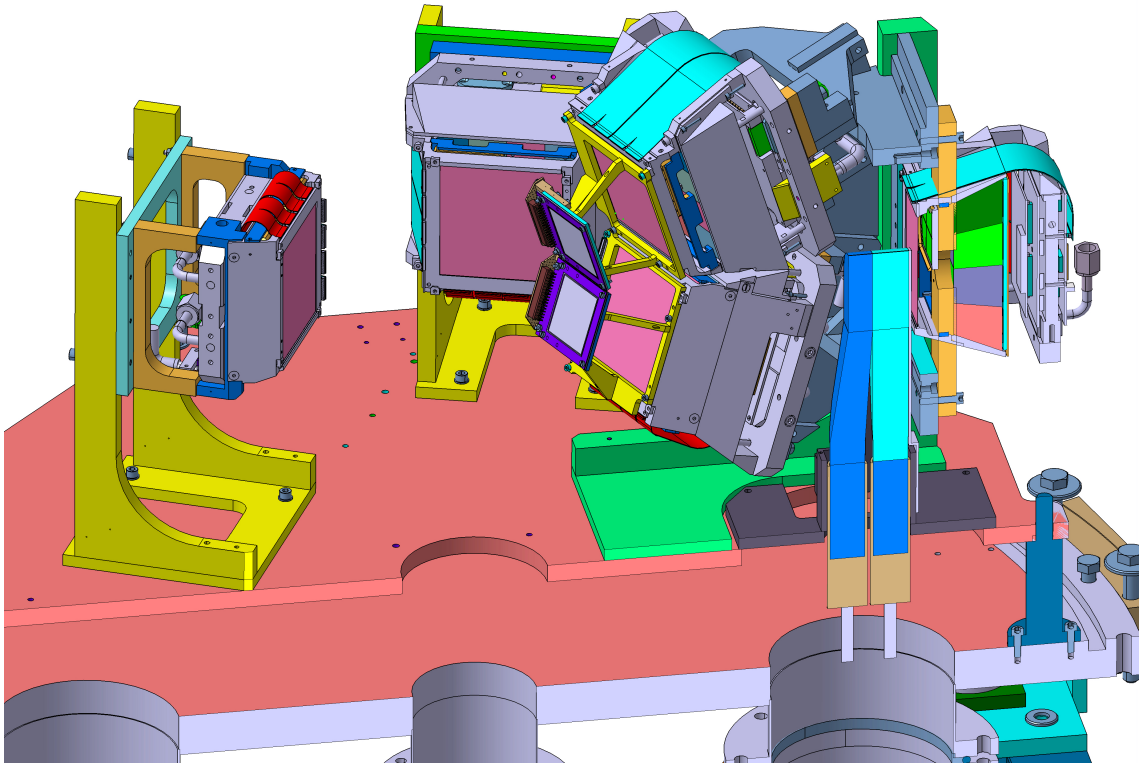

Figure 2.10: *The left half of the detection setup is seen in this CAD view, allowing to see the zero degrees plastic (light and dark blue) and telescope on the right. Each plastic is read by a PM (brown) connected through a light guide (same color as the scintillator).*

2.6 Electronics and data acquisition

The MUST2 array relies on the GANIL data acquisition (GANIL DAQ) system for the control of its electronics and data acquisition. Therefore it was decided for this experiment to couple the GANIL DAQ and the RIKEN DAQ systems. The GANIL DAQ was handling the MUST2 block of data and trigger, while the RIKEN DAQ had in charge data from the SSSD, beam line and plastic detectors. The GANIL Master Trigger (GMT) module, was collecting the trigger signals from all the detectors (MUST2, PPAC, plastic,..), and generating a common trigger signal

for both GANIL and RIKEN acquisitions. When this signal was received by the RIKEN acquisition, a read-out of all detectors parameters was performed. During the read out process, the RIKEN acquisition was sending a busy signal to the inhibit input of the GMT, preventing the GANIL acquisition to run while the RIKEN one was busy. This way, the two acquisitions could run along and collect data separately but synchronously with common dead time.

The merging of data flow coming from both acquisitions was performed with the help of the NARVAL system, which allows data flux management. It was setup in a way where the GANIL data (MUST2 and GMT data) were send to the RIKEN DAQ at each event, and merged with the other detectors data within the RIKEN data file.

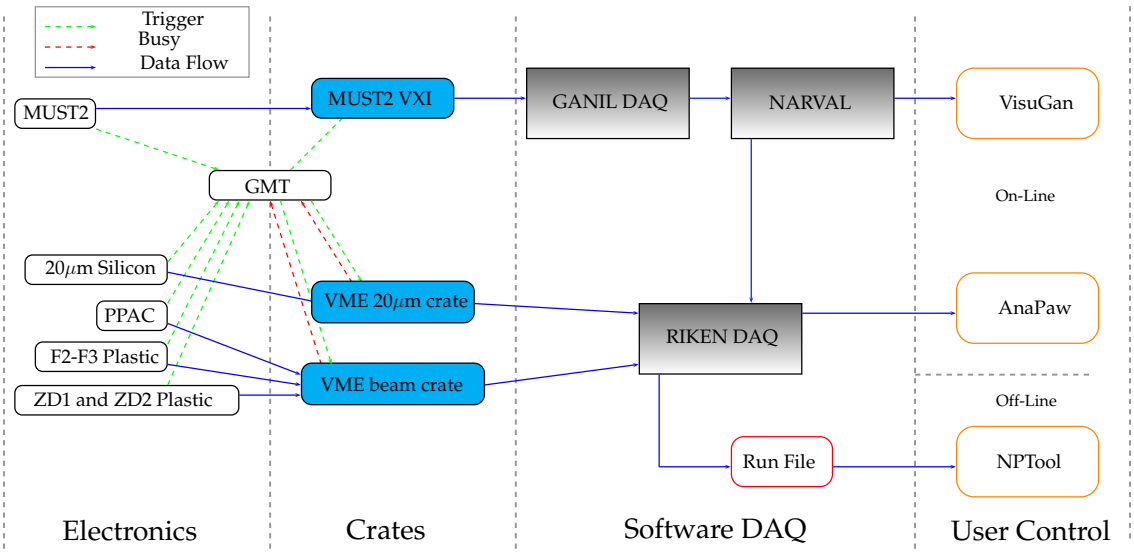

Figure 2.11: *Overview of the coupled acquisition and common trigger system. The user control allow the visualization of spectra during the experiment, VisuGan is the standard on-line user control software for GANIL experiment and AnaPaw its RIKEN counter part. NPTool was used as an offline analysis programs.*

The coupled-acquisition running scheme is presented in Fig.2.11, showing how the trigger signals are managed by the GMT that lead the two acquisitions to run along. The electronics layout of the experiment is shown in App.C.

2.7 Detectors position measurement

To reach the angular resolutions that can be obtained by combining the PPAC and MUST2 position information, an accurate knowledge of the detectors position is required. A private company, PASCO, was asked to perform the measurement using a laser-based technique. A laser tracker, in this case a LTD800 from Leica Geosystem, follows the position of a cube corner mirror and stores its relative position at any time. Using this device and selecting some reference points in the room,

the surveyor was able to define a referential in the laboratory. Point on the last three quadrupoles were used in conjunction with reference mark on the ground and wall as exposed in Fig.2.12.

Once the referential was defined, the detectors positions were measured. Because the cube corner was too big to fit the printed circuit board (PCB) hole of MUST2 DSSD, a special tool was produced at RIKEN. Three points were measured on each PCB with an accuracy of 0.5μm. The PPAC positions were also measured as well as the target position.

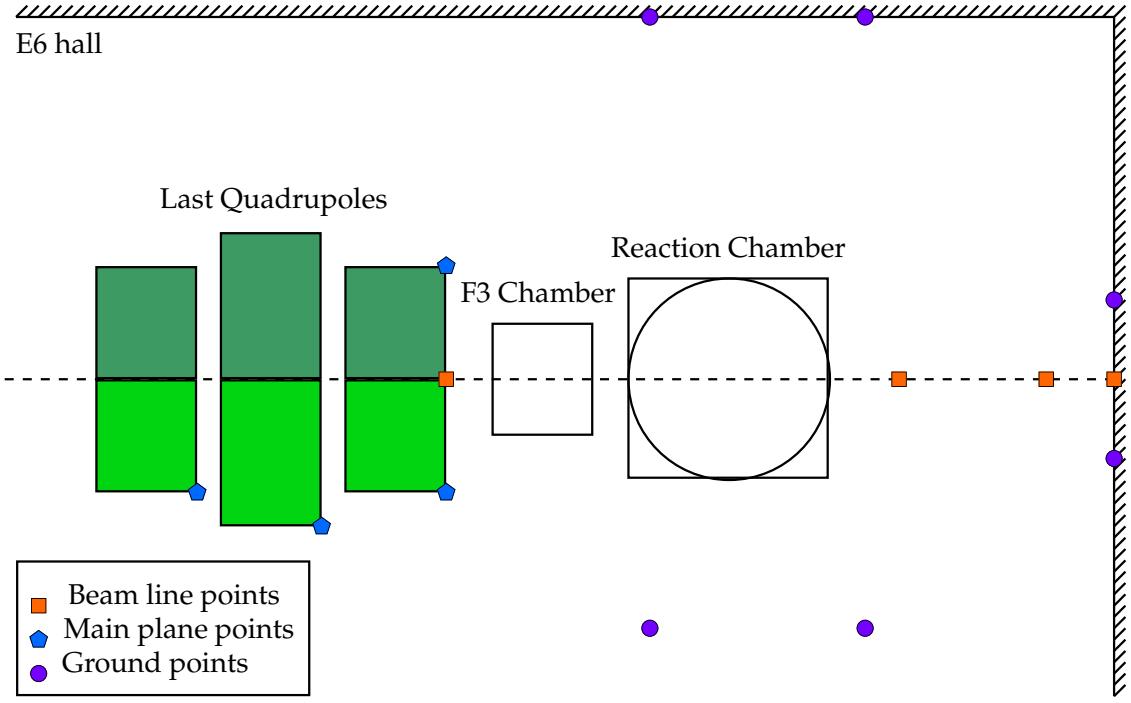

Figure 2.12: *The different points used to build a referential using the laser tracker.*

The use of a low tolerance pinning system designed at IPN Orsay for the MUST2 mechanics, visible on Fig.2.13, allows a precise positioning of the detectors. Set of holes has been drilled in the plate supporting the whole detection inside the chamber. Every assembled pieces has at least two pins to reach a high level of reproducibility when mounting the detection setup. The pins themselves has only 20 μm allowance, however the whole assembled pieces have around 200μm reproducibility. Deformation of the base plate because of the uneven mass repartition, deformation of the chamber plate and mounting allowance of the DSSD themselves, conduct to up to 2mm discrepancies between the PASCO measurement and the CAD provided value.

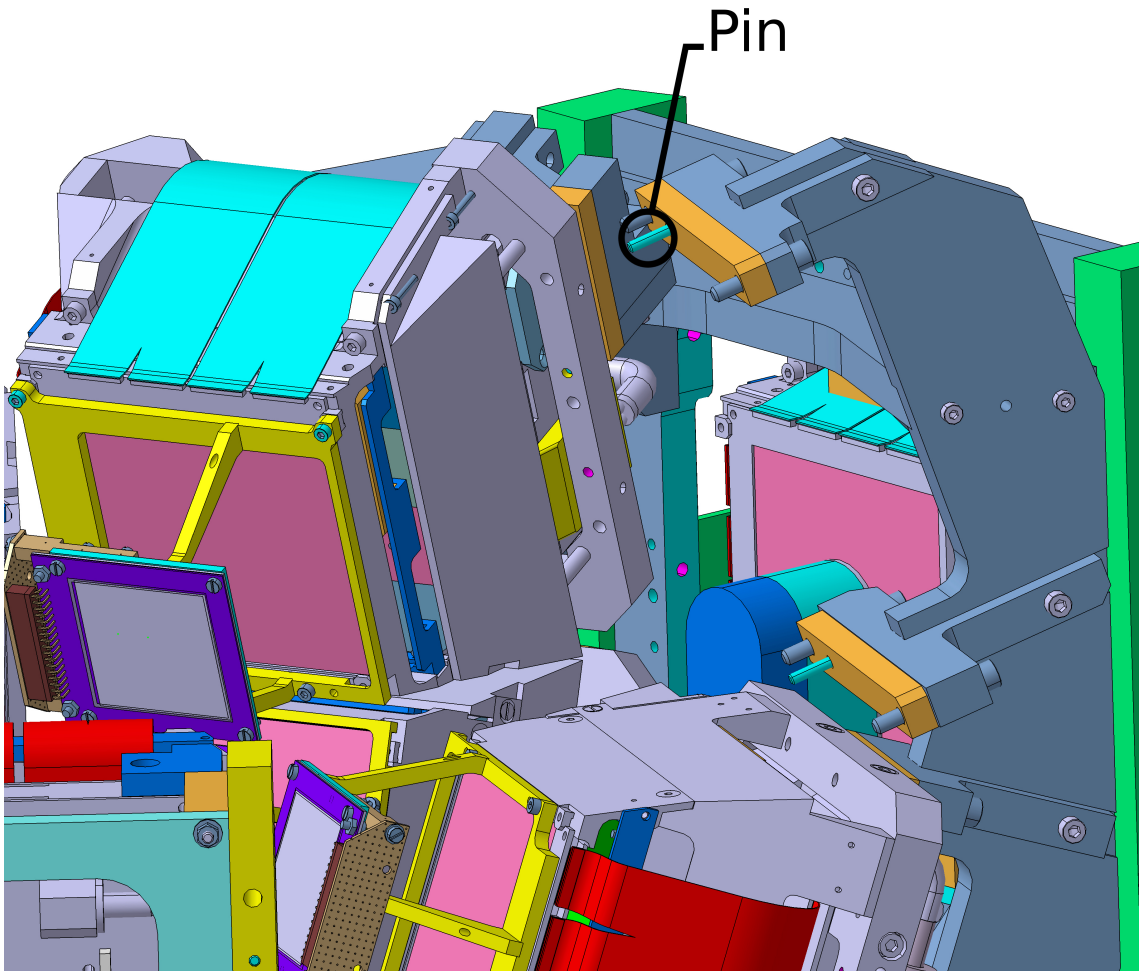

Figure 2.13: *One of the MUST2 telescope is removed from this CAD view to reveal the pinning system used to obtain a low tolerance mechanics. The zero degrees plastic and telescope are shown as well in the background.*

Chapter 3

Simulations

The *Monte Carlo* method to evaluate integral, invented in 1949 by Nicholas Metropolis [MU49], gave birth in the following years to a brand new approach for the resolution of problem involving a large number of parameters. The simulation of an experimental setup is one of such problem, where the statistical behavior of the initial conditions is known and interfere with all the parameters that define the setup. In 1974, a first version of GEometry And Tracking (GEANT) was released within the CERNLIB. Since the code evolved and the state of the art *Monte Carlo* simulations for particles interaction is the GEANT4 package.

In this thesis, two kinds of simulations have been performed. Firstly the *prior-experiment* simulations, aimed at defining the feasibility and performances of the experimental setup. This part of the study is about optimization, we will try to emphasize how the simulations lead to the actual setup and how the simulations played a decisive role in the experimental decisions. The second one are the *post-experiment* simulations, used to understand the experimental observations and to obtain the *real* performances of the experimental setup.

3.1 Previous and present simulation tool

Monte Carlo simulations have been handled in the past by simple programs, taking into account the geometry in a very crude form. A couple of programs of that kind exist in the different laboratories working on MUST2 and allow to obtain indications on the setup performances. However, the geometry of the detection is rather complicated, while experiment tend to add more and more ancillary detectors. A complete GEANT4 simulations was needed for the MUST2-TIARA-EXOGAM-VAMOS experiment in GANIL. A GEANT4 based simulation of the MUST2 array, as well as the other γ and particles detectors was used for the first time [Ram09] and was useful for *post-experiment* studies of a MUST2 experiment. However the very rigid form of the code does not allow any flexibility on the detector positions or number.

Because the setup needed to be defined completely from scratch, a new tool has

been designed, that fulfills the needs of flexibility and effectiveness of an exploratory *prior-experiment* work. The project, named NPTool (Nuclear Physics Tool), was designed to be as universal as possible for the common work of simulation and analysis of nuclear physics experiments. An overview of the structure of this project is given in App.A, while the simulation results obtained from this package are presented in the present chapter.

3.2 Prior-experiment simulations

The starting point is the will to study the ^{11}Li(d,^{3}He)^{10}He reaction at 50 AMeV by missing mass method, namely detection the remaining ^{3}He to reconstruct the ^{10}He excitation energy spectra. However inclusive spectra, requiring only the detection of a light ^{3}He, are hard to interpret because of the contamination of other processes, like break-up. Hence, we need also to detect the heavy particles of the reaction around zero degrees. The unbound nature of the ^{10}He also plays a decisive role here, as it decays into 8He+n+n or 6He+n+n+n+n. Other direct reactions can occur during the experiment, providing additional data, and we also designed a setup allowing the detection of light particle related to the (d,d) and (d,p) reactions. The detectors choice and their positioning are, as it will be explained in the following sections, dependent of the reactions studied. We will focus on the design of the (d,^{3}He) related detection for clarity.

3.2.1 Building the setup

Optimizing the setup means taking into account all the aspect of the experiment to obtain the best compromise on resolution and statistics. We rely on three important criteria to choose the best experimental setup:

- **Energy resolution**: which is given by the width of the peaks in of the obtain excitation spectra.
- **Efficiency**: which is given by the percentage of the emitted particles detected.
- **Particles identification**: Which characterizes how the particles of interest can be distinguished from the background.

To start with the simulation the energy of the beam as well as the cross section of the transfer reaction have to be determined.

Beam Energy

The energy of the beam is a decisive parameter in the experiment. It governs both the statistics, favoring a transfer reaction at low energy and break-up at high energy, and the kinematics with all the implication on the resolution and detection efficiency. Taking into account all those parameters, as well as availability of beam at the RIKEN Nishina Center, we choose as a good compromise an energy of 50 AMeV. This energy was used for all the prior-experiment simulations.

Cross section

The differential reaction cross section has been calculated (see Fig.3.1) using DWBA, for a state at 1 MeV above the two neutrons emission threshold, assuming a L=1 transfer of a p shell proton of ^{11}Li. For the purpose of the setup definition, the relevant information is given by the yield of the ^{3}He in the center of mass (see Fig.3.2) and given by:

$$N(\theta_{CM}) \propto \frac{d\sigma}{d\Omega_{CM}} \cdot 2\pi \sin(\theta_{CM}) \tag{3.1}$$

The $\sin(\theta_{CM})$ term coming from the solid angle formulation has strong effect. Hence, the counting rate is expected to be null around zero degrees CM because of the small solid angle. The noticeable facts are the concentration of the yield in the 5°-60° region because the solid angle is favoring the second maximum at larger angle.

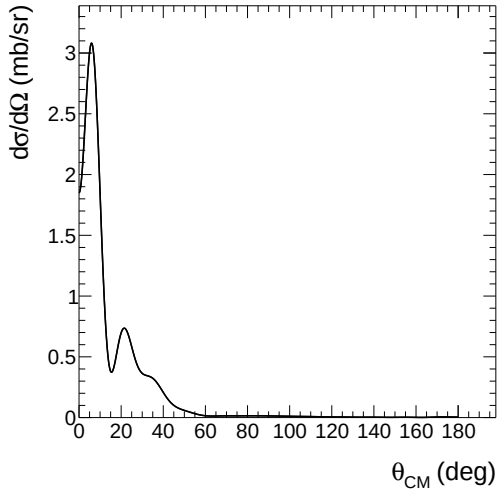

Figure 3.1: *The reaction differential cross section in the center of mass.*

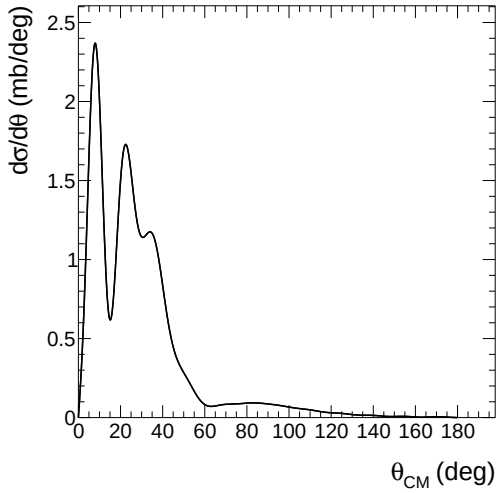

Figure 3.2: *Yield of the ^{3}He in the center of mass.*

DWBA calculations are known to be correct at small angles in the center mass, while at higher angle, other non-direct processes like formation of a compound nucleus, are influencing the cross section shape and intensity. Therefore, for extraction of the relevant information on the structure of ^{10}He, we focus on the small angles in the center of mass frame. The region 5°-20° is therefore considered more important than the one from 20° to 40°.

Kinematics

By applying momentum and energy conservation rules, we can associate the energy and angle in the laboratory with the unique angle in the center of mass of

the outgoing particle. The position along the curves described by the (E_{Lab},θ_{Lab}) is called the kinematic line, the one associated to the ^{3}He, is represented in Fig.3.3.

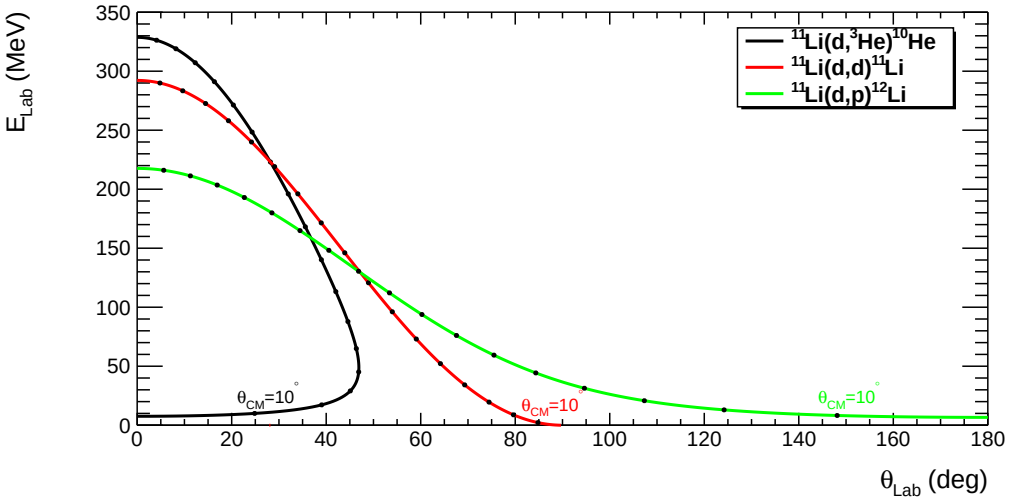

Figure 3.3: *Kinematic line of the ^{3}He from the reaction of interest (black line) in the laboratory, extracted from a relativistic calculation. The black dots are placed every 10 degrees in the center of mass frame. Note the low energy at small CM angle, where the cross section is higher. Other reactions ((d,d) in red and (d,p) in green) are also plotted, showing the regions of interest of these reactions.)*

We can see in Fig.3.3 a folding point around 47°, characteristic of this kind of reaction in inverse kinematics. The black dots on the figure are placed every 10° in the center of mass. The high energy branch is associated with large center of mass angle, where the yield is lower (see Fig.3.2), while the low energy branch, is associate to an important yield.

Conclusions

All this information come as an input of an event generator that takes into account the specificity of the reaction at this energy. The Fig.3.4 allow to pin point the relevant region in the laboratory frame. The setup has to fulfill the following requirements for the ^{3}He detection:

1 It should focus in the region between 5° and 20°.

2 It should deal with ^{3}He with an energy ranging from 6 to 40 MeV.

Most of the statistics is below 22 MeV, meaning the ^{3}He stop in the first stage of MUST2. To get an accurate identification of these particles, additional thin silicon detectors were used in front of the MUST2 DSSD, to act as Δ-E detectors. This is the basis of the setup design, while other aspects, such as the target thickness and zero degrees detection need to be defined with accurate simulations.

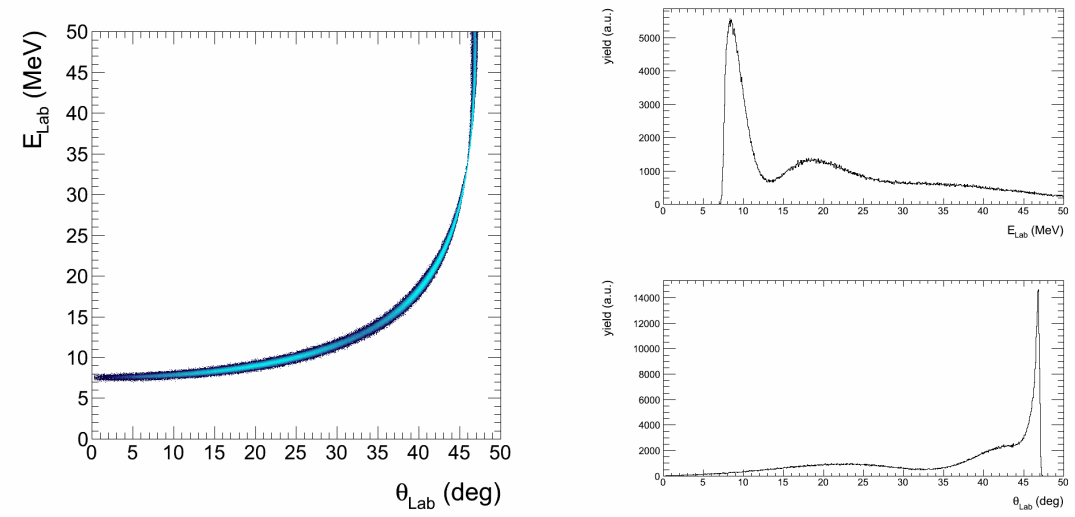

Figure 3.4: *Kinematic line (left) obtain after a Monte Carlo simulation of the reaction (no detection effect are here taken into account). The area of interest with great yield at small angle is clearly visible. The width of the line is here due to the beam energy spread. The angular distribution (bottom right) and energy distribution (top right) are visible.*

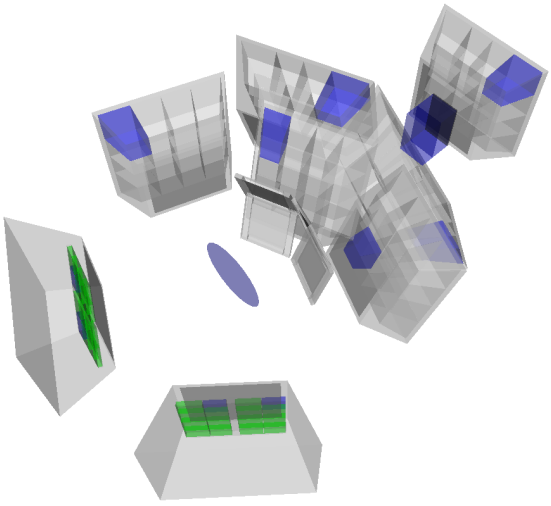

Figure 3.5: *A three dimensional view of the different volume designed within the simulation. Some of the volume are passive material while others act like detection device.*

In addition, to detect ^{2}H from elastic scattering an additional detector was placed around ninety degrees (see kinematics line for (d,d) reaction in Fig.3.3), while another one was setup at backward angle for stripping reaction(see green line in Fig.3.3). Similar study lead to definitive positioning of these detectors. The final setup is presented in fig3.5 as it is modeled in the simulation.

The GEANT4 part of the simulation does not take into account the PPAC, however the initial X and Y positions of the generated event in the target are stored in the output file. During the analysis of the simulations, these values are used to perform a Gaussian random shoot using a sigma of 1 mm, simulating the precision

of the reconstruction on target.

3.2.2 Angular coverage

The setup was designed to detect the maximum of ^{3}He coming from the reaction. Indeed, the detection efficiency in Fig.3.6 is maximum in the region of interest. To achieve this goal we put the MUST2 wall T1-4 17 cm from the target, instead of the standard 15cm.

The obtention of exclusive spectra being mandatory, the efficiency need to take care of the coincidence with the heavy residues of reaction. The coincidence around zero degrees of ^{8}He from the ^{10}He decay reduce by 20% the efficiency at its maximum as presented in Fig.3.7.

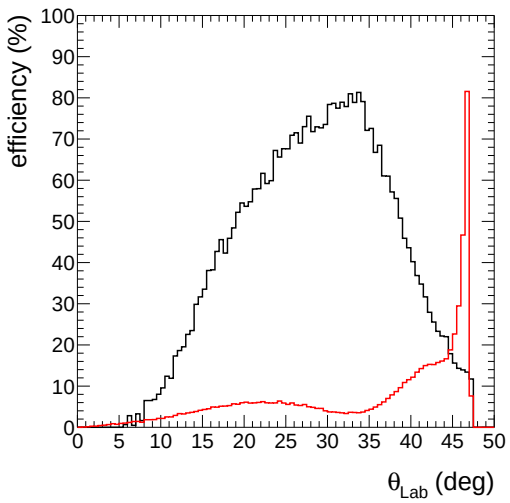

Figure 3.6: *Efficiency of the detection setup in the laboratory frame (black line) for T1-4 and the yield of ^{3}He produced in the (d,^{3}He) reaction (red line, arbitrary unit).*

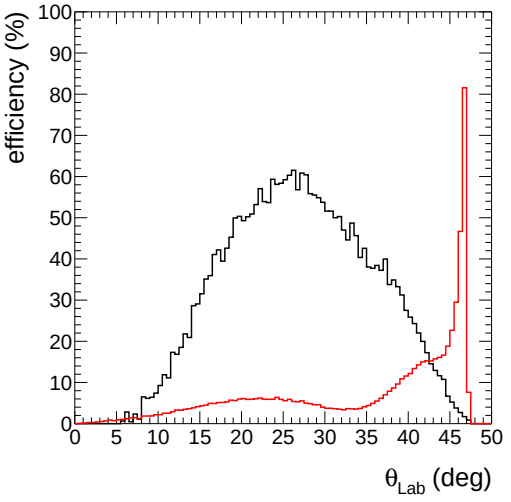

Figure 3.7: *Efficiency of the detection setup in the laboratory frame (black line) for T1-4 after coincidence with the decayed ^{8}He and the yield of ^{3}He produced in the (d,^{3}He) reaction (red line, arbitrary unit).*

The peak visible around 47° in the particle angular distribution in Fig.3.6 and Fig.3.7 correspond to the turning back of the kinematic line. In this region, a large area of the center of mass coverage, the 30°-50° region, is concentrated in a small portion of the laboratory angle, between 38° and 47°. This region is of limited interest for the DWBA analysis of the reaction. Moreover, this part of the distribution correspond also to very large angle ^{8}He, making the coincidence difficult. Hence even if the region represents same yield as in the 5°-38° region, it is not the region to be covered.

3.2.3 Study around the target

A deuterium target is needed for our experiment, several methods exist to produce such target. The conventional way is to produce a thin film of deuterated polyethylene (CD_2), but other more sophisticated methods exist, like cryogenic target, which hold a volume of gaseous, liquid or solid deuterium at low temperature increasing its density. The later targets offer larger number of deuterium atoms by unit of surface but they required important machinery to run.

The possibility to use a cryogenic gaseous target for this experiment has been investigated and was a central part in the simulations work, comparing the situation with CD_2 counter part. A cryogenic target cell can be simulated as a very simple object, two thin windows of light but strong material, keeping a volume of underpressure D2 gas at low temperature. In order to obtain a gain in statistics with respect to CD_2 target, this volume has to be kept around 25-30 K and 0.5-1 bar. Under such pressure, the windows will change shape and the volume of the target will increase, leading to a bigger error on the position of interaction inside the target, and therefore a poorer angular resolution.

The main problem is to find a good compromise between the running pressure and temperature (*i.e.* statistics), angular resolution, and energy loss in the windows. Those parameters are all influencing each other. For instance if you put higher pressure, you increase statistics but need stronger windows to keep the angular resolution at the same level so you increase the energy loss in the target, and so on. Taking into account all those effect accurately required a *Monte Carlo* simulation.

A cryogenic target requires windows to conceal the gas volume, in our case, the large beam size required very large windows, and therefore a large deformation of the windows is expected. The windows material need to be strong enough not to deform too much, but made of light compounds to avoid important energy straggling of the particle going out of the target. The possibility to use Havar windows for the cryogenic cell was quickly dropped because of its dramatic effect on low energy ^{3}He, the presence of tungsten and other large Z compounds strongly increasing the energy loss and energy straggling in the material. Instead, we chose to use Mylar foil and pickup the 12 μm thick one as a good compromise between energy loss and strength.

Calculation using the finite element numerical method performed at IPN predicted a 1 mm deformation at 1 bar leading to a 4 mm (2 mm of nominal thickness plus two 1 mm of deformation per windows) total thickness in the central part of the target. After the first test with the cryogenic target this value was found to be underestimated by a factor of three, leading to a total thickness around 10 mm in the central part. The target was also expected to run at a temperature of 26 K, however the tests showed that only 30 K could be reached at 0.7 bar instead of the expected 1 bar. During the preparation phase many combination of temperature and pressure have been explored, only the relevant results for the expected and real cryogenic target are presented in Table 3.1.

Simulations were run for different targets assuming the following conditions:

- ^{11}Li beam at 50 AMeV ± 20 MeV (Δ p/p = 6%, see Sect.2.1)
- L=1 transfer reaction
- PPAC reconstruction on target of ±1 mm
- Coincidence with zero degrees detectors

The results given in Table 3.1 are obtained with a target simulated as a cylindrical object. In reality, the windows gets deformed and take a hyperbolic cosine shape[1] that can be measured using a laser. Any mismatch in the target alignment or the beam position on target will influence strongly the energy loss correction leading to additional systematic errors that are not here taken into account. In the same way, the problem of the fluctuating pressure and temperature and therefore density inside the target lead to bigger statistical error. One can hence conclude that the values of the resolution given here are underestimate.

			Thickness (mg/cm^2)			
e (mm)	P (bar)	T (K)	^{2}H	^{12}C	Total	σ (keV)
4	1	26	0.75	1.54	2.29	850
10	0.7	30	1.13	1.54	2.67	1170

Table 3.1: *Summary of the study for the cryogenic target. The first case is the expected running conditions, the second case is the effective conditions.*

The standard solution for deuterium target is the use of CD_2 target. Those solid target are made of polypropylene where the proton of the hydrogen atoms has been substitute by a deuterium nuclei. The evaluation of the thickness of these targets is a difficult task, where the total mass need to be estimated accurately. We intended to use a 1.5 mg/cm^2 target, but in order to check the target thickness, we use the test experiment, ^{9}Li(d,^{3}He), and found a larger value of 1.9 mg/cm^2 (see Sect.4.7.1).

	Thickness (mg/cm^2)			
e (μm)	^{2}H	^{12}C	Total	σ (keV)
14.2	0.38	1.13	1.5	932
18.0	0.48	1.43	1.9	1050

Table 3.2: *Summary of the study for solid CD_2 target. The first case is the expected target thickness, the second case is the actual deduced target thickness from the data analysis.*

The benefits of the cryogenic target at 30 K and 0.7 bar were too small, only a factor of three in the statistics, compared to the difficulty to run the target in

[1]The shape of a suspended wire at equilibrium

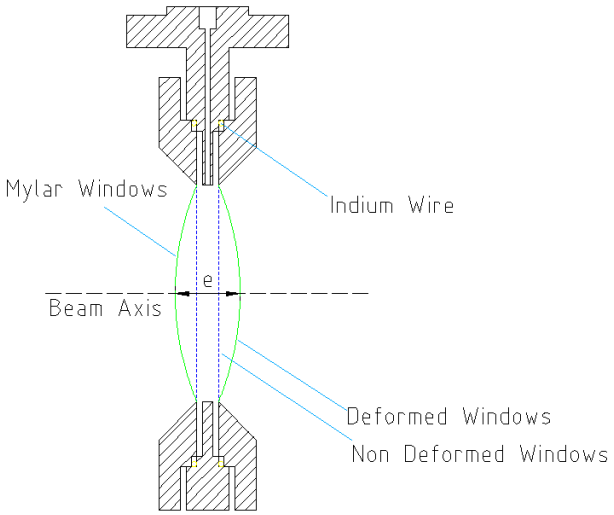

Figure 3.8: *Drawing of the cryogenic target cell designed for this experiment. The cell is the last stage of the cryogenic target, where the gaz is kept at constant pressure and temperature. The effective thickness of the target (denote as "e" on the drawing) is a decisive parameter for the experimental resolution.*

nominal condition during the whole experiment and the loss of beam time due to the necessity of opening the chamber during the experiment to switch targets. The solution of the solid CD_2 target was finally kept.

3.2.4 Particles identification

Time of Flight - Energy (TOF-E) identification method allow to determine the mass of the detected particle. The time of flight t of a particle of kinematic energy E and mass A along a path of length d is given by the following formula:

$$t = d\sqrt{1 - \frac{A^2}{E^2}} \tag{3.2}$$

Energy Loss - E (ΔE-E) identification method allow to determine the mass and charge of the detected particle. The Bethe-Block formula giving the following relation between the energy loss ΔE of a particle of mass A and kinematic energy E crossing a layer of material of thickness x_m.

$$\Delta E \approx x_m \frac{2\pi n}{m_e} \left(\frac{e^2}{4\pi\epsilon_0}\right)^2 AZ^2 \frac{1}{E} ln(\frac{4m_e}{AI}E) \tag{3.3}$$

Choice of thin silicon detectors

The identification of ^{3}He with low energy coming from the reaction requires discrimination from the other light particles, especially ^{4}He and ^{3}H. The Time of Flight identification method can not be used to achieve this goal, ^{3}He and

^{3}H having the same mass. The simulation tested different thickness for the thin silicon detector in front of the MUST2 DSSD. Finally the choice of very thin 20μm thick detector was made because of its low threshold for ^{3}He detection. The SSSD detectors were expected to show off a resolution of 150 keV (FWHM), and this value was used for the simulation. However the alpha calibration of the real detectors showed a better resolution of 112 keV (FWHM) (see Sect.4.5.1). The time of flight resolution is assumed to be 500 ps (FWHM) taking into account the MUST2 time resolutions and the PPAC time resolutions.

Particles are generated with a Gaussian energy distribution centered at 15 MeV $\pm$ 15MeV for He isotopes and 4MeV $\pm$ 5MeV for H isotopes to produce identification plots.

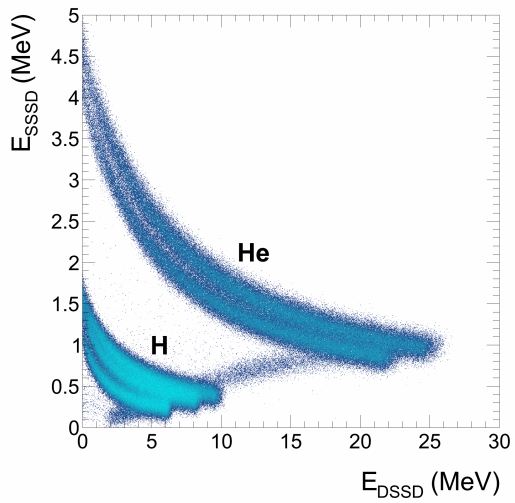

Figure 3.9: *E-ΔE identification of the light particle using the SSSD and MUST2 DSSD.*

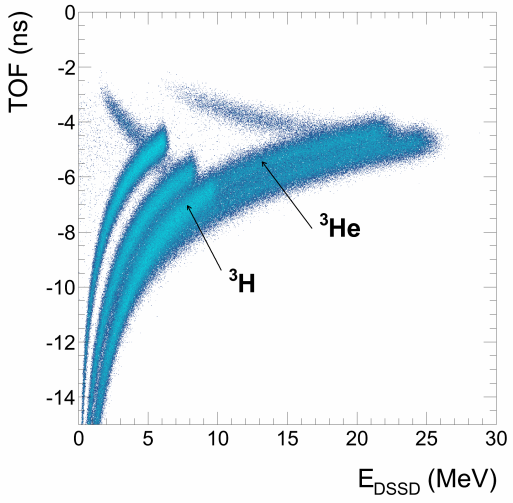

Figure 3.10: *E-TOF identification of the light particle using the time of flight between the target and the MUST2 DSSD.*

The plot presented in Fig.3.9 shows how the separation of ^{3}He from other light particles is possible using the SSSD and a ΔE-E identifications plot, while MUST2 alone offer only the TOF-E identification plot visible in Fig.3.10. The latter identification does not help to distinguished ^{3}He from ^{3}He, resulting in a lower identifications limits around 10 MeV. At higher energy, the α-particles are mixing with the ^{3}He and the separation is not effective.

The identification plots shown here demonstrate how the light particle can be separated, the chap.4 explained in details the many refined treatment such as the correction of the SSSD thickness and multiple variable selections of the event used to achieve a very good particles separation.

Residues

^{10}He is known to be an unbound nucleus and therefore can not be detected directly, instead it will decay into lighter and bound Helium isotopes ^{4,6,8}He. Previous measurement has been channel dependent, therefore we aimed to make a channel free measurement, by detecting both ^{3}He ejectile and the ^{4,6,8}He from decay. Without indication on correlation in the decay of ^{10}He we use a phase space generator to cover the possible configurations. The event generator first compute the four momentum of the ^{10}He using the two body kinematic associate with the reaction. Then the phase space generator is used to compute the four momentum of the neutrons and remaining He isotope. The weight of each configuration is compute and stored in the output data in order to renormalized the spectra. The following decay channels have been explored :

- ^{10}He $\rightarrow$ ^{8}He+n+n
- ^{10}He $\rightarrow$ ^{6}He+n+n+n+n

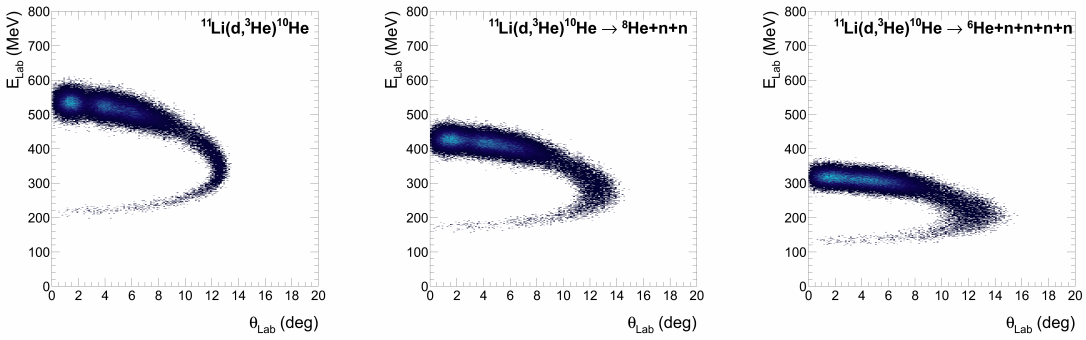

Figure 3.11: *The kinematics line of the heavy residues in three cases: (left) assuming a bound ^{10}He, (center) assuming a ^{8}He+n+n decay, (right) assuming a ^{6}He+n+n+n+n decay (from a 3 MeV state)*

The Fig.3.11 shows off the effect of the decay on the energy of the heavy particles while the angular distribution is not changed much. We can use this information as a starting point to design the zero degrees detections.

In order to identify heavy residues, as well as separate them from the beam particles, we used one MUST2 telescope. The later was protected from the beam using a two-stages plastic scintillator. The size of the plastic detector was decided after simulations exploring the following points:

- The plastic should allow the identification He and Li isotopes
- The plastic can sit in between the T1-4 mechanics

- The plastic stop most of the beam particles

A good compromise was found with a first stage of 20 mm and a second stage of 30 mm, allowing a rather good identification of particle stopping the plastic. The simulation stated a standard BC400 scintillator and a energy resolution of 5% based a previous experiment using such PM and scintillator. To check the identification of particles around zero degrees we used the generation of particles with a Gaussian energy distribution centered at 350 MeV ± 100 MeV to cover a large range of particles energy. The emitted particles are ^{3}He, ^{4}He, ^{6}He, ^{8}He and ^{9}Li, ^{11}Li and got the identification plots presented in Fig.3.12 for the plastic telescope and Fig.3.13 for the zero degrees MUST2 telescope.

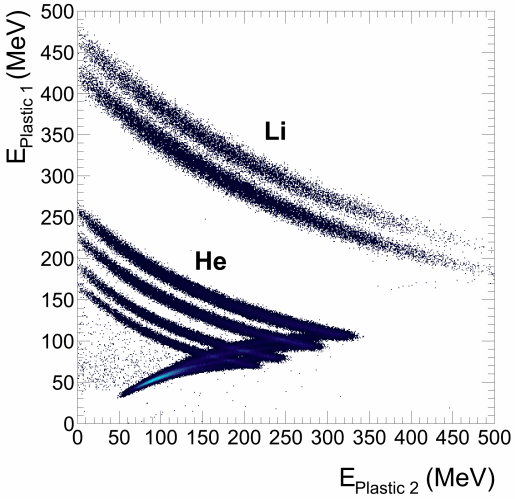

Figure 3.12: *E-ΔE identification plot in the zero degrees plastic. The beam particle are stopped inside the plastic detector as well as low energy He isotopes. Higher energy He isotopes cross the second stage plastic and go in the MUST2 telescope.*

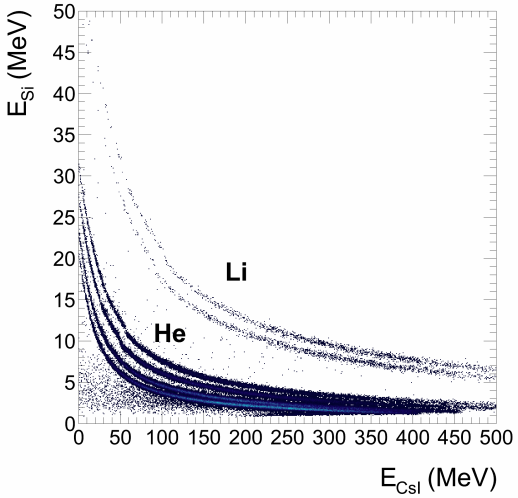

Figure 3.13: *E-ΔE identification plot in the zero degrees MUST2 telescope. All the particle are identified correctly.*

3.2.5 Background evaluation

When a beam particle interacts with a target particle a transfer can occur, but also processes where the internal structure of the nuclei is not probed. These corresponds to pure phase space events, where there is no correlation between the initial and final state. Different phase space have been investigated using the TGenPhaseSpace [Jam68] function from CERN ROOT library. This method rely on a *Monte Carlo* methodology to populate the whole phase space. The following phase spaces have been explored :

- ^{11}Li + ^{2}H → ^{3}He+^{8}He+n+n

- ^{11}Li + ^{2}H → ^{3}He+^{6}He+n+n+n+n

Figure 3.14 and Fig.3.15 show the associated contributions to the kinematics plot of the ^{3}He of interest. The blue line is set at the threshold where the associated phase space can start to contribute.

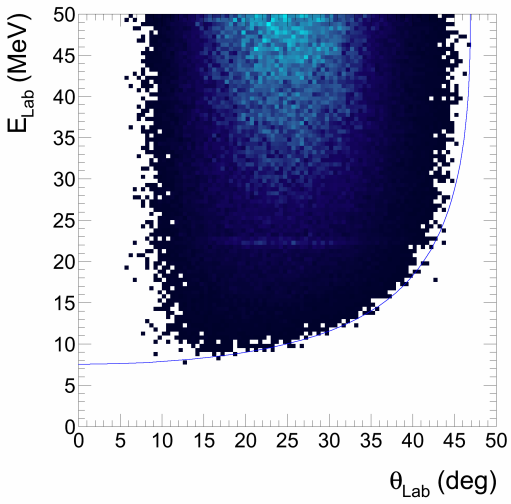

Figure 3.14: *The ^{11}Li + ^{2}H → ^{3}He+^{8}He+n+n phase space represented in the E_{Lab}-θ_{Lab} space. The blue curve indicate the ^{8}He decay threshold.*

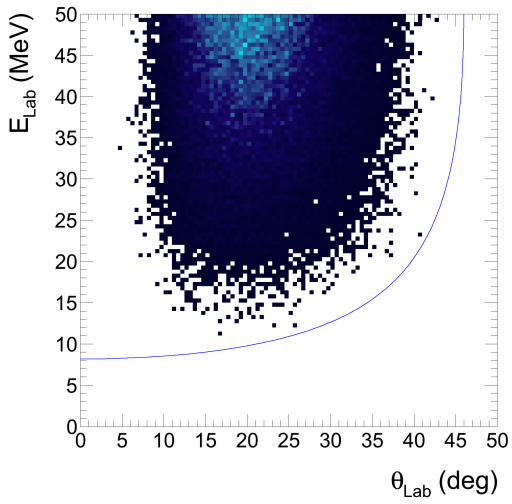

Figure 3.15: *^{11}Li + ^{2}H → ^{3}He+^{6}He+n+n+n+n phase space represented in the E_{Lab}-θ_{Lab} space. The blue curve indicate the ^{6}He decay threshold.*

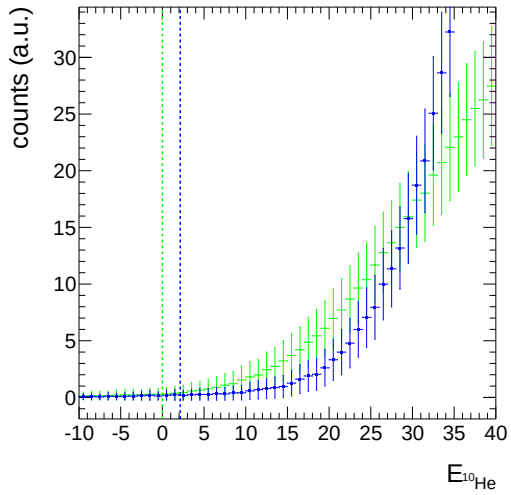

Figure 3.16: *^{11}Li + ^{2}H → ^{3}He+^{8}He+n+n (green) and ^{11}Li + ^{2}H → ^{3}He+^{6}He+n+n+n+n (blue) phase space contributions to the excitation energy spectra of ^{10}He. The green and blue vertical line indicate respectively the ^{8}He and ^{6}He decay mode threshold. All detection effect are taken into account as well as coincidence around zero degrees.*

Figure 3.16 presents the associated excitation energy spectra contribution. All the phase space events are not equivalent and their weight has to be taken into account to be representative of the reality. These phase space contributions can

later be used to fit physical background in the final spectra. Their normalization remain a free parameter of the analysis. Note the error bars in Fig.3.16 due to the *Monte Carlo* methods used here. The error bars can be decreased using more statistics but the running time, as well as the volume of the generated file, are limitations. The more bodies the phase space involves, the more the weight of each configuration is small and the more the need of statistics is high. Therefore, many body phase space are more delicate to evaluate.

3.3 Post-experiment simulations

The *post-experiment* simulations aimed at understanding the detection setup in the effective conditions of the experiment. All the results presented in this section take into account the real beam position and emittance, as well as the measured position of the detector (see Sect.2.7). Therefore direct comparison between the simulated data and the experimental data could be performed. The simulation stated a 18 μm thick target (1.9 mg/cm^2), ^{9}Li is assume to have a Δp/p =0.2%, ^{11}Li Δp/p =6%, and the PPAC reconstruction on target extracted within $\pm$1 mm.

3.3.1 Resolution and efficiency

All the values in Table 3.3 are given for the ground state (1 MeV above the ^{8}He+n+n state for the ^{10}He case). In the case of (d,^{3}He) reactions, the resolution is getting better with the excitation energy, because the ^{3}He is produced with a higher energy, decreasing the energy straggling in the target.

Reaction	Cross section	σ (keV)	Inclusive Eff. (%)	Exclusive Eff. (%)
^{9}Li(d,^{3}He)	flat	818	14.4	1.9
	L=1	944	25.6	19.2
^{11}Li(d,^{3}He)	flat	865	20.6	12.2
	L=1	1019	28.0	19.3
^{9}Li(d,d)	flat	561	0.5	2.8
^{11}Li(d,d)	flat	939	0.9	2.8

Table 3.3: *Summary of the post-experiment simulations. Inclusive efficiency correspond to the event where an ^{3}He has been detected in the T1-4 (T7 for (d,d) cases) wall, while the exclusive efficiency required event with an ^{8}He (^{9}Li or ^{11}Li for (d,d) cases) in the zero degrees detection.*

All these information are very valuable during the data analysis (see chap.4) where comparison between the expected and observed resolution sheds light on analysis errors.

3.3.2 Solid angle

In order to extract the angular distribution associated with the reaction, one needs the solid angle in the center of mass $d\Omega_{CM}$ (see Sect.4.7.2). $d\Omega_{CM}$ is obtained using a flat cross section simulation and given by:

$$d\Omega_{CM} = \frac{N_{detected}(d\theta_{CM})}{N_{emitted}} \cdot 4\pi \tag{3.4}$$

The *Monte Carlo* approach and the NPTool methodology is here decisive, because the real and simulated data are analyzed in the same way, we insure an homogeneous event selection. Therefore, we minimize the systematic error on $d\Omega_{CM}$ induced by the selection of the particle of interest. We can defined $d\Omega_{CM}(C)$, where C is the collection of all the conditions used for the real data, *i.e.* cuts, thresholds and coincidences.

$$d\Omega_{CM}(C) = \frac{N_{detected}(d\theta_{CM}, C)}{N_{emitted}} \cdot 4\pi \tag{3.5}$$

For all the reactions, the solid angle is obtained from the simulation, using a realistic beam and taking into account the coincidence with heavy particles around zero degrees. The (d,^{3}He)^{10}He case is illustrated in Fig.3.17, where the effect of coincidence is visible. A diminution as well as a shift of the maximum is noticeable. Since the solid angle is used in the normalization of the angular distribution, the account of coincidences is crucial in the extraction of physical data. A complete and accurate simulation plays here a decisive role.

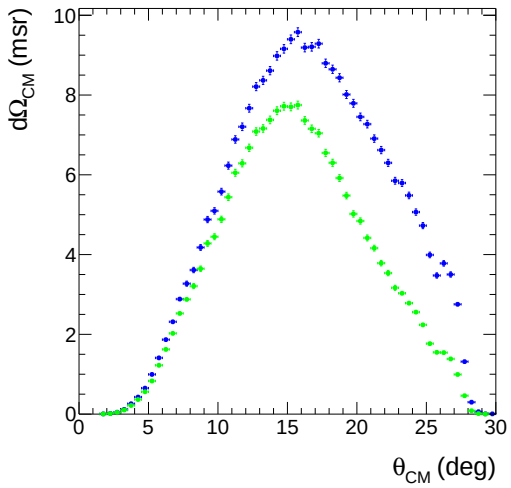

Figure 3.17: *The solid angle coverage of the detection system deduced from the simulation, before (blue) and after (green) coincidences with the zero degrees ^{8}He. The coincidences does not only reduced the detection rate but also the shape of the efficiency, having direct of incidence on the angular distributions.*

Chapter 4

Data Analysis

4.1 Introduction

This part will present the methodology used to analyse the data from our multi-detector set-up. Each time a specific case was identified a diagnostic method was implemented and solution found within the same software that treats the rest of the channels. This approach of "no exception methodology" tend to reduce at maximum the user dependent operation. In this Chapter, the beam identification and tracking will be first presented. The calibration of the MUST2 and SSSD detector will be discussed as well as the particles identification. In the last part of the Chapter, the extraction of the excitation energy and angular distribution, that contains the structure information will be discussed.

4.2 Beam particles identification

In order to identify the incident particles on target, two plastic detectors were set at the F2 and F3 focal plane. The F2 plastic was 2 mm thick while the F3 plastic, was 0.3 mm thick. The time of flight between F2 and F3 versus the ΔE in F2 allows the identification of the incident particles as presented in Fig.4.1. For the purpose of identification and purity evaluation, the down scale singles event has been used, an important contamination of tritons exists, however their low energy loss in the F2 plastic and PPAC forbid their detection. The ^{11}Li beam purity, excluding tritons, reaches 40.4%. The main contaminants were ^{15}B (49.0%), ^{9}Li (3.2%), ^{6}He (2.8%) and ^{8}He (0.2%). These contributions can be completely removed during the data analysis using previously mentioned identification plot. Moreover, the ^{15}B, with an intensity equal to the one of ^{11}Li, provided additional data on the ^{15}B(d,^{3}He)^{14}Be reaction, to be analysed in the future.

The ^{9}Li beam purity, excluding tritons, reached 73%, contaminated mainly by ^{6}He (10.5%). During the ^{9}Li run, the F3 plastic was removed to reduce the associate carbon background it may produce. The incident particle identification was done using the time of flight between F2 and the PPAC and the ΔE in F2. One cut was made for each PPAC to avoid any loss of statistics. An example is given in Fig.4.2.

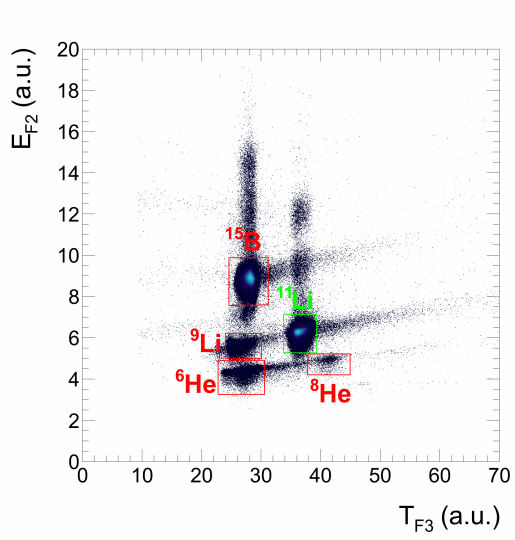

Figure 4.1: *Identification plot of the incident particles using the F2 and F3 plastic information during the ^{11}Li runs. The main contaminants of the ^{11}Li beam are here clearly visible.*

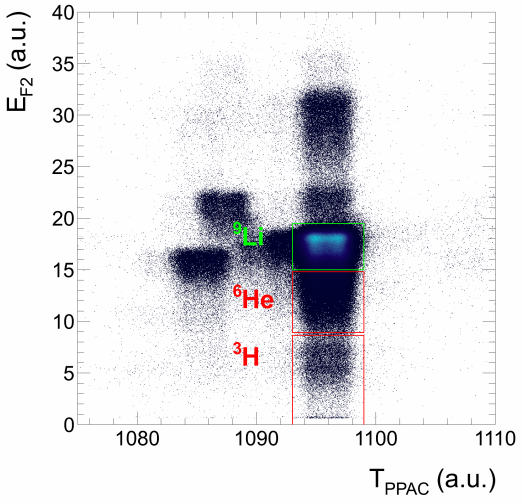

Figure 4.2: *Identification plot of the incident particles using the F2 plastic and F3 PPAC information during ^{9}Li runs. The main contaminant, ^{3}H is not visible because of there low energy loss in the PPAC and Plastic.*

4.3 PPAC Beam Tracking Detector

4.3.1 Calibration and efficiency

The PPAC position information is deduced from a timing measurement $T_{right}, T_{left}, T_{bottom}, T_{top}$ between the two ends of the horizontal (X) or vertical (Y) delay line. The calibration of the four PPAC (eight layers) was made injecting a pulser signal at one side of the delay line and measuring the delay at the other side and knowing the length of the delay line. The calibration gives the offset x_0 and y_0 and the coefficients c_x and c_y that gives the following formula for the position of interaction in the PPAC:

$$x = c_x(T_{right} - T_{left}) + x_0 \tag{4.1}$$

$$y = c_y(T_{bottom} - T_{top}) + y_0 \tag{4.2}$$

The fast signal coming from the anode was used as a stop for time measurements started by the F2 plastic. The efficiency of the PPAC array was evaluated using down-scaled single (DS) events of the F2 plastic. The set of the four PPAC gives a total reconstruction efficiency of 56% for ^{9}Li beam, and 71% for ^{11}Li beam.

4.3.2 Beam Tracking

Using the different parameters shown in Fig.4.3, we can deduced the beam particle position and incident angle on target through the measured beam position in two different planes by the formula :

$$X_{Target} = X2 + (X2 - X1)\frac{|Z2_X|}{Z2_X - Z1_X} \tag{4.3}$$

$$Y_{Target} = Y2 + (Y2 - Y1)\frac{|Z2_Y|}{Z2_Y - Z1_Y} \tag{4.4}$$

$$\vec{b} = (X2 - X1, Y2 - Y1, Z2 - Z1) \tag{4.5}$$

$$\theta_b = \arccos\left(\frac{\vec{b}.\vec{n}}{|\vec{b}|}\right) \tag{4.6}$$

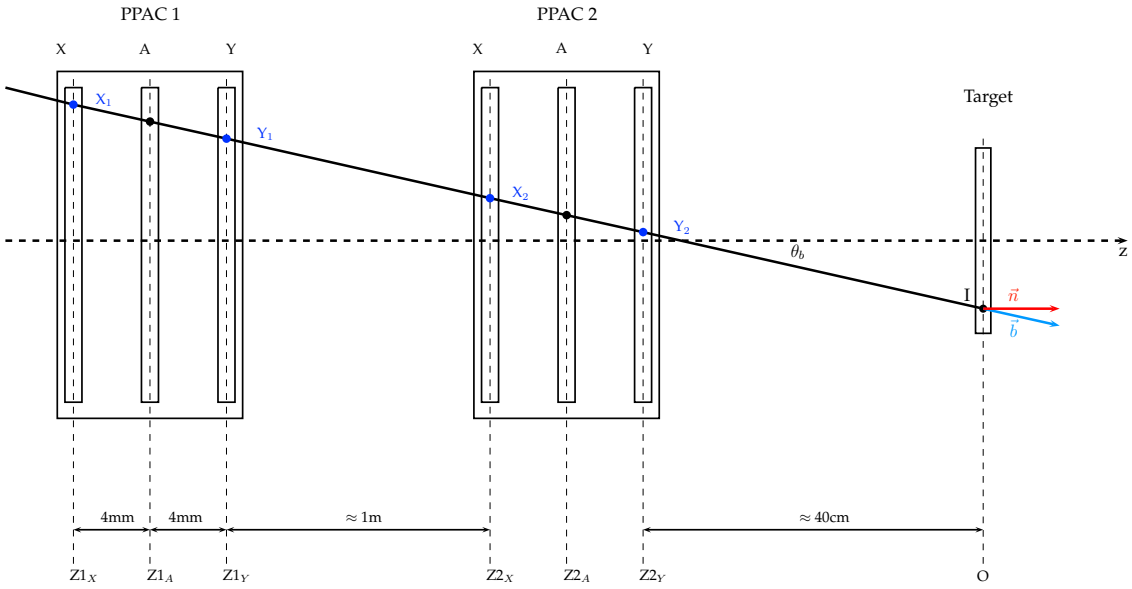

Figure 4.3: *Schematic view of the PPAC layout and definition of the different parameters needed for the beam tracking. The position (X_1,Y_1,Z_1) and (X_2,Y_2,Z_2) are defined here.*

Beam	$\bar{x}$ (mm)	σ_x (mm)	$\bar{y}$ (mm)	σ_y (mm)	σ_{θ_x} (mrad)	σ_{ϕ_y} (mrad)
^{9}Li	0.2	3.9	1.8	2.4	8.9	13.3
^{11}Li	1.8	6.2	-0.1	6.1	10.7	6.7

Table 4.1: *The beam position (m_x,m_y) width (σ_x,σ_y) and emittance (σ_{θ_x},σ_{ϕ_y}) on the target according to the PPAC reconstruction.*

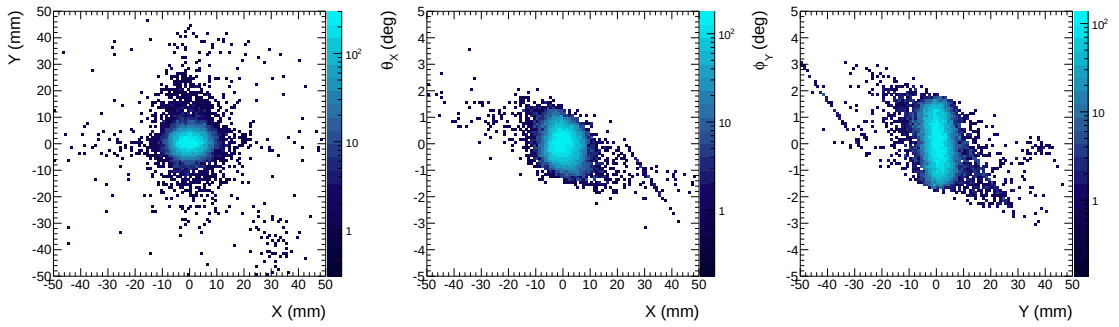

Figure 4.4: *^{9}Li beam profile on CD2 target (left), beam emittance on X axis (center) and Y axis (right)*

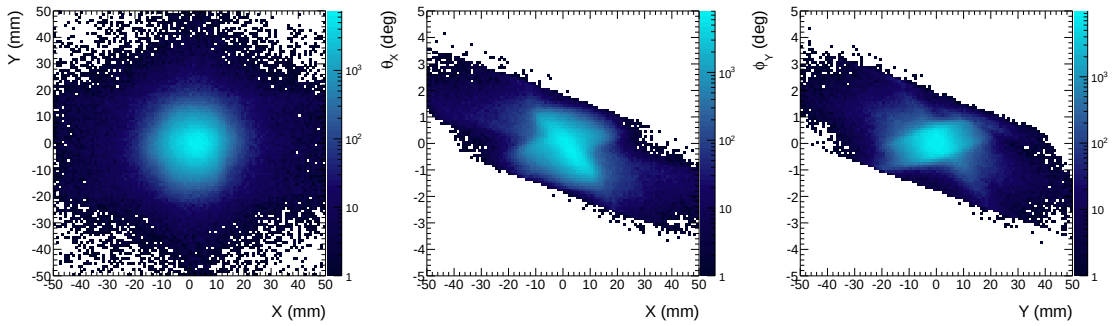

Figure 4.5: *^{11}Li beam profile on CD2 target (left), beam emittance on X axis (center) and Y axis (right)*

The beam profile and emittance are visible on Fig.4.4 for ^{9}Li and Fig.4.5 for ^{11}Li. The projected values, summarized in Table 4.1, are used in the simulations (see Sect.3.3). The ^{11}Li distribution is much broader than the ^{9}Li one, because the full acceptance of the RIPS line is used in the former case while narrow slits are used in the latter.

Checking the PPAC calibration and position

The first excitation energy spectra obtained using the initial PPAC parameters led to peak widths inconsistent with the simulations. To check the validity of the trajectory reconstruction, we firstly used the image of the target frame. However it was found that this image can be kept consistent even under transformations such as mirror transformation (X=-X or Y=-Y or both) and rotation (swapping X and Y). In a second step, we used the elastic scattering ^{9}Li(d,d) as a reference. This reaction has several features that make it a good test case. First, the statistics is higher than for transfer reaction, and thus, the spectra are easier to interpret. Secondly, the signal resolution is quite insensitive to the target thickness, so we can put this effect aside and concentrate on only one parameter.

Table 4.2 shows clearly that results using an inversion of the X axis, are the

Modification	Mean (MeV)	Sigma (MeV)
Normal	0.06	1.24
-X (retained modification)	0.05	0.65
-Y	0.11	1.47
-X and -Y	0.04	0.79
Inv. X/Y	0.47	1.63
-X and Inv. X/Y	0.36	1.68
-Y and Inv. X/Y	0.09	1.44
-X and -Y and Inv. X/Y	0.10	1.46

Table 4.2: *Checking of the PPAC reconstruction on Target with possible inversion and influence on position and resolution of the ^{9}Li ground state populated by the $^{9}Li(d,d)^{9}Li$ reaction.*

only ones compatible with the predicted 560 keV of the simulation. For the rest of this study, this correction will be used. We also checked the dependence of the signal on the target position along the z axis. Table 4.3 does not show evidence of an offset on the target position.

Modification	Mean (MeV)	Sigma (MeV)
-2mm	0.90	0.64
-1.5mm	0.70	0.64
-1mm	0.49	0.63
-0.5mm	0.25	0.63
0mm	0.05	0.65
1mm	-0.42	0.65

Table 4.3: *Influence of the target position along beam axis, the target position is given with respect to the theoretical one.*

4.4 MUST2 Telescopes

4.4.1 Energy Calibration

The DSSDs feature 128 strips on each side, read out by two MUFEE cards. The X and Y signals are of different polarities and coded on the same 14 bit ADC by shifting the ground line. Therefore, the X signals, of positive polarity, are coded from the channel number 8192 to the channel number 16384 whereas the Y strips signals, of negative polarity, are coded from channel number 8192 to channel number 1. Prior to a source calibration, the pedestals of all the strips were realigned to the channel number 8192 value using a built-in functionality of the MUVI digital board.

Source	E_α (MeV)	Relative Intensity	$T_{1/2}$ (year)
^{239}Pu	5.15659(14)	70.77(14)	2.411 10^4
	5.11443(8)	17.11(14)	
	5.1055(8)	11.94(14)	
^{241}Am	5.48556(12)	84.8(5)	432.2
	5.44280(13)	13.1(3)	
	5.388	1.66(2)	
^{244}Cm	5.80477(5)	76.40(12)	18.1
	5.76264(3)	23.60(12)	

Table 4.4: *Three α source made of three different long-life isotopes.*

Three α source (^{239}Pu, ^{241}Am, ^{244}Cm) were then used to calibrate the strips. Nuclei from the source are particle unstable and will decay emitting α particles of well defined energy presented in Table 4.4. The energy of the main and satellite peaks were used to produce a realistic fit of the strips spectra and find the relation between the ADC output and the energy deposit.

One major problem in calibrating silicon detectors is the characterisation of their dead layer. This dead layer is made of a thin metallisation of aluminium needed for the charge collection, but also of a layer of inert silicon, for which the thickness is not accurately known. This dead layer reduces the energy of alpha particles entering the silicon detector, and may induce a systematic error on the calibration if not correctly taking into account. In order to get rid of this error we use the zero extrapolation method, presented in Fig.4.6, and performed the following five iterative steps:

1 Assuming a dead layer thickness (pure aluminium), the energies of α particles from the source are calculated using an energy loss table.

2 Linear fit $E_{Calibrated} = a + bE_{channel}$ is performed for each strip using the previously mentioned energies.

3 The position of the zero energy point is extrapolated $E_{\text{Calibrated}} = 0 = a+b(E_0)$ for each strip.

4 The distance $\delta_0 = E_0 - E_{Pedestal}$ is evaluated for each strip.

5 If the average of δ_0 over all strips is small enough (typically 0.1 channel), the dead layer thickness is validated for this telescope. Otherwise, the dead layer assumption is modified and the protocol goes back to step 1.

An automatic routine converge to a dead layer thickness allowing a zero extrapolation average dispersion around 0.1 channel. The resulting values are presented in Table 4.6.

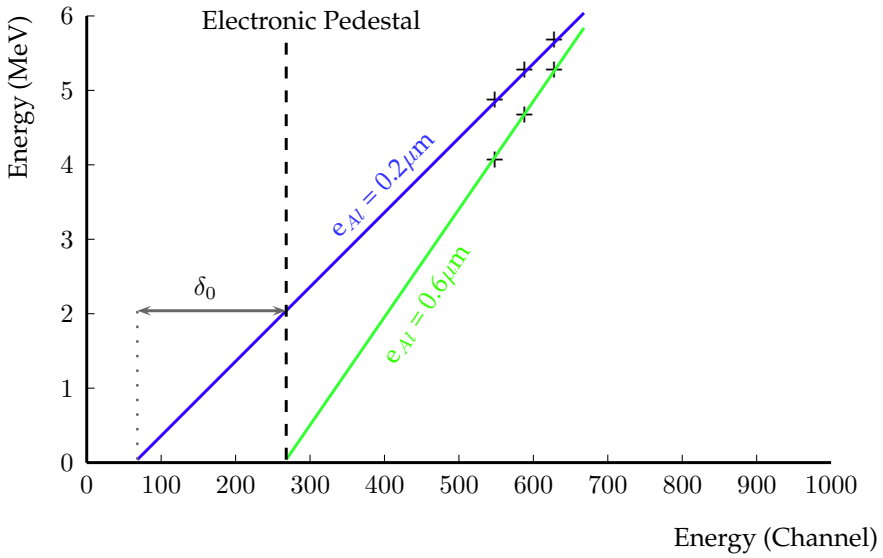

Figure 4.6: *Scheme of the zero extrapolation method:The aluminium equivalent dead layer is adjusted so zero energies deduced from the calibration is aligned with the electronic pedestal.*

Because each detector has its own dead layer thickness, we can sum up all the strip only on a detector basis. The source peaks are then fitted using a realistic shape, sum of Gaussian functions of same width and fixed relative height, as shown for telescope 1 in Fig.4.7 and summarized for all telescopes in Table 4.5. The deduced widths of the peaks show a typical 38keV FWHM resolution with a small dispersion.

Detector	σ_{Pu} (keV)	σ_{Am} (keV)	σ_{Cm} (keV)
1	15	16	16
2	16	18	15
3	17	19	15
4	17	16	16

Table 4.5: *Table of the deduced resolution (σ) for each telescope and each source peak. The average σ over all the values is 16.3 keV, giving a 38 keV FWHM resolution*

This method enfirms a particle independent calibration, the detector and its electronics is calibrated in energy and the deduced dead layer thickness can then be used to introduce particle dependent corrections on the energy.

A systematic study was performed using a pool of α-source calibration data from four experiments, RRC66, this work, RIBF57, an ^{24}O(p,p') experiment performed at RIKEN in 2010, e569s, a ^{14}O(d,^{3}He) experiment at GANIL in 2009 and e552, a ^{68}Ni(d,^{3}He) experiment performed at GANIL in 2011.

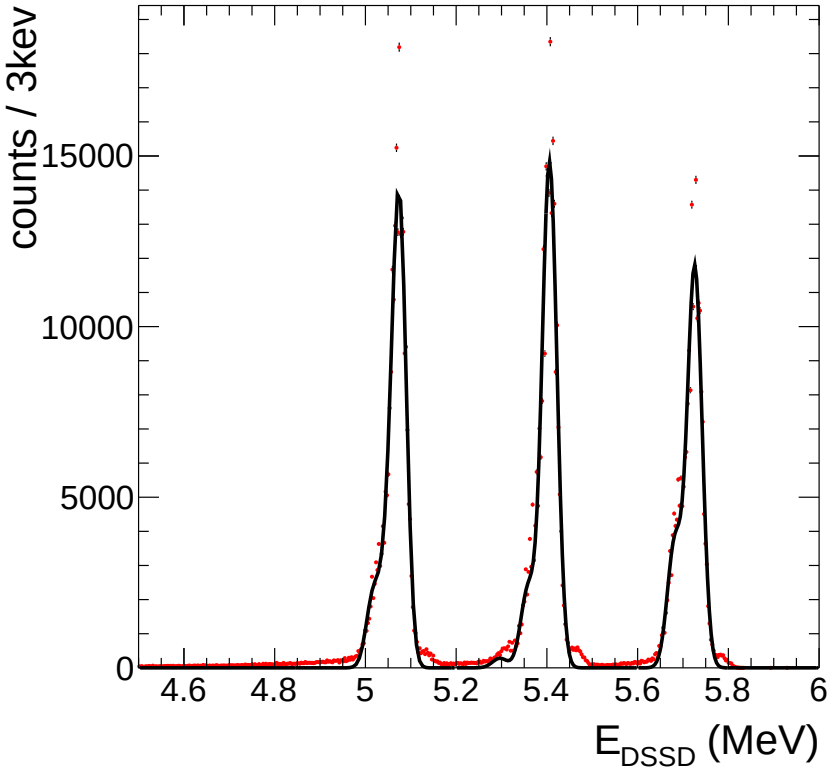

Figure 4.7: *Alpha source energy spectra obtain after summation of all the X strips of the telescope 1. The statisticsal error bars are represented around the red dots, while the black solid line is a realistic fit of the source signal. The asymmetric shape of the signal is due to the lower energies satellite peaks.*

Detector	Al Thickness	Detector	Al Thickness
1	0.50 μm	5	0.49 μm
2	0.65 μm	6	0.57 μm
3	0.66 μm	7	0.25 μm
4	0.57 μm	8	0.45 μm

Table 4.6: *Deduced Aluminium equivalent dead layer thickness on the entrance sides of the 300 μm thick silicon first stage of the MUST2 detectors using X strips measurement of the alpha energy.*

The same method has been applied to all MUST2 experiments and compatible values were found and are summarized in Table 4.7. This systematic study shows that values from one experient to the others are in agreement within 0.08 μm of

Aluminium, giving around 10% resolution to the method. One can note that the values deduced from the Y strips are generally higher than the one deduced from the X strips. This is understood as a charge collection deficit on the Y strips because of the low penetration of the alpha particles at this energy (around 30 μm of silicon). Further investigation needs to be performed to fully understand the discrepancies between all those values.

Using X Strips

Detector	RRC66*	RIBF57**	e569s*	e552*
1	0.50 μm	0.53 μm	0.54 μm	0.48 μm
2	0.65 μm	0.57 μm	0.58 μm	0.57 μm
3	0.66 μm	0.58 μm	0.62 μm	0.59 μm
4	0.57 μm	0.62 μm	0.65 μm	0.59 μm

Using Y Strips

Detector	RRC66*	RIBF57**	e569s*	e552*
1	0.67 μm	0.59 μm	0.57 μm	0.69 μm
2	0.65 μm	0.65 μm	0.70 μm	0.70 μm
3	0.69 μm	0.63 μm	0.71 μm	0.70 μm
4	0.77 μm	0.61 μm	0.62 μm	0.72 μm

*:(d,^{3}He) setup **:(p,p') setup

Table 4.7: *Deduced Aluminium equivalent dead layer thickness on the entrance sides of the 300 μm thick silicon first stage of the MUST2 detectors using X or Y strips measurement of the alpha energy.*

4.4.2 Time Calibration

The time calibration was performed for each strip using a time calibrator module, producing start and stop signals. The stop signal delayed by $N \cdot \tau$, τ being the fixed period and N varying so as to cover the whole range of the coder (640 ns). During the calibration process, the start and stop are inputs to the MUVI board and a calibration spectrum is obtained for each strip. A relative second order time calibration is then performed taking the first peak as reference. The summed spectrum of all the strips after the calibration of T1-4 is shown in Fig.4.8. The later gives a resolution 430 ps FWHM for the electronics, within specification of the MUST2 TDC.

The actual time resolution is worsen by the strip length. This resolution has to be correlated with time resolution of the 2 mm thick plastic located at the F2 focal plane that gives the stop signal. The resolution of the stop signal, a 2mm thick plastic located at the F2 focal plane, gives the final time resolution of the set-up. The total time resolution is evaluated at 1 ns.

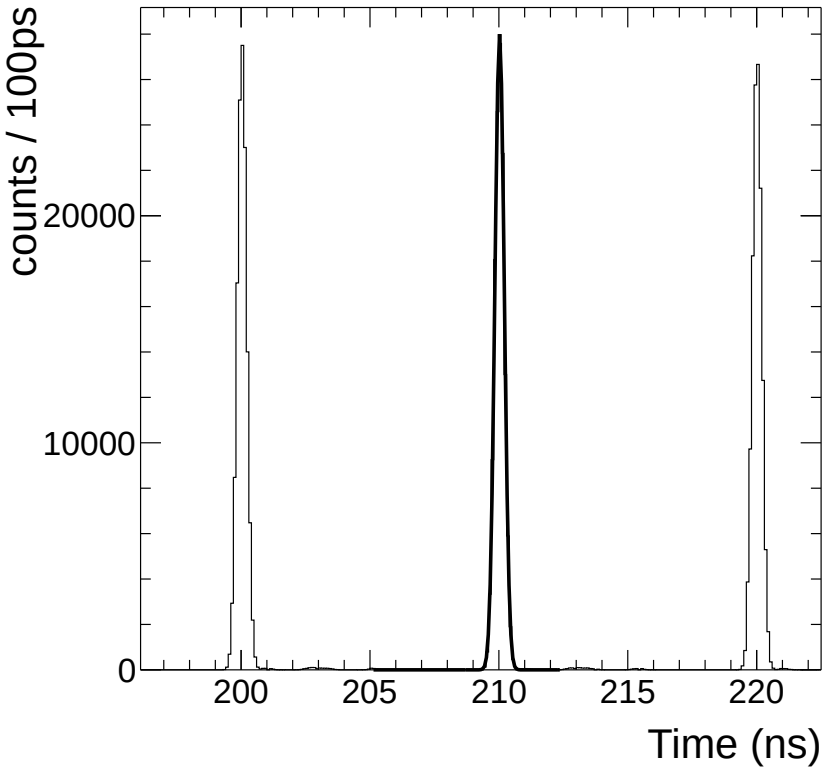

Figure 4.8: *Zoom on one of the Time Calibrator peak obtain after the calibration and summation over T1-4 Y strips. The black line show a Gaussian fit, giving 0.18 ns sigma, leading to a 430 ps resolution FWHM.*

4.4.3 CsI Calibration

The CsI stage consists of 16 modules made of CsI(Ti) scintillator read by a photo-diode. The response of each crystal is sensitive to the type of particle. It is therefore difficult to obtain an absolute calibration of the detector for particle heavier than proton. In the present work, the CsI stages were used for identification purpose only.

An identification plot using the strips energy and the uncalibrated CsI energy was done for each crystal of the telescopes. Selecting a given particle, in our case deuteron, inside those spectra, one can calculate the total energy of the particle knowing the ΔE and the thickness of the detector [Mou08] . A third order calibration was performed, allowing to sum up all the spectra of all the CsI modules together.

Once the particles were identified, the total energy of the particles was deduced using a similar fashion. A dE/dx table of ^{3}He in silicon was numerically reversed to obtain the total energy.

4.4.4 Event Selection

The algorithm for treating a MUST2 event, displayed in Fig.4.9, consists of three steps:

Pre-treat: This step aims at suppressing any non-physical contribution and at applying the calibration. During the calibration process using the alpha source, where all event should be of multiplicity one, the disfunctional strips are identified. There are many reasons for a strip not to work properly, the first one is a damaged bounding, leading to an absence of signal on one strip and the increase of signal on the adjacent ones. Electronics issues or damaged connectors are the other sources of trouble. A typical 5 to 10 strips were disabled, mostly on the exposed front sides of the silicon detector. Once those "dead strips" were disabled, we could apply a threshold on the calibrated data, in order to suppress background, and obtain an homogeneous threshold for all the strips.

Match X-Y: After this first step, all possible couples between X and Y strips are analysed and a condition on the energy matching is made, requiring that $|E_X - E_Y| < \epsilon$. The ϵ parameter is taken as three σ of the DSSD energy resolution. If possible couples remained unresolved at the end of the process, the event is rejected.

Match Time and Second stage: Finally for all the allowed coupled defined earlier, a search for associated time is performed. In the same way, the algorithm looks for associated Si(Li) or CsI event in geometrical correspondence.

The multiplicity of the event corresponds to how many X-Y couples have been successfully found for this event. We only kept events of multiplicity one (within T1-4) in our study, based on obvious physical argument.

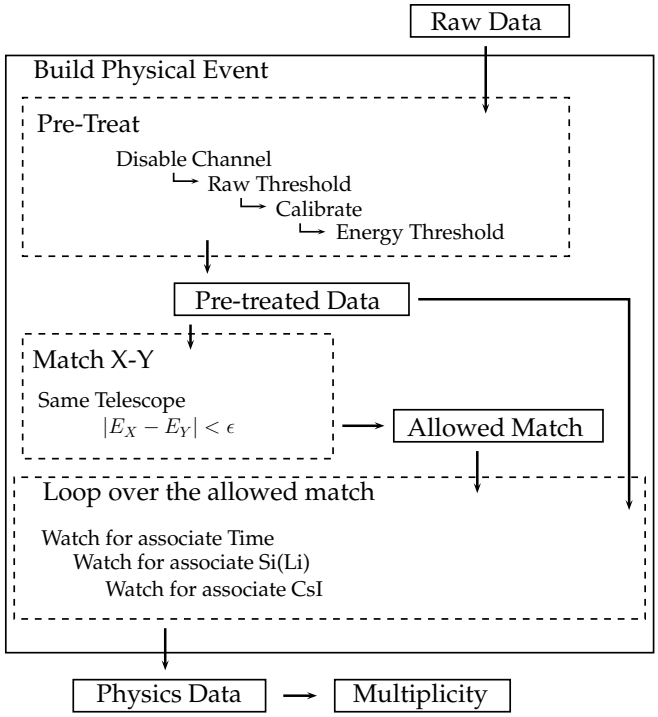

Figure 4.9: *Simplified scheme of the MUST2 event treatment algorithm. This technique ensures to suppress background without rejecting any physical event.*

4.5 20 μm Silicon detector (SSSD)

4.5.1 Energy Calibration

To perform an absolute calibration as well as an evaluation of the dead layer thickness of the four 20 μm thick silicon detector (SSSD), particles of known energies stopping inside the active part of the detector are used. The range of α-particles from the source listed in Table 4.4 exceeds the thickness of the detectors. To increase the effective thickness crossed by the α-particles, the source was set 12 cm below (for detector 3 and 4, above for detector 1 and 2) the nominal target position, as shown in Fig.4.10. As for the MUST2 silicon stage, we used the zero extrapolation method explained above. Because the detectors are closer to the source than in the MUST2 case, and because the particles came with a large angle, we observed a strong angular dependence and corrected this effect using position information given by the strips. This method gives values two times larger than the constructor specifications. However, as explained in the next part, such specifications are found not reliable. The deduced values of dead layer thickness are shown in Table 4.8.

After calibration and summation of all the strips, the source spectra are fitted (see Fig.4.11), using a sum of Gaussian functions as for the MUST2 DSSD case. The energy resolution deduced from this calibration is summarized in Table 4.9, leading to 112 keV FWHM resolution.

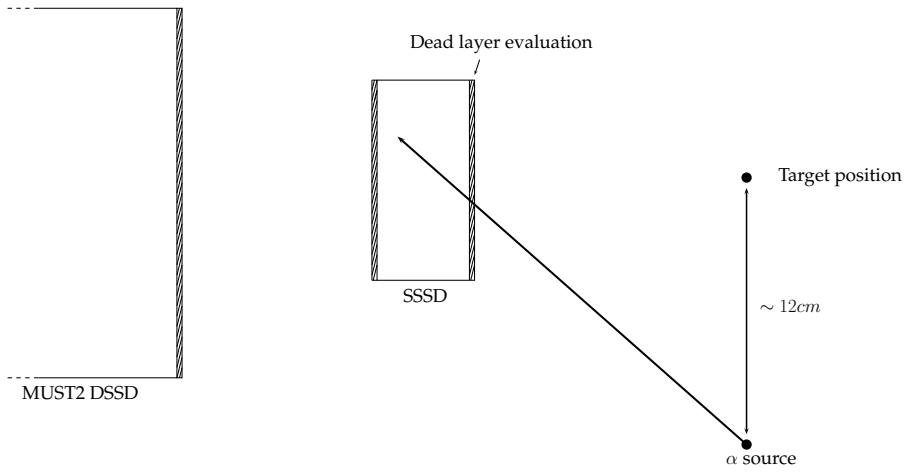

Figure 4.10: *Alpha source is moved such as the alpha particles are incident on the SSSD surface with a very large angle.*

Detector	Al Thickness
1	0.73 μm
2	0.74 μm
3	0.80 μm
4	0.74 μm

Table 4.8: *Deduced dead layer thickness of Aluminium on the entrance sides of the 20 μm thick silicon detectors. This value is to be compared to the manufacturer specification of 0.4μm of Al + 0.1μm of Si.*

Detector	σ_{Pu} (keV)	σ_{Am} (keV)	σ_{Cm} (keV)
1	43	43	47
2	51	52	50
3	49	51	60
4	37	45	44

Table 4.9: *Table of the deduced width (σ) for each detector and each source peak. The average width over all the value is 48keV, giving a 112keV FWHM resolution*

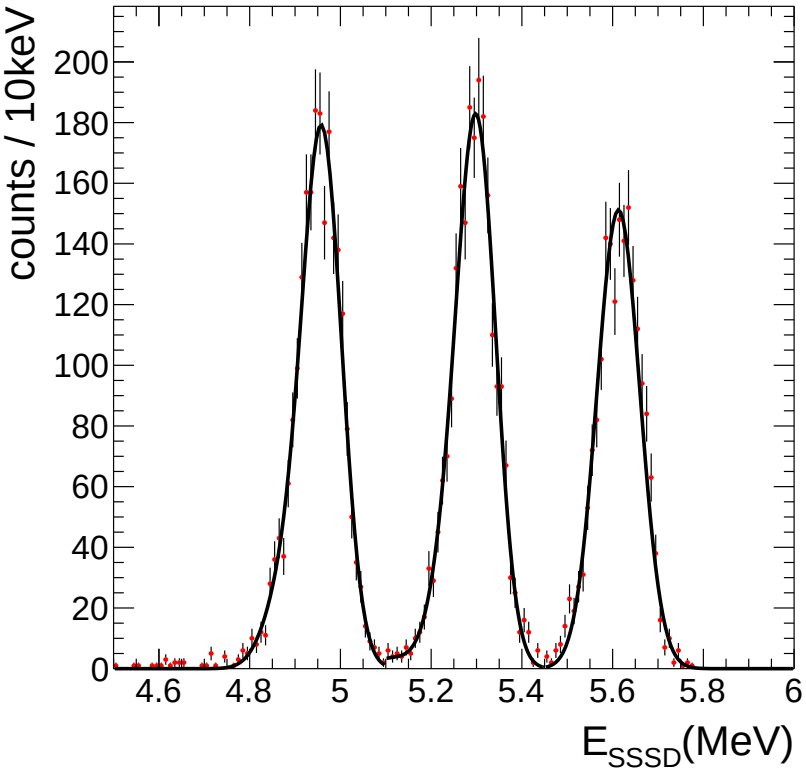

Figure 4.11: *α source energy spectrum obtained after summation of all the strips of the detector 1. The statistical error bars are represented around the red dots, while the black solid line is a realistic fit of the source peaks. Results of the fit are given in Table 4.9.*

4.5.2 Thickness measurement and correction

Thickness measurement

The SSSD were used for the purpose of E-ΔE identification at forward angle in conjunction with the MUST2 DSSD. Their thickness provided by the manufacturer varies from piece to piece, around 20 μm $\pm$1.5 μm. During the preparation phase of the experiment we performed test runs using the three alpha sources in transmission (see Fig.4.12). The energy of the α-particles was high enough to go through the SSSD stage after losing more than half of their initial energy.

Figure 4.13 shows the SSSD and DSSD summed energy spectrum for a single telescope. The peaks are much broader than in the case of the DSSD. The total energy resolution is dominated by the energy resolution of the SSSD, and shifted to lower energy by about 400 keV, due to the dead layer.

The E-ΔE spectrum is shown for the same telescope in Fig.4.14. It presents three very broad spots (light blue to dark blue). On the contrary, the same plot conditioned by a small area on the DSSD (block red point on the same figure), namely one pixel defined by the intersection of one strip X and one strip Y, show three very limited spot, evidencing strong thickness inhomogeneities.

Taking advantage of the MUST2 DSSD high granularity, we managed to map the absolute thickness of the detectors and obtained corrected E-ΔE spectrum. After selection of events corresponding to the highest energy peak (see Fig.4.14), the absolute silicone-equivalent thickness, corrected by the incident angle, is evaluated using the energy loss table and the MUST2 DSSD energy measurement, independently of the energy deposit in the SSSD. As represented in Fig.4.12 the silicon-equivalent thickness measured corresponds to the sum of the DSSD front dead layer, front and back SSSD dead layer, and SSSD active layer.

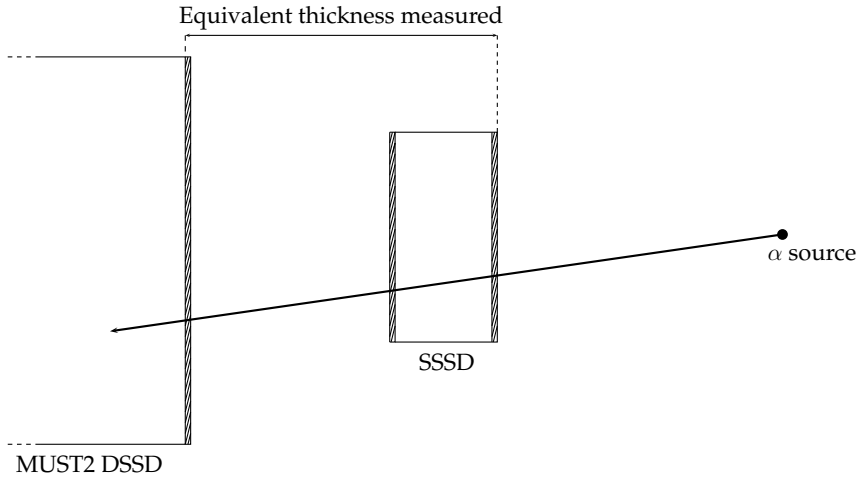

Figure 4.12: *Alpha source set-up at the target position, the small incident angle allow the alpha particles to cross the SSSD.*

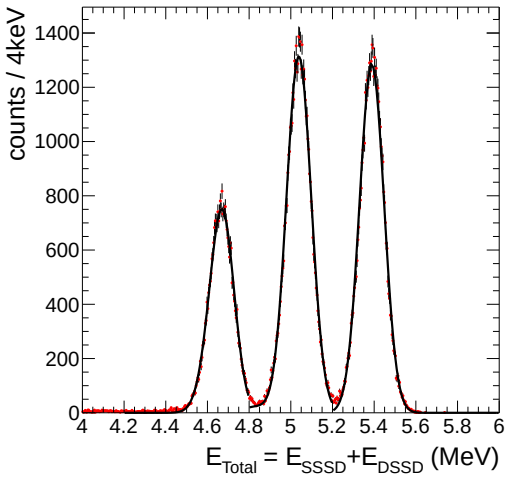

Figure 4.13: *The total energy spectra for telescope 1, where the alpha peak position is shifted at lower energy, due to the detectors dead layers. Note that the the first peak is twice smaller than the other two because lower energy alpha cannot go through the thicker part of the SSSD.*

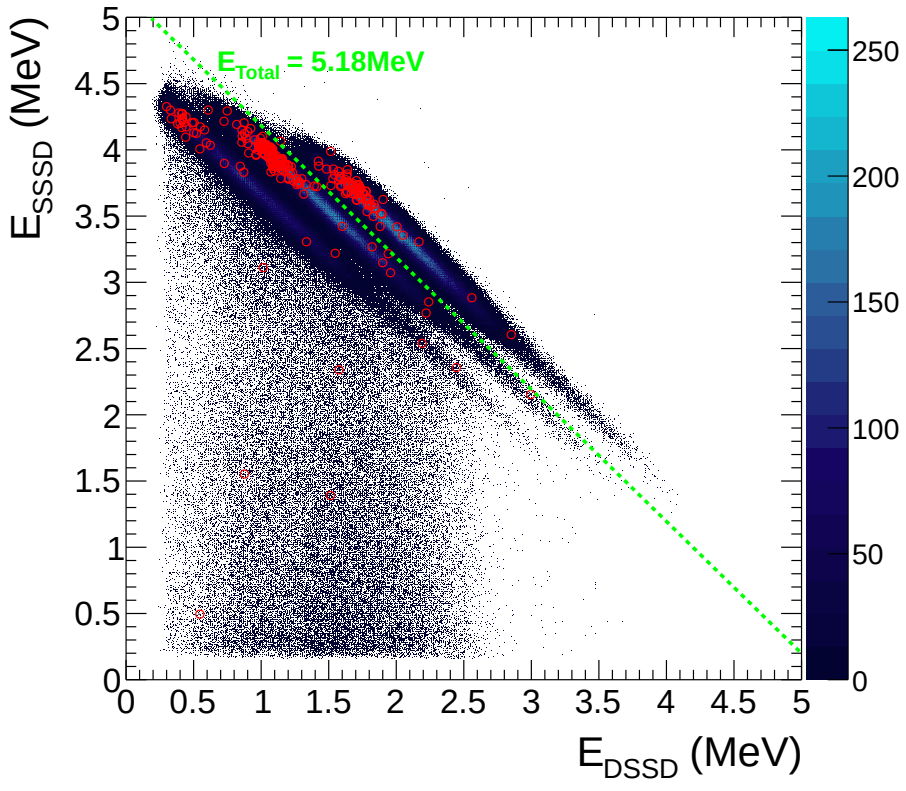

Figure 4.14: *E-ΔE spectra of the source for the full surface of telescope 1. The red circle show the same data conditioned by one pixel on the DSSD. The Green line show the graphical representation of the condition applied on E_{Total} to isolate the highest energy peak.*

Errors on the measured thickness are mainly systematic. They come from the energy loss table and the calibration of the DSSD.Taking into account systematic error on the energy loss table selection and the error on the DSSD calibration we did not evaluate them larger than 1 μm. The statistical error can be evaluated looking at the sigma of the residual energy distribution in the DSSD, and show a 100 keV sigma, leading to an error of ± 0.4 μm. The final mapping of the detectors thickness is presented in Fig.4.15.

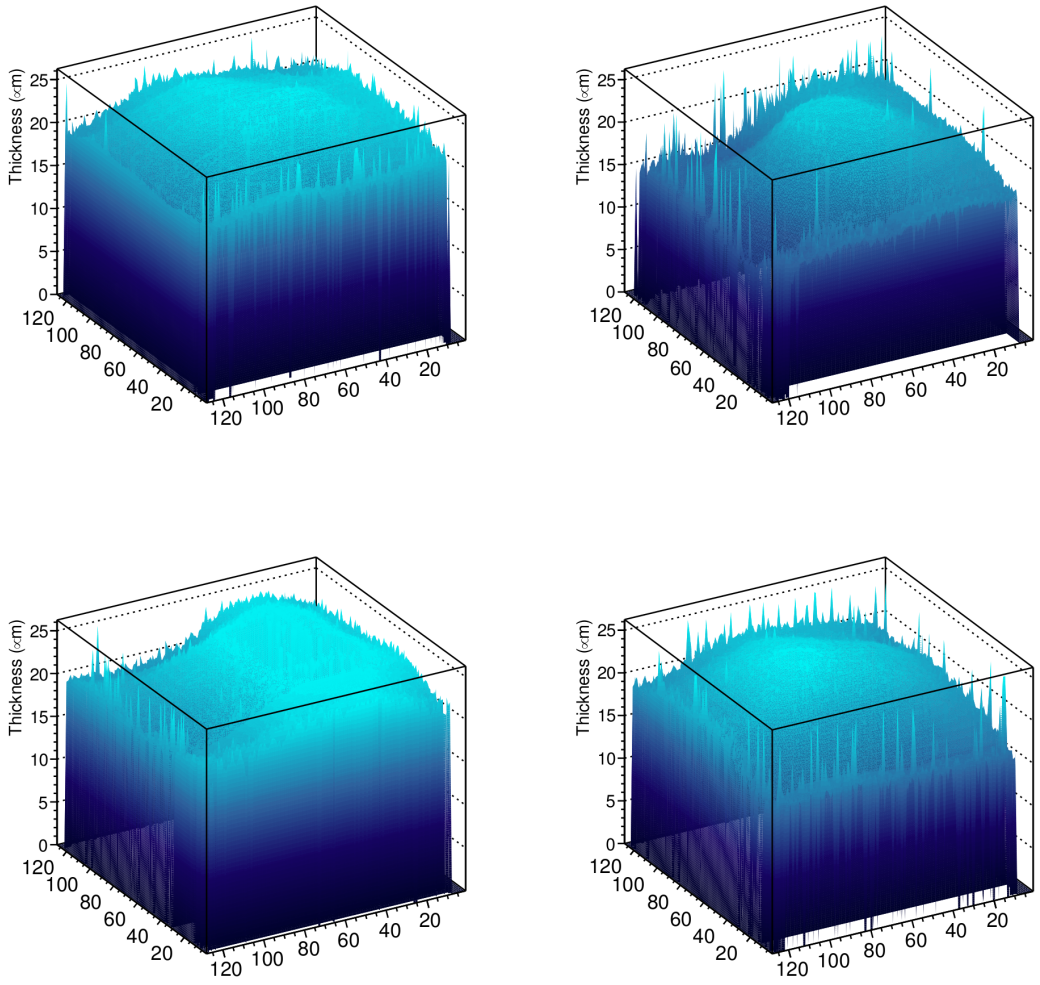

Figure 4.15: *Thickness mapping of the four 20 μm thick silicon detector. Detector 1 is in the top left corner, other following clockwise. The color code indicate the thickness, from dark blue (thin) to light blue (thick).*

The thickness measurement thus reveals severe inhomogeneities, especially in detector 2. The manufacturer's (Micron) specifications are not fulfilled. Thicknesses less than 15 μm thick as well as very irregular shapes are observed. We will see in

the next section how the thickness study allows to improve the identification plot and to obtain the final results.

Thickness correction

To take into account the correction measurement we used the Bethe-Block formula, offering a good description for energies above 1 MeV.

$$-\frac{dE}{dx} = \frac{4\pi n}{m_e}(\frac{e^2}{4\pi\epsilon_0})^2\frac{Z^2}{v^2}ln(\frac{2m_e}{I}v^2) \tag{4.7}$$

with:
$-dx$ = the thickness of material
m_e = the electron mass
Z = the particle atomic number (if fully ionize)
v = the particle velocity
I = the mean excitation potential of the material = 173.5 eV for Silicon [TB68]
Replacing v^2 by $\frac{2E}{A}$ with E, being the particle kinetic energy, and A its mass we obtain :

$$-\frac{dE}{dx} = \frac{2\pi n}{m_e}(\frac{e^2}{4\pi\epsilon_0})^2 AZ^2\frac{1}{E}ln(\frac{4m_e}{AI}E) \tag{4.8}$$

using the approximation where ΔE and x_{sssd} are the energy loss in the SSSD and the SSSD thickness respectively:

$$\frac{dE}{dx} \approx \frac{\Delta E}{\Delta x} = \frac{\Delta E}{x_{sssd}} \tag{4.9}$$

we obtain:

$$\Delta E \approx -x_{sssd}\frac{2\pi n}{m_e}(\frac{e^2}{4\pi\epsilon_0})^2 AZ^2\frac{1}{E}ln(\frac{4m_e}{AI}E) \tag{4.10}$$

For a given particle and a given material, the thickness of material factorizes in the expression of the energy loss as a function of the incident kinetic energy.We can therefore renormalize the energy loss in the SSSD to a given arbitrary thickness, we choose the nominal 20 μm thickness:

$$E_{corrected} = \frac{x_{sssd}E_{SSSD}}{x_{normalisation}} \tag{4.11}$$

The next section will show how this correction allows to separate correctly the charged particle using E-ΔE identification.

4.6 Particle Identification

For the purpose of particle identification, we used a multi-variable analysis using various cuts in various representations. We intend to separate ^{3}He of energy below 22 MeV using the combination of the three methods : TOF-ΔE, TOF-E and ΔE-E. We will present these methods in the following:

4.6.1 E-ΔE identification

The E-ΔE method is a powerful tool for particle identification. As shown in Eq.4.10 it allows to separate particles both in mass and charge. This method is effective for intermediate energy light particles, and we planned to use it to separate ^{3}He from ^{3}H and ^{4}He using the $\Delta E = E_{SSSD}$ and $E_{Total} = E_{SSSD} + E_{DSSD}$.

$$\Delta E \propto x_{SSSD} K \frac{A.Z^2}{E} ln(R\frac{E}{A}) \tag{4.12}$$

where A and Z are respectively the mass and charge of the particle, E its initial kinetic energy and K a constant. The important inhomogeneities of the SSSD detector strongly limits the particle separation as shown in Fig.4.16*(top)*. Using the renormalized $\Delta E = E_{corrected}$ of Eq.4.11, we can obtain a much better identification plot, as shown in Fig.4.16*(bottom)*. Before (top), the ^{3}He and ^{4}He could not be separated, after correction (bottom), the identification becomes effective in mass, revealing even the ^{6}He. In order to obtained a clearer plot the ^{9}Li beam punching through the DSSD has been removed an other method (see Sec.4.6.3). The hydrogen isotopes separation is also improved significantly.

The identification plots for the telescope 1, 3 and 4 are qualitatively similar. However the SSSD number 2 cracked during the mounting of the experiment. Though this detector shows a good resolution during the alpha calibration, we can see on Fig.4.17 that the identification plot is not as good as for the other detectors.

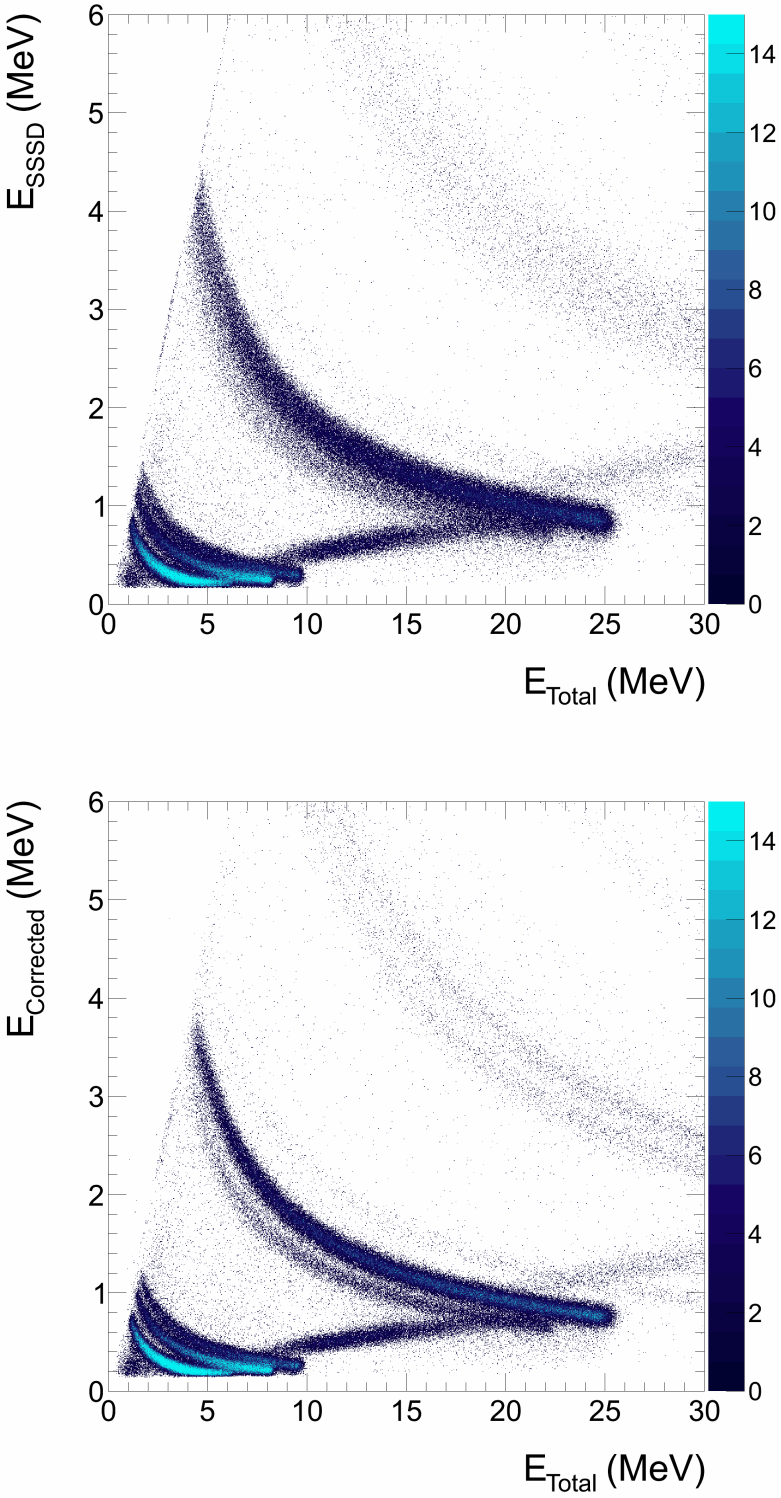

Figure 4.16: *E-ΔE spectra obtain before (top) and after (bottom) correction for telescope 1. The green line is a guide to the eyes, showing the separation become effective after the thickness correction.*

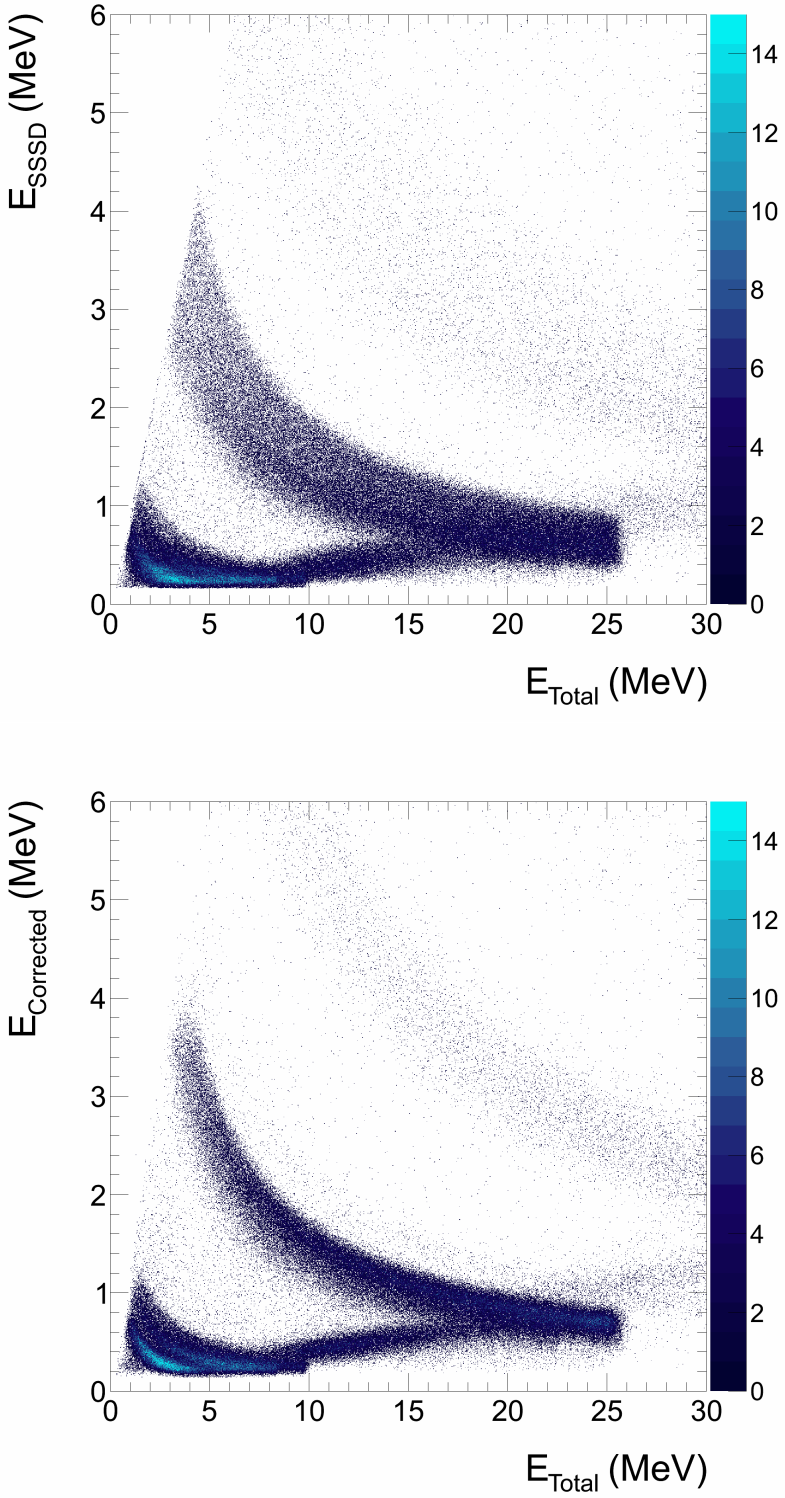

Figure 4.17: *E-ΔE spectra obtain before (left) and after (right) correction for telescope 2. The detector broke by itself before the experiment because of its small thickness (below 15 μm) and have poorer identification capabilities.*

4.6.2 E-TOF identification

Time of flight (TOF) identification separates particles by masses, relativistic kinematics giving:

$$t = d\sqrt{1 - \frac{m^2}{E^2}} \tag{4.13}$$

with:
t = time of flight, in this case the start signal is given by the MUST2 DSSD and the stop signal by the F2 plastic delayed.
d = distance to between the target and the detectors
E = particle kinetic energy
m = particle mass

Thus, this technique of identification can separate ^{3}He from ^{4}He but not from ^{3}H. However ^{3}He and ^{3}H are separated E-TOF in the present set-up because the SSSD are placed relatively far from the DSSD and the target. Indeed after crossing the SSSD, the ^{3}He and ^{3}H particle of the same initial energy have different velocities over a sizeable flight length because of their different energy loss in the SSSD.

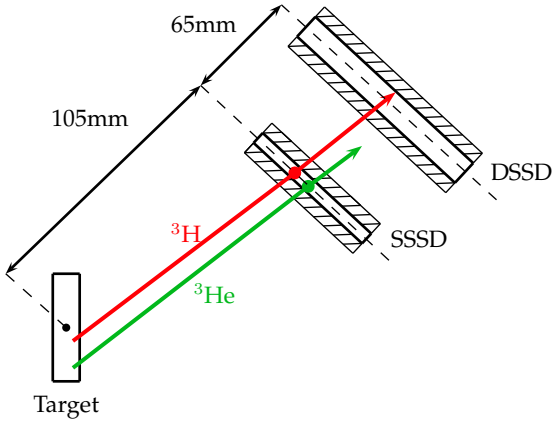

Figure 4.18: *The time of flight of same energy ^{3}He and ^{3}H is the same up to the SSSD, once they cross the last one, their energy is changed, and their time of flight is different on the remaining path.*

In the present experiment only the TOF provided by the DSSDs were available and not the one from the SSSD. From the TOF-E$_{DSSD}$ plot show in 4.19(top), separation between ^{3}H and ^{3}He is not achieved. Conversely, the TOF-E$_{SSSD+DSSD}$ allows to see a clear line of ^{3}He well separated from ^{3}H in all the energy range. However one can note that the separation of ^{3}He form ^{4}He is difficult above 15 MeV.

Because the time calibration is only relative, the regular E-TOF spectrum can be obtain by plotting E_{DSSD} vs TOF, as the E-TOF spectra between the SSSD and DSSD. On the contrary, the *modified* time of flight is obtained by plotting E_{Total} vs

TOF. The resulted modified time of flight shown side by side with the regular one in Fig.4.19 allow to see a clear line of ^{3}He well separated from ^{3}H in all the energy range. However one can note that the separation of ^{3}He form ^{4}He is difficult above 15 MeV.

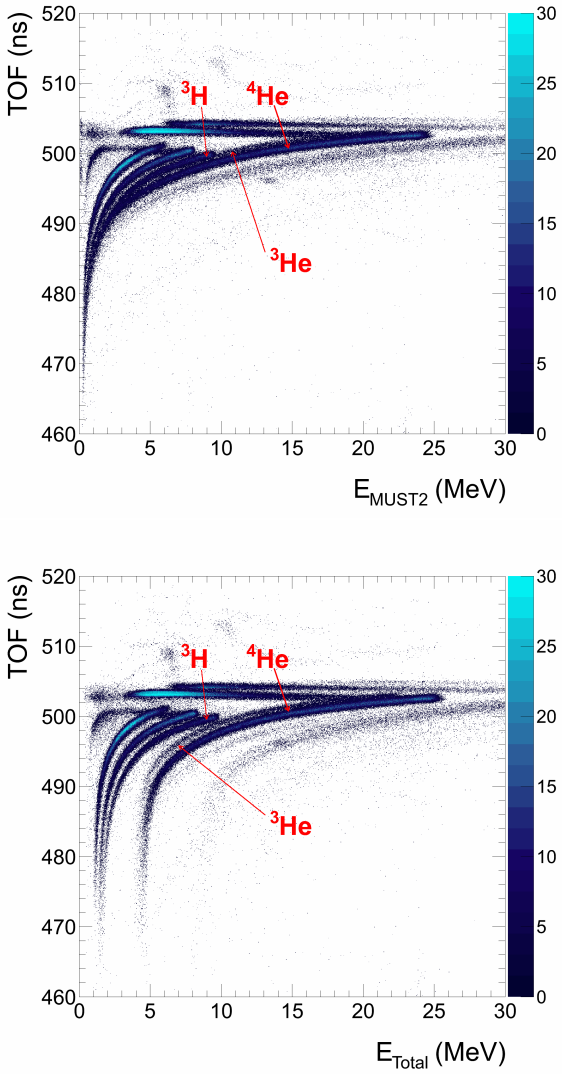

Figure 4.19: *Target-DSSD time of flight (TOF) vs Energy in the DSSD (top) and TOF vs $E_{SSSD+DSSD}$ (bottom). The ^{3}He are separated from ^{3}H and ^{4}He because of the different energy loss in the SSSD that modify their time of flight differently.*

4.6.3 ΔE-TOF identification

The combination of the energy measurement in the SSSD and the time of flight in MUST2 gives an excellent separation of the particle in Z, especially at high

energy. This identification is powerful to remove any contribution of the beam halo in the identification spectrum shown in Fig.4.20.

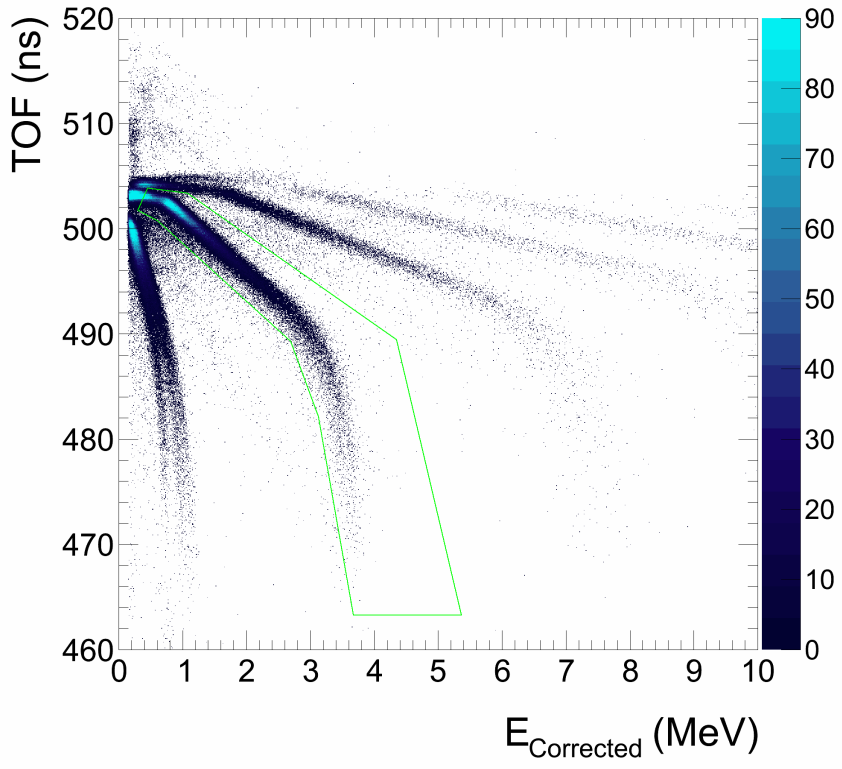

Figure 4.20: *ΔE-TOF spectra for telescope 1. The green line is surrounding the He isotopes.*

4.6.4 Multi-variables analysis

Using the different parameters shown above and setting gates in the three different representations successively:

1 Using ΔE-TOF representation Fig.4.20 we select only the He isotopes.

2 Using E-TOF representation Fig.4.21 we remove most of the ^{4}He particles.

3 Using ΔE-E representation Fig.4.22 we select accurately the ^{3}He.

we finally obtained a good identification of the ^{3}He of interest:

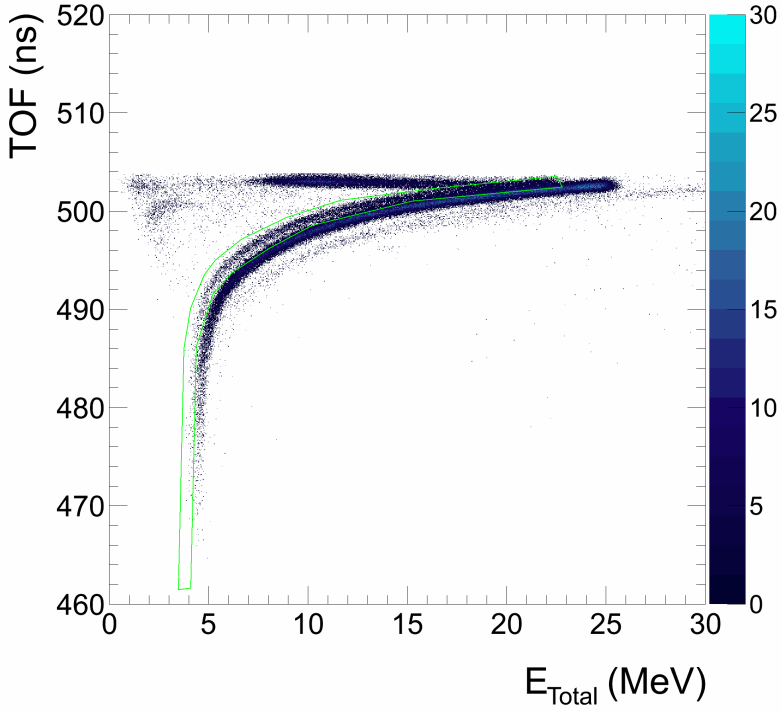

Figure 4.21: *E-TOF spectrum for telescope 1 conditioned by the He isotopes gate in the ΔE-TOF spectrum (see Fig.4.20) . The green line is selecting the ^{3}He particles.*

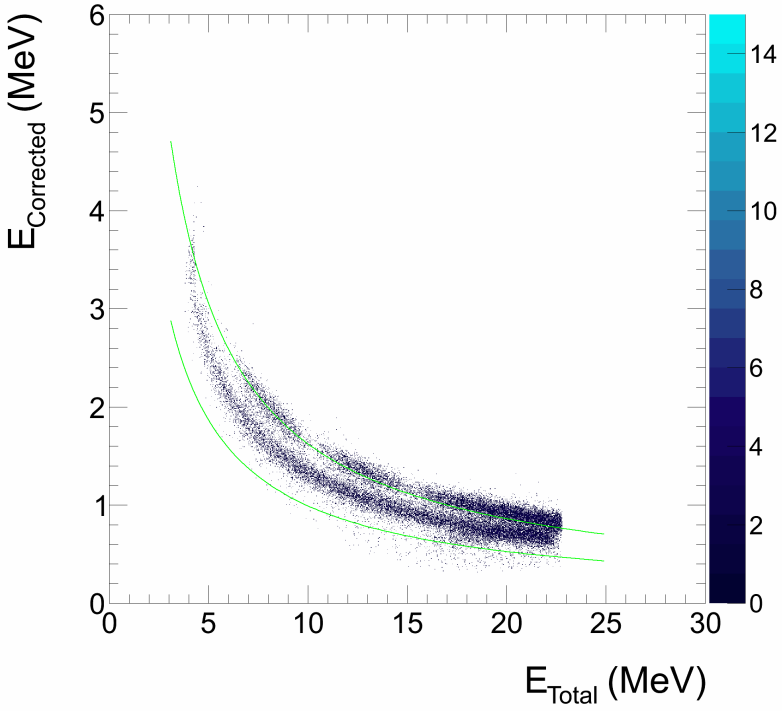

Figure 4.22: *E-ΔE spectrum for telescope 1 conditioned by the ΔE-TOF He isotopes gated (see Fig.4.20) and E-TOF ^{3}He gated (see Fig.4.21). The green lines are selecting the ^{3}He particles.*

4.6.5 Zero degrees telescope

An additional telescope, T6, was placed at zero degrees to detect heavy products of reactions using E-ΔE identification between the DSSD and the CsI stage. The telescope was protected from the beam by a two-stage plastic. The identification plot, summed over all the CsI modules of T6, is visible in Fig.4.23.

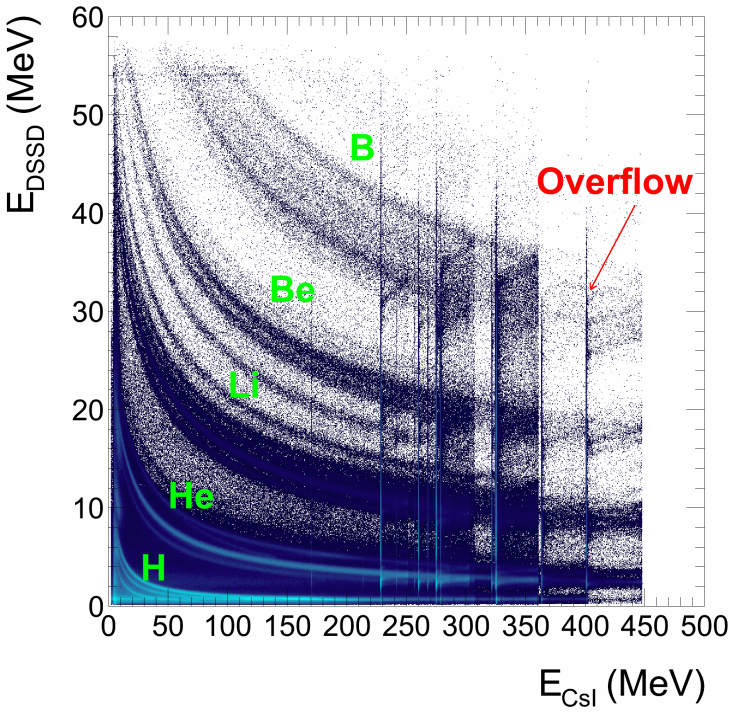

Figure 4.23: *E-ΔE identification, summed over all the CsI modules of T6, of particles around zero degrees. The different particles are identified while overflow lines are visible (one for each crystal).*

We observe the presence of strong overflow lines corresponding to energy deposit higher than the electronics range. There is one overflow line for each CsI module. Most of ^{8}He and ^{6}He of interest are located in this region where they can not be separated.

4.6.6 Zero degrees plastic detectors

The two plastic scintillators placed around zero degrees to protect the zero degrees MUST2 telescope aimed at allowing identification of the heavy residues of reaction, and especially at separating Helium isotopes, through $E - \Delta E$ method. However the quenching effect, which demises the light output produced by the particle energy loss in the scintillator, altered the EΔ-E plot, making the identification harder.

Using plastic F2 down-scaled events, and the identification information of the incoming beam particles (see Fig.4.1), we figured out the identification. The Bρ of the second dipole of RIPS defined the beam particles energies. ^{8}He are around 45 AMeV while ^{6}He are around 78 AMeV. This noticeable difference explains why the ^{6}He particles are in the punch through region in Fig.4.25 and the ^{8}He are stopped in the second stage plastic. This information, combined with the light particles identification allows to define a graphical cut in the EΔ-E plane which avoids background but does not cause loss of correct events.

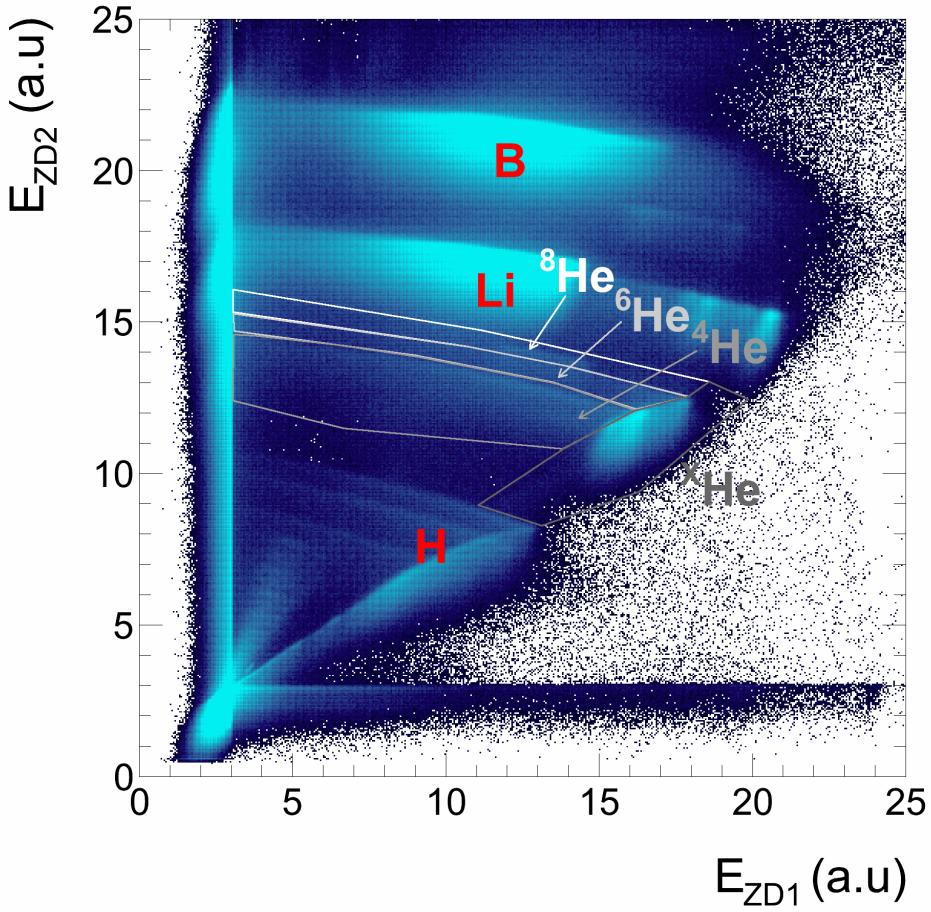

Figure 4.24: *E-ΔE identification around zero degrees of beam single events. He isotopes are identified by graphical cut. The regions marked ^{X}He correspond the punch through of Helium isotopes, where He isotopes are no longer separated.*

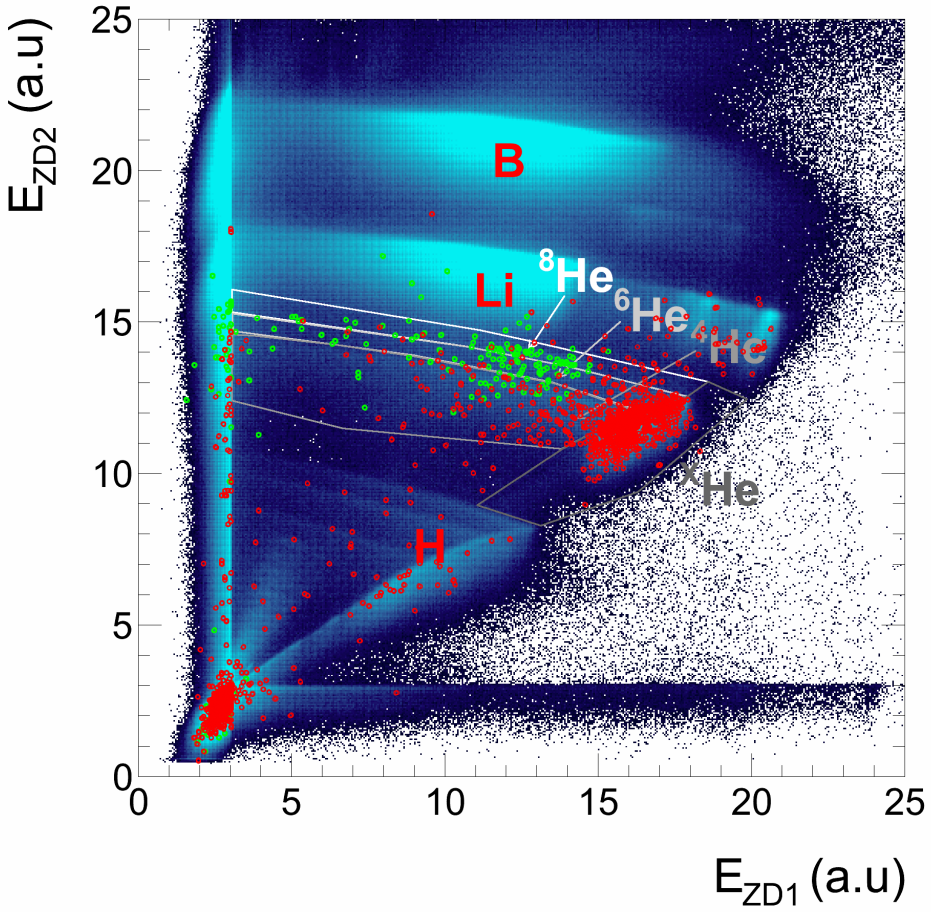

Figure 4.25: *The same identification plot (left) with additional identification. The green dots correspond to the* ^{8}*He beam particles (see Fig.4.1) and the red dots to the* ^{6}*He particles.*

4.7 Extracting the observables of interest

Transfer reactions investigated with the missing mass method represent a great tool for study of unbound nuclei. Because of the two body kinematics constraints the ejectile particle carries away information of the formed nuclei. Therefore, the combination of the energy and angle in the laboratory frame are sufficient to extract the relevant observables of the reaction. Let us consider the two body reaction:

$$A + a \rightarrow B + b \tag{4.14}$$

where A is the beam particle, a the target particle, B the studied nucleus and b the ejectile particle. We can define the energy-momentum quadrivector $\vec{P_i}$ for each of the particle in both the center of mass frame and the laboratory frame. Figure 4.26 defines the center of mass angle θ_{CM} and its associated laboratory angle θ_{Lab},

defined as the angle of the b particle with respect to the beam axis (see Fig.4.26).

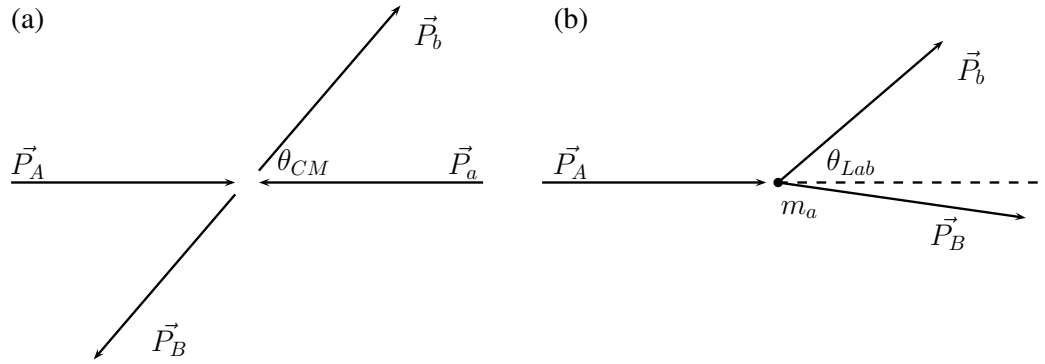

Figure 4.26: *The two body kinematics in the center of mass frame (a) and laboratory frame (b) where the target particle is at rest.*

Using the natural unit convention $c = 1$ and recalling the definition of the kinetic energy $T = E - m$ of the particle of energy E and mass m, one can write in the laboratory frame:

$$\begin{cases} \vec{P_A} = (T_A + m_A, 0, 0, \sqrt{T_A^2 + 2T_A m_A}) \\ \vec{P_a} = (m_a, 0, 0, 0) \\ \vec{P_b} = (T_b + m_b, \sqrt{T_b^2 + 2T_b m_b}\sin(\theta_{Lab}), 0, \sqrt{T_b^2 + 2T_b m_b}\cos(\theta_{Lab})) \\ \vec{P_B} = (T_B + m_B, p_{Bx}, 0, p_{By}) \end{cases} \tag{4.15}$$

The missing mass method relies on the measurement of T_b and θ_{Lab}, the other parameters T_A, m_A, m_b are supposed to be known. We will see in the next sections how to deduce m_B and θ_{CM} from these two information.

4.7.1 Excitation Energy

The excitation energy E^* of nuclei B is defined as follow:

$$E^* = m_B - m_{Bgs} \tag{4.16}$$

where m_{Bgs} is the mass of B in its ground state and m_B the mass of the formed nuclei B as used in Eq.4.15.

In the case of an unbound nuclei B, the reference energy of the system m_{Bgs} could be defined in different way. The 2003 Audi mass table, for instance, takes the first resonant state measured by Ostrowski *et al* [OBG+94] as reference. We choose the convention where it is taken as the lowest particle emission threshold value, *i.e.* for ^{10}He the ^{8}He+n+n decay threshold:

$$m_{^{10}He_{gs}} = m_{^{8}He_{gs}} + 2m_n \tag{4.17}$$

Applying the momentum conservation law:

$$\vec{P_A} + \vec{P_a} = \vec{P_b} + \vec{P_B} \tag{4.18}$$

we obtained:

$$\begin{cases} m_B = T_A + m_A + m_a - T_b - m_b + T_B \\ T_B = \sqrt{T_A + T_b - 2T_A T_b \cos(\theta_{Lab})} \end{cases} \tag{4.19}$$

With the measured T_b and θ_{Lab}, one can now compute the excitation energy of the studied nuclei. It is important to note that because T_b is the energy measured by the charged particle detectors. It is usually referred as E_{Lab}, we will use this convention in this document. In the same way, one can note that T_A refers to what is usually called the beam energy and noted E_{Beam}.

The reaction occurs inside a medium, the target, and therefore the particle b will lose part of its energy. In a similar way, the dead layers of the charged particles detectors contribute to the underestimate of E_{Lab} as shown in Fig.4.27. Using energy loss table, one can estimate the loss in the different layers crossed by the particle, leading to:

$$\begin{aligned} E_{Lab} &= E_{DSSD}^{measured} + E_{DSSD}^{front}(E, \theta_n) \\ &+ E_{SSSD}^{back}(E, \theta_n) + E_{SSSD}^{measured} + E_{SSSD}^{front}(E, \theta_n) \\ &+ E_{Target}(E, \theta_{Lab}) \end{aligned} \tag{4.20}$$

The red terms calculation relies directly on the evaluation of the dead layer for the SSSD and DSSD (see Sec.4.4.1 and Sec.4.5.1). Moreover, only the front dead layer has been measured, while the back one remains unknown. For that reason, we used instead the overall thickness measurement of the SSSD (see Sec.4.5.2) and did not use the measured energy inside the SSSD. This is represented by the blue line in Fig.4.27.

$$\begin{aligned} E_{Lab} &= E_{DSSD}^{measured} \\ &+ E_{SSSD}(E_{DSSD}^{measured}, e_{SSSD}, \theta_n) \\ &+ E_{Target}(E_{DSSD} + E_{SSSD}, e_{Target}, \theta_{Target}) \end{aligned} \tag{4.21}$$

In the case of particles going through the DSSD, the total energy is evaluated using the thickness e_{DSSD} of the silicon stage:

$$\begin{aligned} E_{Lab} &= E_{MUST2}(E_{DSSD}^{measured}, e_{DSSD}, \theta_n) \\ &+ E_{SSSD}(E_{MUST2}, e_{SSSD}, \theta_n) \\ &+ E_{Target}(E_{MUST2} + E_{SSSD}, e_{Target}, \theta_{Target}) \end{aligned} \tag{4.22}$$

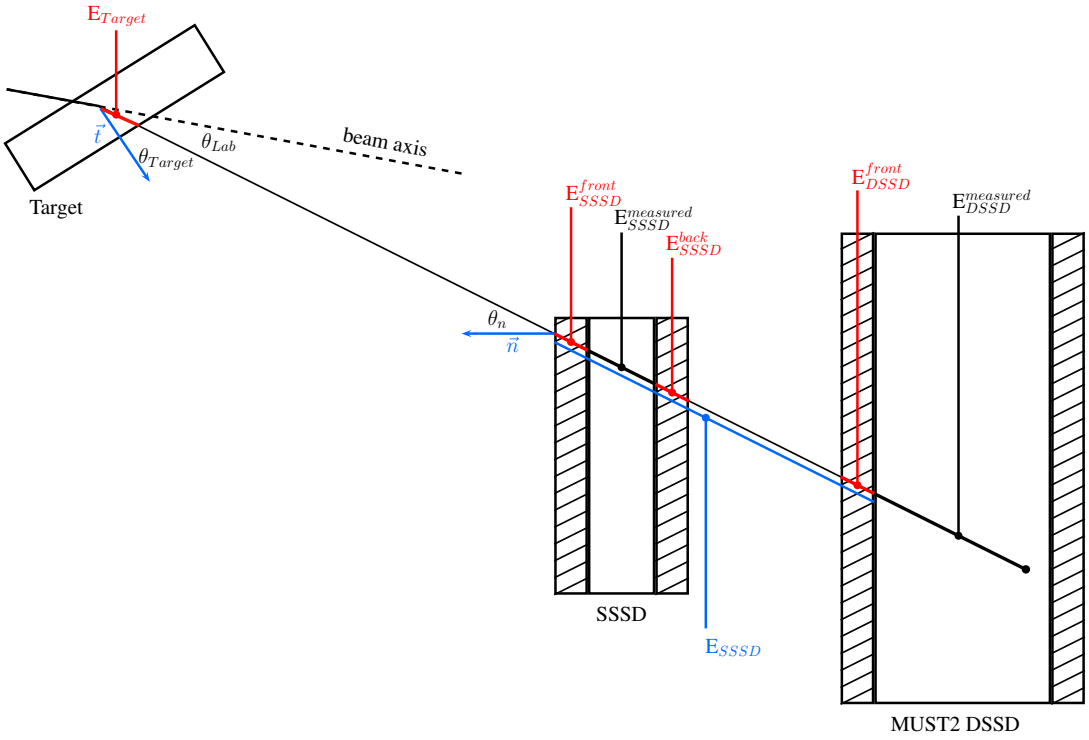

Figure 4.27: *Definition of parameters needed for the reconstruction of the excitation energy of a particle going through the detection system.* $\vec{t}$ *and* $\vec{n}$ *are respectively the normal to the target and the normal to the detector surface.*

As expressed in Eq.(4.21), the correction term depends on the energy of the particle while crossing the non sensitive material. E_{Lab} is reconstructed by starting at the end of the track, and adding the energy lost in each layer one by one. The beam incident angle is taken into account, as well as the incident angle of the detected particle with respect to the detection surfaces. However the exact position where the reaction occurs in the target is unknown. While the PPAC gives information for the x-y plane, no information on the z coordinate is available. One can assume that the reaction takes place in the middle of the target, averaging the path of the particle within the target, but the energy-loss in the target is not a linear function of the path length, and this produces a systematic error. A better method consists in taking, the average on the energy loss inside the target, using a random generator to uniformly cover the target thickness. This latter is adjusted to reproduce both

the ^{8}He and ^{9}Li ground states. Though the nominal thickness of the target was 1.5 mg/cm^2 (13.1 μm of CD2), the adjustment leads to a value of 1.9 mg/cm^2 (18 μm of CD2). This value is considered as acceptable with respect to the precision of the method used to produce the target and in agreement with other observed discrepancies [Gir11].

4.7.2 Angular Distribution

The center of mass angle θ_{CM} can be deduced from E_{Lab} and θ_{Lab} using the following relation:

$$\tan(\theta_{CM}) = \frac{\sqrt{E_{Lab}^2 + 2E_{Lab}m_b}\sin(\theta_{Lab})}{-\beta\gamma(E_{Lab} + m_b) + \gamma\sqrt{E_{Lab}^2 + 2E_{Lab}m_b}\cos(\theta_{Lab})} \tag{4.23}$$

where the velocity β and the Lorentz factor γ of the center of mass system are given by the relation:

$$\beta = \frac{\sqrt{E_{Beam}^2 + 2E_{Beam}m_A}}{E_{Beam} + m_A + m_a} \tag{4.24}$$

$$\gamma = \frac{1}{\sqrt{1-\beta^2}} \tag{4.25}$$

For each event, the center of mass angle θ_{CM} is computed. The E^* spectra is then gated to obtain the angular distribution $N(\theta_{CM})$ associated with each of the observed level. To be compared with the reaction model, we need to deduce from this $N(\theta_{CM})$, the differential cross section associated with the reaction:

$$\frac{d\sigma}{d\Omega_{CM}} = \frac{N(\theta_{CM})}{N_{Target}\cdot N_{Beam}\cdot \epsilon_{PPAC}\cdot \epsilon_{MUST2}\cdot \epsilon_{Coincidence}\cdot d\Omega_{CM}(\theta_{CM})} \tag{4.26}$$

with:

N_{Target} = Number of deuteron in the CD2 target

N_{Beam} = Number of incident beam particle on the target

ϵ_{PPAC} = efficiency of the PPAC reconstruction

ϵ_{MUST2} = efficiency of the MUST2 event algorithm = 0.9

$\epsilon_{Coincidence}$ = efficiency of the coincidence between the b and B particle

$d\Omega_{CM}$ = solid angle covered by the detection set-up at a given θ_{CM}

N_{Target} is accessible knowing the target thickness. The fraction of proton contained in the target has not been measured and is assumed to be negligible:

$$N_{Target} = \frac{2\cdot N_{Avogadro}t}{M_{carbon} + 2\cdot M_{deuteron}} \tag{4.27}$$

with:

$N_{Avagadro}$ = Avogadro constant

t = the target thickness (g/cm^2)

M = standard atomic weight of carbon, deuteron

The target thickness has been adjusted to reproduce correctly the position of ^{8}He and ^{9}Li ground state positions.

The number of incident particle N_{Beam} on the target is evaluated at the same time as the efficiency of reconstruction. For this purpose, events triggered by the plastic F2 divided, by a factor D, has been used, counting events with a PPAC reconstruction on target and selecting the beam particle ^{11}Li or ^{9}Li we obtain $N_{Trigger}$.

$$N_{Beam} \cdot \epsilon_{PPAC} = D \cdot N_{Trigger} \tag{4.28}$$

Finally the product $\epsilon_{Coincidence} \cdot d\Omega_{CM}$ is evaluated at once using the simulation and a flat differential cross section in the center of mass. The statistical error on the cross section is given by the statistical error on the number of counts for each point of $N(\theta_{CM})$ is equal to $\sqrt{N(\theta_{CM})}$ but also the statistical error of the simulation, based on a *Monte Carlo* approach (see Sec.3.3).

4.8 Conclusion

The severe inhomogeneities of the thin silicon detectors was corrected successfully. The ^{3}He particles of interest coming from the (d,^{3}He) reaction are correctly identified to exclude ^{4}He and ^{3}H contamination. In the same way, heavy residues of reaction could be isolated within the zero degrees detections. The reconstruction of the beam trajectory and the granularity of the MUST2 DSSD allow angular measurement. This information are used to extract the relevant observables that are presented in the next chapter.

Chapter 5

Results

This chapter will present the obtained results for the studied reaction ^{9}Li(d,d) and ^{11}Li(d,d) in a first part and then ^{9}L(d,^{3}He) and ^{11}Li(d,^{3}He) results. The use of reaction model is mandatory in order to extract the nuclear structure information on the nuclei of interest. For the analysis of the transfer reactions, we will use the standard one-step Distorted Wave Born Approximation (DWBA) model.

5.1 DWBA

The DWBA is a reaction model used to analyze the experimental differential cross-sections of direct reaction such as elastic and inelastic scattering, as well as transfer reactions. Let us consider the following reactions:

$$A + a \rightarrow b + B \tag{5.1}$$

where A is the target, a and b are respectively the projectile and ejectile, B the studied nucleus, populated in its ground state or in excited states. We note α the in-going channel $(A + a)$ and β the out-going channel $(b + B)$. We can write the differential reaction cross-section as [Mes60]:

$$\frac{d\sigma}{d\Omega} = \frac{\mu_\alpha \mu_\beta}{(2\pi\hbar^2)^2} \frac{k_\beta}{k_\alpha} \frac{1}{(2J_a + 1)(2J_A + 1)} \sum_{M_\alpha M_\beta} |T_{\alpha\beta}|^2 \tag{5.2}$$

where μ_α and μ_β are the reduced masses of the in-going and out-going channels,
k_α and k_β are the wave number of in-going and out-going channel,
J_a and J_A the spin of the in-going nuclei,
$T_{\alpha\beta}$ is the transition amplitude associated with the reaction, depending of the spin projections of the particles M_α and M_β.

We can write the Hamiltonian H for both α and β channels:

$$H = H_\alpha + T_\alpha + V_\alpha = H_\beta + T_\beta + V_\beta \tag{5.3}$$

with $H_{\alpha,\beta}$ describing the intrinsic state of the nuclei in channels α and β, $T_{\alpha,\beta}$ the kinetic energy operator and $V_{\alpha,\beta}$ the interaction between the nuclei of the channel.

We consider the plane wave solutions $\phi_{\alpha,\beta}$ of the Schrödinger equation for the free propagation and $\chi_{\alpha,\beta}$ solutions of the elastic scattering on the potential $U_{\alpha,\beta}$:

$$H\phi_{\alpha,\beta} = (H_{\alpha,\beta} + T_{\alpha,\beta})\phi_{\alpha,\beta} = E\phi_{\alpha,\beta} \tag{5.4}$$

$$H\chi_{\alpha,\beta} = (H_{\alpha,\beta} + T_{\alpha,\beta} + U_{\alpha,\beta})\chi_{\alpha,\beta} = E\chi_{\alpha,\beta} \tag{5.5}$$

We now project the total wave function of the system $\Psi_\alpha^{(+)}$ and $\Psi_\beta^{(-)}$ on the new base [1]:

$$T_{\alpha\beta} = \langle \chi_\beta^{(-)}\phi_\beta | V_\beta - U_\beta | \Psi_\alpha^{(+)} \rangle = \langle \Psi_\beta^{(-)} | V_\alpha - U_\alpha | \chi_\alpha^{(+)}\phi_\alpha \rangle \tag{5.6}$$

The left part of the second equation is called the *prior* form and the right part the *post* form.

5.1.1 The Born Approximation

Let us consider $G_\alpha^{(+)}$ the green function associated to the H operator. We can develop $\Psi_\alpha^{(+)}$ in a Born series :

$$|\Psi_\alpha\rangle = [1 + G_\alpha^{(+)}(V_\alpha - U_\alpha) + G_\alpha^{(+)}(V_\alpha - U_\alpha)G_\alpha^{(+)}(V_\alpha - U_\alpha) + ...]\chi_\alpha^{(+)}|\phi_\alpha\rangle \tag{5.7}$$

The Born Approximation states that the elastic scattering governed by U_α is dominant, and therefore we can neglect terms containing $(V_\alpha - U_\alpha)^{n\geq 1}$. We then can write the transition amplitude (Eq.5.6)as:

$$T_{\alpha\beta} = \langle \chi_\beta^{(-)}\phi_\beta | (V_\beta - U_\beta) | \chi_\alpha^{(+)}\phi_\alpha \rangle \tag{5.8}$$

5.1.2 Transition potential

$(V_\beta - U_\beta)$ now governs the transition amplitude.In the case of the (d,^{3}He) reaction, the nucleus a is a deuterium, noted d and b an ^{3}He. The V_β potential could be separated in different contribution. First the interaction between the transferred proton and the deuterium V_{pd} and secondly the sum of the interaction between the transferred proton and all the nucleons in A, noted V_{pi} :

$$V_\beta = V_{pd} + \sum_{i=1}^{A} V_{pi} \equiv V_{pd} + V_{pA} \tag{5.9}$$

V_{pA} correspond to the interaction of the transferred proton with all the nucleons of A, *i.e.* the interaction of p with A. In the previous sub-section we assumed that the elastic scattering is the dominant process, that leads to consider $V_\beta \approx V_{pA}$. If we neglect the remnant term $V_{pA} - U_\beta$ The transition amplitude is reduced to:

$$T_{\alpha\beta} = \langle \chi_\beta^{(-)}\phi_\beta | V_{pd} | \chi_\alpha^{(+)}\phi_\alpha \rangle \tag{5.10}$$

[1] (+) and (-) denote in-coming and out-going boundaries conditions

Developing the integral we obtain(now $b = {}^3He$ and $a = d$):

$$T_{\alpha\beta} = \int \chi^*_\beta(\vec{r_{Bb}}, \vec{k_b})\langle\phi_{^3He}\phi_B|V_{pd}|\phi_d\phi_A\rangle\chi_\alpha(\vec{r_{Aa}}, \vec{k_a})d\vec{r}_{Aa}d\vec{r}_{Bb} \tag{5.11}$$

Assuming that V_{pd} is only function of the $p-d$ distance we obtain :

$$T_{\alpha\beta} = \int \chi^*_\beta(\vec{r_{Bb}}, \vec{k_b})\langle\phi_B|\phi_A\rangle \cdot \langle\phi_{^3He}|V_{pd}|\phi_d\rangle\chi_\alpha(\vec{r_{Aa}}, \vec{k_a})d\vec{r}_{Aa}d\vec{r}_{Bb} \tag{5.12}$$

$\langle\phi_{^3He}|V_{pd}|\phi_d\rangle$ is sometimes referred as the range function. It is known with high accuracy for light particles (p,d,^{3}He,α,...). The important overlap function $\langle\phi_B|\phi_A\rangle$ that carries the nuclear structure information now appears explicitly in the transition amplitude. We will see below how it can be evaluated.

5.1.3 Zero Range approximation

The zero range approximation assumes the transfer occurred only when the transferred particle, here the proton, and a are at the same positions, *i.e* $\langle\phi_{^3He}|V_{pd}|\phi_d\rangle = D_0\delta(\vec{r}_{^3He-d})$. The approximation diminishes the complexity of the integral, reducing the number of variables to integrate. The approximation is valid if the wave length of a in the center of mass is large compared to the typical variation length of the wave function of A [Gle04]. In our case the incoming deuterons have an energy of 100 MeV in the center of mass, corresponding to a wave length of $\sim$2 fm, while the typical variation length of the nuclear wave functions is $\sim$1 fm.

5.1.4 Form factor

In order to calculate the nuclear overlap function of nuclei A and B, let us develop ϕ_B on a basis of eigenstates ϕ:

$$\phi_B = \sum_{lj} \beta_{lj}\langle J_A M_A jm|J_B M_B\rangle\Psi^{M_A}_{J_A}(\vec{\zeta_A})\phi_{lj}(\vec{r}_{Ap}) \tag{5.13}$$

where $\Psi^{M_A}_{J_A}(\vec{\zeta_A})$ is the initial wave functions of A within the inert core approximation. $\phi_{lj}(\vec{r}_{Ap})$ is the wave functions of the transferred proton. After integration of $\langle\phi_B|\phi_A\rangle$ over the intrinsic coordinated ζ_A, one obtains:

$$\langle\phi_B|\phi_A\rangle = C\sum_{lj} \beta_{lj}\langle J_A M_A jm|J_B M_B\rangle\phi^{m*}_{jl}(\vec{r}_{Ap}) \tag{5.14}$$

The radial part $u_{lj}(\vec{r}_{Ap})$ of the one-body function ϕ^m_{lj} is called the form-factor. As recalled in chap.1, the spectroscopic factor is defined as the norm of the radial overlap [Sat83]:

$$S_{lj} = \int |u_{lj}(r)|^2 r^2 dr \tag{5.15}$$

In order to determine the form factor to be used in the calculation of the DWBA amplitude, a standard way consists in writing:

$$u_{lj}(r) \approx S_{lj}^{1/2} \cdot \frac{\phi_{nlj}(r)}{r} \tag{5.16}$$

where $\phi_{nlj}(r)$ is the radial part of the wave function, normalized to 1, of a bound-state from an independent particle model. $\phi_{nlj}(r)$ is solution of the radial Schrödinger equation:

$$\left[\frac{d}{dr^2} - \frac{l(l+1)}{r^2} - \frac{2\mu}{\hbar^2}(V(r) - E)\right] \frac{\mu_{nlj}(r)}{r} = 0 \tag{5.17}$$

V(r) is usually taken as a Wood-Saxon potential whose depth V_0 is adjusted so as to reproduce the binding energy of the transferred particle. We note that other parameters of the Wood-Saxon potential, radius and diffusseness, are usually fixed to "standard" values $r_0 = 1.25$ fm and $a_0 = 0.65$ fm, inducing some uncertainties in the calculations. It is known that changing the value of r_0 induces variation of the calculated cross-section. The above procedure is implemented in DWBA code such as DWUK4[Kun02] to calculate the form factor internally. Another option is the use of externally calculated form factors from more sophisticated model.

The inhomogeneous equation provided such calculation for a large range of nuclei, providing a phenomenological input. The *ab initio* methods give a realistic and microscopic overlaps and allow a direct comparison with the experimental cross-section. These microscopic overlaps are not yet available for the studied nuclei but the perspective to perform such comparison in the near future is a thrilling motivation.

Experimentally, the spectroscopic factor is extracted by comparison between the DWBA and the experimental cross-section. Denoting the Clebsh-Gordan coefficient for isospin coupling C, we can define the spectroscopic factor S as:

$$C^2S = \left(\frac{d\sigma}{d\Omega}_{DWBA}\right)^{-1} \cdot \left(\frac{d\sigma}{d\Omega}_{Exp}\right) \tag{5.18}$$

In the case of single particle state population, S could be understood as a probability of occupancy of the single state considered. In a more general case, it could be linked to the likeliness of the initial and final state nuclei A and B, *i.e.* the $\langle A|B\rangle$ overlap.

5.1.5 Optical potential

The DWBA calculation relies on the generation of distorted wave functions χ, describing correctly the elastic scattering. To obtain these wave functions, we need a potential well to deforme the initial plane waves. This mean potential $U(r)$, describing the potential seen by a in the field of A, includes imaginary terms describing the flux lost in the other reaction channels. The potential is obtained using

global formulae in which the parameters are adjusted so as to reproduce a large variety of elastic scatterings on stable and nearly stable nuclei. Because of the density distribution in nuclei, the potential terms are derived from a Wood-Saxon shape characterized by r_i, the radius of the potential and a_i, its diffuseness:

$$f(r, r_i, a_i) = \left[1 + \exp(\frac{r - r_i A^{1/3}}{a_i})\right]^{-1} \tag{5.19}$$

Adding the Coulomb potential $V_C(r, r_C)$ we obtain the following description of the potential $U(r)$:

$$\begin{aligned} U(r) &= V_C(r, r_C) \\ &- V f(r, r_V, a_V) \\ &- iW f(r, r_W, a_W) \\ &+ i4W_D \frac{d}{dr} f(r, r_D, a_D) \\ &- \vec{\sigma}.\vec{l} V_{so} \left(\frac{\hbar}{M_\pi c}\right)^2 \frac{1}{r} \frac{d}{dr} f(r, r_{so}, a_{so}) \end{aligned} \tag{5.20}$$

There is only one proper potential for deuterium in the incoming channel in our incident energy domain, by Daehnick *et al* [DCV80] (here after referred as DAE) covering (d,d) reactions from 12 MeV to 90 MeV. We use the relativistic prescription denoted as F in [DCV80]. The DAE potential was obtained from data on 27 $\leq$ A $\leq$ 238 nuclei, far from the our region of interest. No optical potential parameters exist for light exotic nuclei.

The best potential available for (^{3}He,^{3}He) in our case was published by Becchetti and Greenlees [BH71] (B&G hereafter) and obtained for nuclei of mass A > 40 and E < 40 MeV. It will be employed to describe the interaction of the outgoing ^{3}He with the resonant ^{10}He or the bound ^{8}He.

The following section will present the differential cross-sections obtained from our experiment and compared to DWBA calculation. These calculations have been performed using the zero-range code DWUCK4 [Kun02].

5.2 Results for elastic and inelastic scattering

The additional telescope in the 90°-50° region, T7, allowed to detect ^{2}H coming from (d,d) and (d,d') reactions. The study of elastic scattering is an important tool to probe the validity of the optical potential used in the interpretation of transfer reactions.

Two beams have been used in this study, ^{9}Li and ^{11}Li, both around 50 AMeV. The results presented here were obtained using a target. To obtain kinematical plots associated with the reactions, we performed the following selections:

- Incident beam ^{9}Li/^{11}Li on target from beam identification plot (see Sect.4.2)

- **E-TOF** for low energy ^{2}H in T7

- **E-ΔE** for high energy ^{2}H in T7

- ^{9}**Li**/^{11}**Li** in the zero degrees plastic telescope

- ^{9}**Li**/^{11}**Li** in T6 MUST2 telescope placed at zero degrees

5.2.1 Energy Spectra

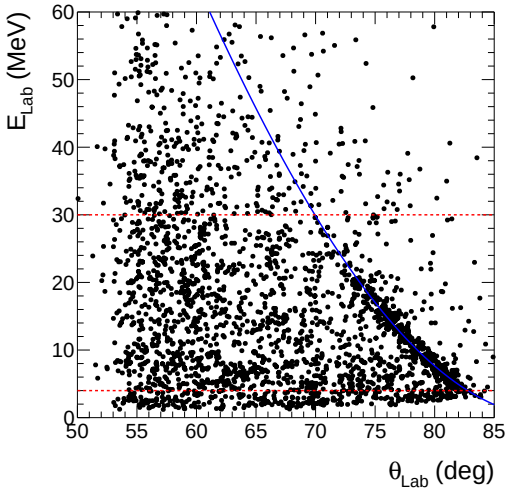

Figure 5.1: *Kinematic line from ^{9}Li(d,d) data. The theoretical kinematic line for the ground state in superimposed (blue) while the energy threshold (red) used to obtain the energy spectra are represented.*

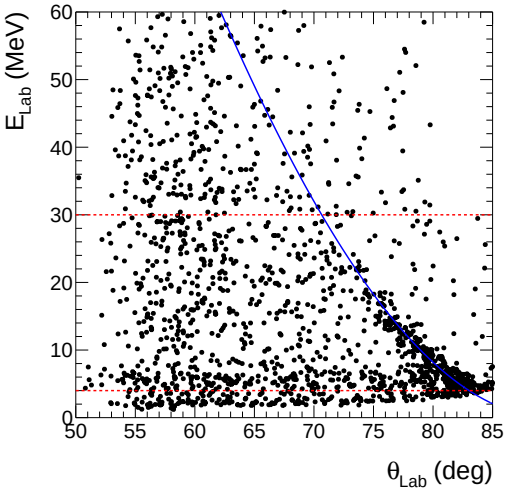

Figure 5.2: *Kinematic line from ^{11}Li(d,d) data. The theoretical kinematic line for the ground state in superimposed (blue) while the energy threshold (red) used to obtain the energy spectra are represented.*

The kinematical plots obtained for ^{9}Li and ^{11}Li are presented respectively in Fig.5.1 and Fig.5.2. Superimposed to the experimental data are the theoretical kinematical lines for elastic scattering at the experimental beam energy. We can observe a clear accumulation of statistics around the calculated lines. A strong background is visible at low energies, where the TOF identification of the ^{2}H is no longer effective to separate them from ^{1}H and ^{3}H. Above 30 MeV of deuteron energy, no events corresponding to elastic scattering emerge from the background. In order to reduce the background we selected the region between the red dashes.

Figure 5.3 and Fig.5.4 show the excitation energy spectra corresponding to ^{9}Li and ^{11}Li respectively. On both spectra the elastic peak has been fitted using Gaussian shaped functions deduced from the simulations (see Sect.3.3.1). Only the magnitude and position were left as free parameters. The experimental widths are very well reproduced by the simulations. The obtained value for ^{11}Li(d,d), $\sigma = 940$ keV, is larger than for ^{9}Li(d,d), $\sigma = 560$ keV. The difference is explained by the

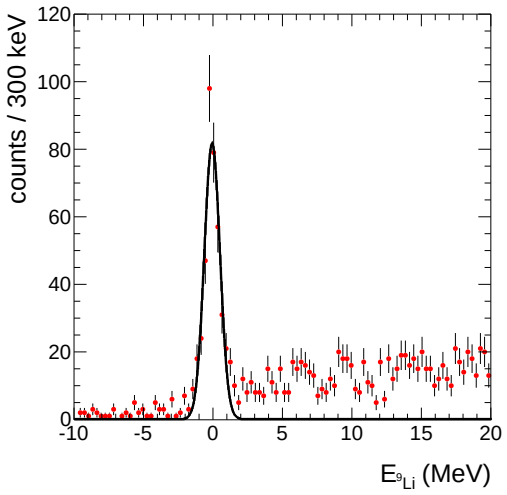

Figure 5.3: *Energy spectrum from ^{9}Li(d,d) data. The black line is a fit of fixed 560 keV width that gives E_{gs}= -46±32 keV.*

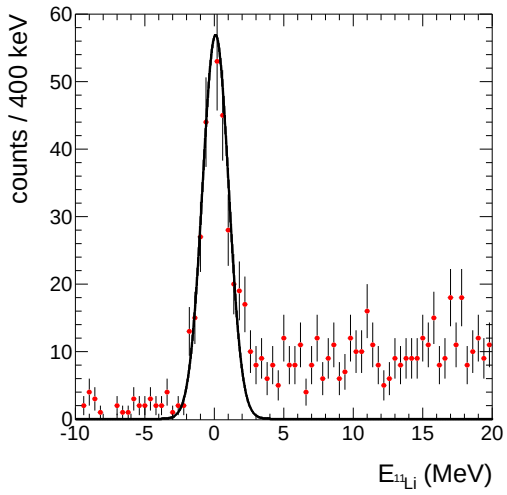

Figure 5.4: *Energy spectrum from ^{11}Li(d,d) data. The black line is a fit of fixed 940 keV width that gives E_{gs}= 25±72 keV.*

larger beam momentum spread in the case of ^{11}Li, while for ^{9}Li narrower momentum slits could be used. The ^{9}Li ground state is found at -46±32keV, within two σ of the expected position. The ^{11}Li has a ground state at 25±72 keV, again in agreement with the expected position. The excellent agreement of the ground-state positions is an indication of the correctness of the adjusted target thickness, 1.9 mg/cm^2.

The coincidence with the heavy particle around zero degrees play an important role, that is illustrated in Fig.5.5, showing the inclusive spectrum of the ^{9}Li(d,d). The important background has been estimated using the algorithm detailed in [MKM$^+$97] and implemented within the ROOT CERN library used for the analysis.

For the (d,^{3}He) transfer reaction spectra presented in the following, where the cross-section is much smaller, the detections in coincidence with the heavy residue is absolutely crucial.

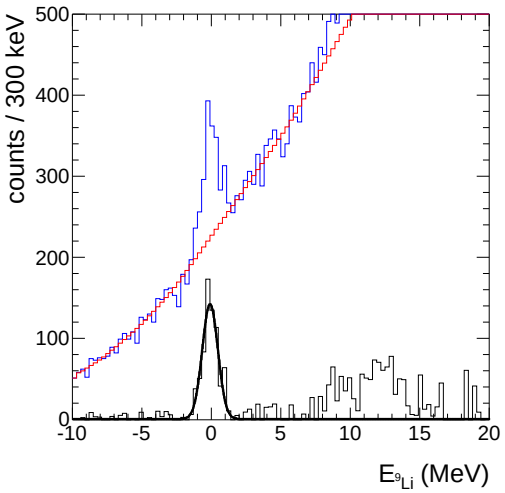

Figure 5.5: *Inclusive energy spectrum from $^{9}Li(d,d)$ data (blue histogram), the estimated background (red histogram). The subtraction (black histogram) of the signal and background is fitted (black curves) and gives a ground state position at E_{gs}= -81±22 keV.*

5.2.2 Differential cross-section

The angular distributions are obtained using a $-2 \leq E_{^{9,11}Li} \leq 2$ MeV gate on the spectra shown in Fig.5.3 and Fig.5.4. All the gate used to obtain the angular distribution were reported in the simulations and used to determine the solid angle covered by the detection set-up. Once normalized the angular distributions give the experimental differential cross-sections of the elastic scattering presented in Fig.5.6 and Fig.5.7.

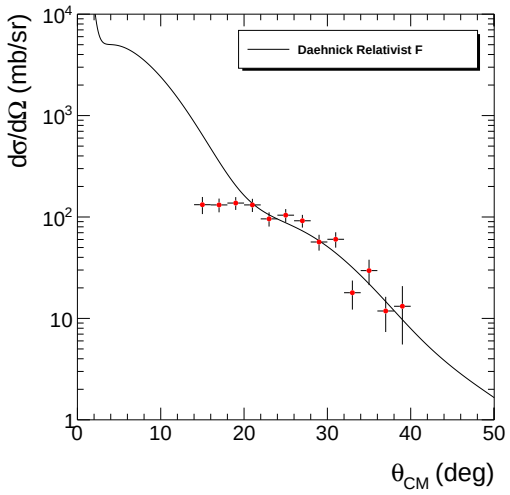

Figure 5.6: *The $^{9}Li(d,d)$ elastic cross-section after correction of the efficiency and normalization (red dot), compared with calculation using the Daehnick F optical potential.*

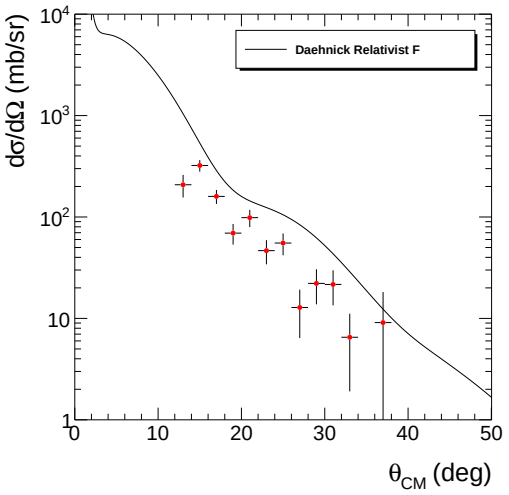

Figure 5.7: *The $^{11}Li(d,d)$ elastic cross-section after correction of the efficiency and normalization (red dot), compared with calculation using the Daehnick F optical potential.*

Comparison of the experimental differential cross-sections of Fig.5.6 and Fig.5.7 with the DAE potential highlights a good agreement, though this global potential was deduced from data on stable nuclei ranging from A=27-208, with energies from 12-90 MeV. For ^{11}Li, Fig.5.7 shows sizable difference in the amplitude of the cross-section. This loss of flux in the elastic scattering channel is qualitatively interpreted as a result of the low binding energy of the neutrons in ^{11}Li, favoring break-up. The DAE potential was fitted on stable nuclei, therefore, the imaginary part of the potential, taking into account the loss of flux in favor of other reaction channels is underestimated for such an extreme case of a halo nucleus.

5.3 Results for the one-proton transfer reaction (d,^{3}He)

5.3.1 Excitation Energy

The (d,^{3}He) data are obtained using the wall of four telescopes T1-4 located at forward angles, in conjunction with four SSSD for the identification of light particles. The first beam, ^{9}Li, was used to produce the bound ^{8}He. The target thickness was slightly modified to reproduce the position of its ground state. The second beam of ^{11}Li was used to produce the unbound ^{10}He. In both cases the spectra were obtained using the following gates:

- **Incident beam** ^{9}Li/^{11}Li on target

- **ΔE-TOF** in T1-4

- **E-TOF** in T1-4

- **E-ΔE** in T1-4

- **^{8}He** in the zero degrees plastic (cf Fig. 5.8 and 5.9)

- **^{8}He** in T6

The kinematical plots associated with the reactions are presented in Fig.5.10 for ^{9}Li(d,^{3}He)^{8}He and Fig.5.11 for ^{11}Li(d,^{3}He)^{10}He. The ^{8}He case shows very little background, because of a very narrow beam energy spread and the strong kinematical constraints on ^{8}He at forward angles, allowing a very narrow gate in the zero degrees plastic telescope, as shown in Fig 5.8. On the other hand the ^{10}He case shows an important background all over the energy range. This is a consequence of the broadening of the energy range of the heavy residues due to the decay of ^{10}He leading to more scattered events in the identification plot of the zero degrees plastic telescope as shown in Fig 5.9. A lower cross-section than for the ^{9}Li reaction, also plays a role as we will see in the following. However a significant increase of the statistics around the theoretical kinematical line is observed in both cases.

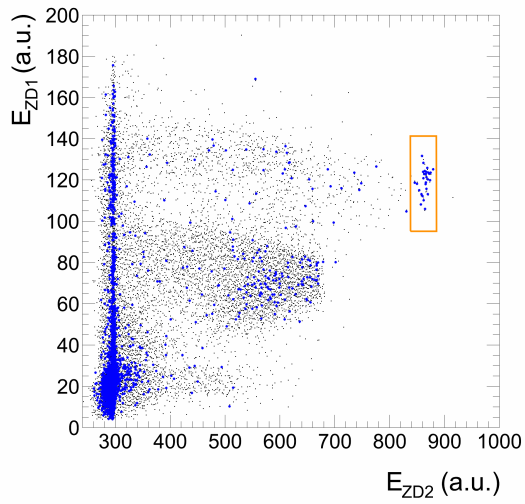

Figure 5.8: *ΔE-E identification plots in the zero degree plastic by. The orange cut selects the kinematically constraints ^{8}He coming from the $^{9}Li(d,^{3}He)$. The black dot are event in coincidence with ^{3}He, the blue dot are event in coincidence with ^{3}He and presenting an excitation energy between -2 MeV and 2 MeV.*

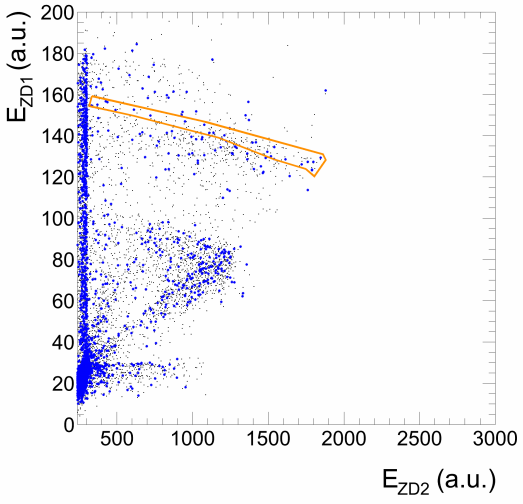

Figure 5.9: *ΔE-E identification plots in the zero degree plastic by. The orange cut selects the non kinematically constraints ^{8}He coming from the $^{11}Li(d,^{3}He)^{10}He$. The black dot are event in coincidence with ^{3}He, the blue dot are event in coincidence with ^{3}He and presenting an excitation energy between -2 MeV and 4 MeV.*

The associated energy spectra are presented in Fig.5.13 for ^{8}He. The presented fit gives a position of 2.7±196 keV, giving a good agreement with the expected position of the ground state. The absence of background and the compatibility of the width and the position of the signal with the simulations, confer confidence in the analysis.

The position of the first resonant state was left as free parameter. Fig.5.14 shows the obtained spectrum and the fit of the data, giving a first resonant state E_R= 1.4±0.3 MeV above the ^{8}He+n+n threshold taken as reference. No evidence for a narrow resonance just above the threshold as predicted by Aoyama [Aoy03] is found, in agreement with previous experimental studies.

Resonances are presenting a specific shape due to their short live time. G. Breit and E. Wigner showed how a resonance can be described using distribution, nowadays called Breit-Wigner, and which density of probability $f(E)$ is given by:

$$f(E) = \frac{1}{\pi} \cdot \frac{\Gamma/2}{(E_R - E)^2 + (\Gamma/2)^2} \tag{5.21}$$

where Γ is the width of the resonance and E_R its position. The experimental resolution broadens the resonance shape. The resulting signal can be modeled by the convolution of the Breit-Wigner and a Gaussian function, an example of such convolution is shown in Fig.5.12.

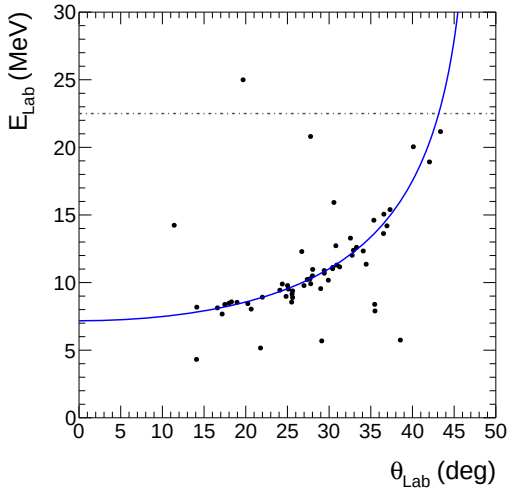

Figure 5.10: *Kinematical plot from the ^{9}Li(d,^{3}He) data, the blue line is the theoretical line of the ground state of ^{8}He.*

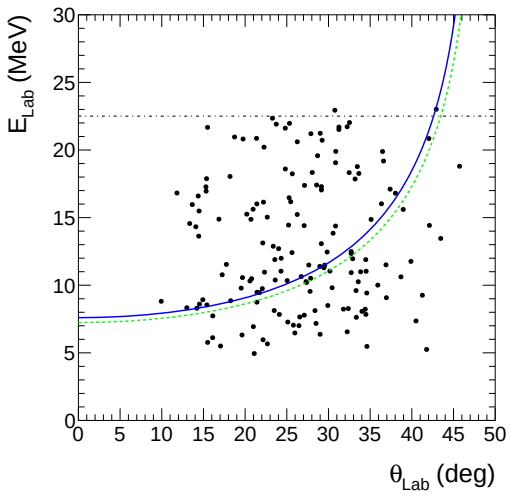

Figure 5.11: *Kinematical plot from the ^{11}Li(d,^{3}He) data, the blue line is the theoretical line of a 1.2 MeV state of ^{10}He. The green line indicate the ^{8}He+n+n threshold.*

The ^{10}He was fitted using such convolutions. However, the fit procedure lead to $\Gamma = 0$ MeV. This observation is understood as a consequence of the energy resolution of the set-up around 1 MeV (σ) that forbids the determination of the natural width of the state.

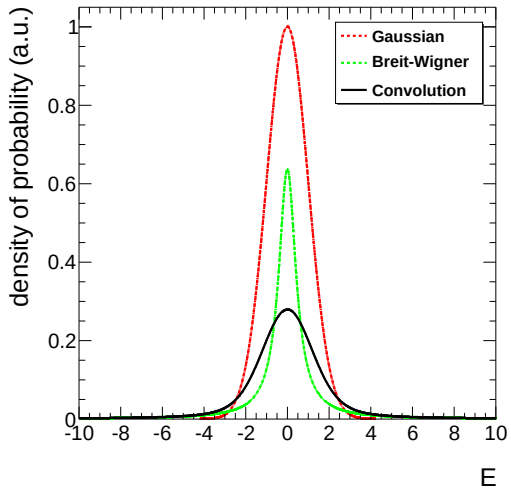

Figure 5.12: *Convolution (black) of a Breit-Wigner (green) of $\Gamma = 1$ MeV with a Gaussian function (red) of $\sigma = 1$ MeV.*

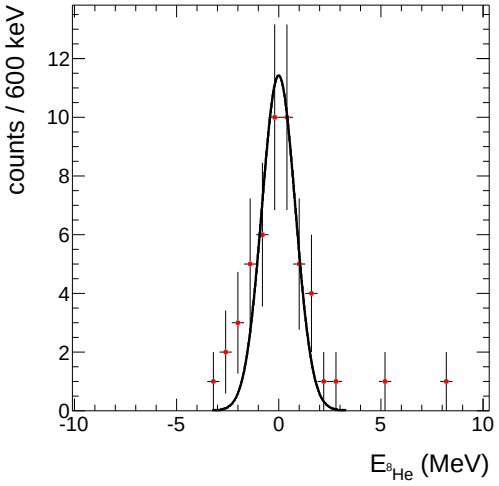

Figure 5.13: *Energy spectrum obtained for the $^9Li(d,^3He)^8He$ reaction. The black line is a fit of fixed 818 keV width that gives E_{gs}= 2.7±196 keV.*

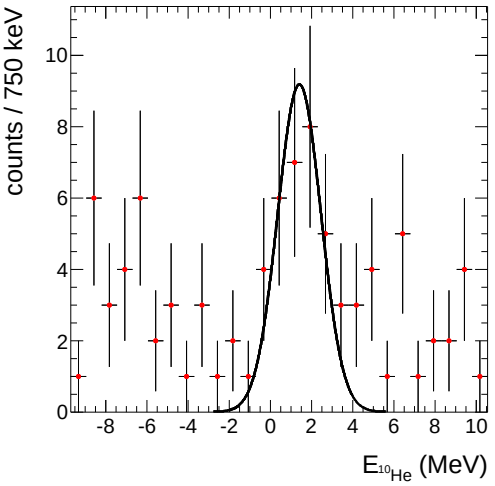

Figure 5.14: *Energy spectrum obtained for the $^{11}Li(d,^3He)^{10}He$ reaction. The black line is a fit of fixed 1050 keV width that gives E_R= 1.4±0.3 MeV.*

Carbon background

The data accumulated using the carbon target with ^{9}Li beam gives almost no contribution, demonstrating the quality of the identification of both ^{3}He and ^{8}He. As explained above, the mixing of ^{8}He and ^{6}He leads to an important background contribution in the ^{10}He case, as shown in Fig.5.15.

The Carbon background was estimated using data accumulated with a 1 mg/cm^2 thickness for both beams. Spectra were extracted using the exactly same gates as for the CD2 target. The number of events in a bin of excitation energy is given by :

$$N_C = N_{detected}(C) \cdot \frac{N_{Beam}(C)}{N_{Beam}(CD2)} \cdot \frac{e_C}{e'_{CD2}} \tag{5.22}$$

For the ^{9}Li beam, only one event was measured in the high excitation energy region. More counts have been measured with ^{11}Li beam but statistics is quite low as can be seen in fog.5.15. The superposition of the normalized spectrum on Carbon target and the ^{10}He spectrum is presented in Fig.5.16. Clearly the contribution of the Carbon from the CD_2 target does not explain the observed structure.

Once normalized, the two spectra can be superimposed to get an idea of the contribution. However, the statistics in the original spectra is rather low and the statistical error bars large (see Fig.5.15), therefore the shape of the distribution is strongly influenced by the statistics and the two histograms can not be subtracted. However a quantitative study can be performed dividing the spectra in three region of interest (cf Fig.5.16), where the density of count for the CD_2 and ^{12}C could

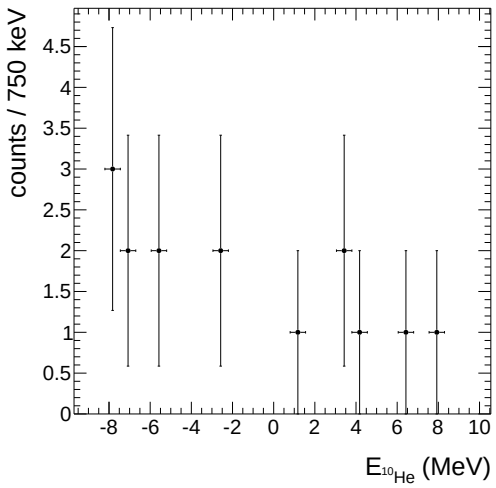

Figure 5.15: *Excitation energy contribution to the ^{10}He spectra obtained using data accumulated with a carbon target before normalization.*

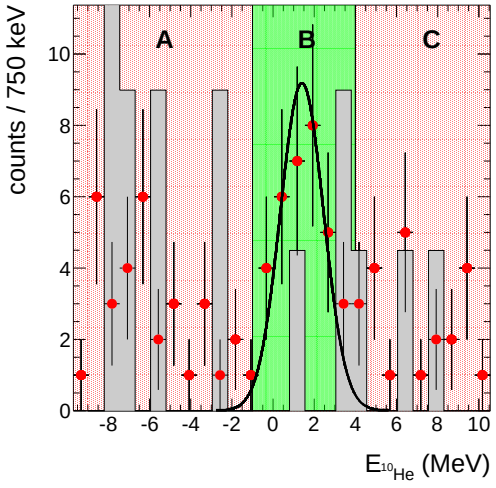

Figure 5.16: *The ^{10}He excitation spectra and the normalized carbon contribution (gray histogram after normalization). The spectra can be divided in three area, (A) the negative energies region, (B) the region of interest and (C) the high energies region.*

be extracted. The obtained results after normalization are shown in Table 5.1. The obtained value show clearly that the number of count in the A region are compatible with a carbon contribution while the B region present an increase of statistic explained only by reaction on the deuterium.

	A	B	C
CD_2	4(1)	6(1)	4(1)
^{12}C	5(1)	2(1)	2(1)
$CD_2/^{12}C$	1(1)	3(1)	2(1)

Table 5.1: *Number of counts per MeV for the three region defined in Fig.5.16*

Moreover, the angular distributions associate with the different regions, and presented in Fig.5.3.1, shown different trend for A and B region. This indicate that the observed count are not coming from the same physical process.

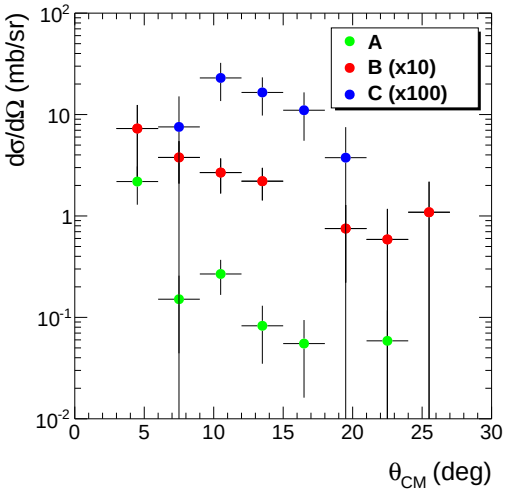

Figure 5.17: *The angular distributions obtained for the three regions described in Fig.5.16. The angular distributions has been multiply by 1, 10, and 100 for respectively A, B and C region in order to clarify the figure. The trend of the angular distribution associate with region A is very different, especially at small angle, of the one of region B.*

5.3.2 Differential cross-sections

The angular distribution for the ^{9}Li(d,^{3}He)^{8}He$_{gs}$ is obtained after setting the energy gate -2 $\leq$ E$_{^{8}He}$ $\leq$ 2 MeV range. It is presented in Fig.5.18. The distribution associated with the first resonant state of the ^{11}Li(d,^{3}He)^{10}He$_{1.4\ MeV}$ is obtained using the -2 $\leq$ E$_{^{10}He}$ $\leq$ 4 MeV gate.

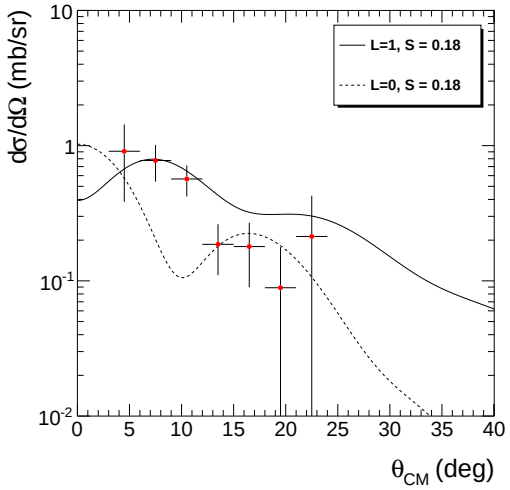

Figure 5.18: *^{9}Li(d,^{3}He)^{8}He differential cross-section compared to DWBA calculation. The normalization gives a spectroscopic factor of 0.18 .*

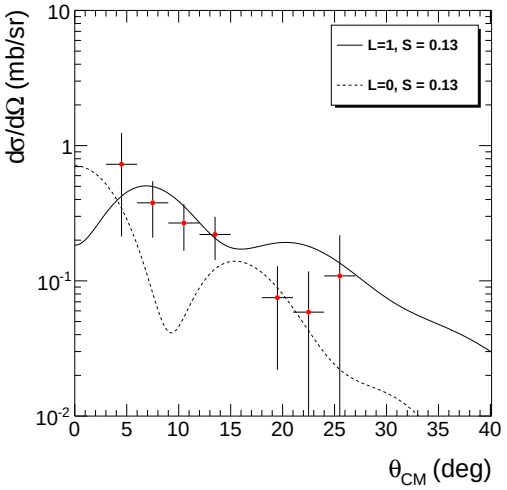

Figure 5.19: *^{11}Li(d,^{3}He)^{10}He differential cross-section compared to DWBA calculation. The normalization gives a spectroscopic factor of 0.13 .*

The comparison with DWBA calculations using DAE potential in the entrance channel and B&G potential in the outgoing channel is presented for L=1 and L=0

case. A first qualitative observation is the incompatibility of the data with a L=0 calculation, showing a strong minimum where the data are maximum. On the other hand, the shape of the differential cross-section is relatively well reproduced by the L=1 calculations. This is in agreement with the pickup of a proton from the $0_{p_{3/2}} shell$.

In both cases the L=1 calculation does not reproduce correctly the shape of the second maximum and over estimate its amplitude. This is stronger in the ^{10}He case and possibly due to the optical potentials used in the analysis. Their parameters are summarized in tab.5.2. Hence the extraction of the spectroscopic factor is done by minimization procedure with the points of the first maximum.

Spectroscopic factor were then extracted using the standard normalization procedure. Values of C^2S=0.18 and C^2S=0.13 were obtained for ^{8}He and ^{10}He respectively.

^{9}Li(d,^{3}He):

Pot.	r_c	V	r_V	a_V	W	r_W	a_W	W_D	r_D	a_D	V_{so}	r_{so}	a_{so}
DAE	1.3	60.97	1.17	0.84	9.55	1.17	0.84	5.63	1.28	0.67	4.00	1.07	0.66
B&G	1.3	159.9	1.2	0.72	30.7	1.4	0.88	0	0	0	0	0	0

^{11}Li(d,^{3}He):

Pot.	r_c	V	r_V	a_V	W	r_W	a_W	W_D	r_D	a_D	V_{so}	r_{so}	a_{so}
DAE	1.3	60.89	1.17	0.84	9.55	1.17	0.84	5.63	1.28	0.68	4.00	1.07	0.66
B&G	1.3	164.9	1.2	0.72	35.1	1.4	0.88	0	0	0	0	0	0

Table 5.2: *Parameters used for the DWBA calculations of the entrance potential (DAE) and the outgoing potential (B&G). The potential depth are given in MeV, the radius and diffusivity in* $fm \cdot A^{\frac{1}{3}}$.

The radius of the form factor used in the DWBA calculation is not well known in the case of a (d,^{3}He) reactions. The above calculation uses a radius R_{ff} = 1.25 fm. In order to check the sensitivity of our results upon this value we evaluated the spectroscopic factor S for different value of R_{ff} in the 1.1-1.4 fm range. The results are presented in Fig.5.20.

The radius of the form factor R_{ff} has a significant influence on the value of the spectroscopic factor. As mentioned above, the standard value R_{ff} = 1.25 fm was used in our DWBA evaluations for the radius of the Wood-Saxon potential for the form-factor calculation. When R_{ff} is varied in the range 1.1-1.4 fm it give in the $\langle ^9\text{Li}|^8\text{He}\rangle$ case a variation of $\pm$0.05. In the case of $\langle ^{11}\text{Li}|^{10}\text{He}\rangle$ the variation is $\pm$0.03.

The error bars were estimated by taking into account the statistical error, the error due to the choice of the optical potentials (evaluated to 25%) and the error associated with the indetermination of R_{ff} (20%). It gives the final value for the overlap of $\langle ^9\text{Li}|^8\text{He}\rangle$, S=0.18(8) and for $\langle ^{11}\text{Li}|^{10}\text{He}\rangle$, S=0.13(6). Because the target thickness has been adjusted to reproduce correctly the ground state of ^{9}Li

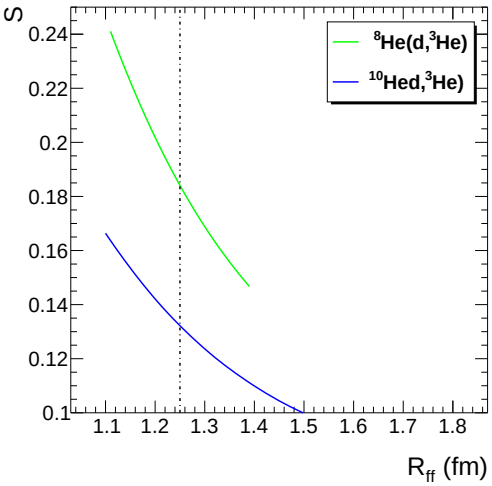

Figure 5.20: *The spectroscopic factor deduced from the differential cross-section of $^{8}He(d,^{3}He)$ (green) and $^{10}He(d,^{3}He)$ reaction plotted versus the form factor radius R_{ff}. The usual value for this parameter is 1.25 fm, and represented as a dashes line on the plot. The spectroscopic factor is sensible to the R_{ff} value and is the main contribution the error bars is the evaluation of its value.*

and ^{8}He a systematic error of 26% should be added, giving for $\langle^{9}\text{Li}|^{8}\text{He}\rangle$ the value of S=0.18(8)(9) and for $\langle^{11}\text{Li}|^{10}\text{He}\rangle$ the value of S=0.13(6)(6).

5.4 Excited states of ^{10}He

Higher energy resonant states may decay in ^{6}He+4n or ^{4}He+6n, therefore they can be studied only using ^{6}He and ^{4}He gates in the zero degrees plastic telescope. An important background exists and therefore the extraction of those states is difficult. However we managed to identify two structures in the energy range of interest as visible in Fig.5.21.

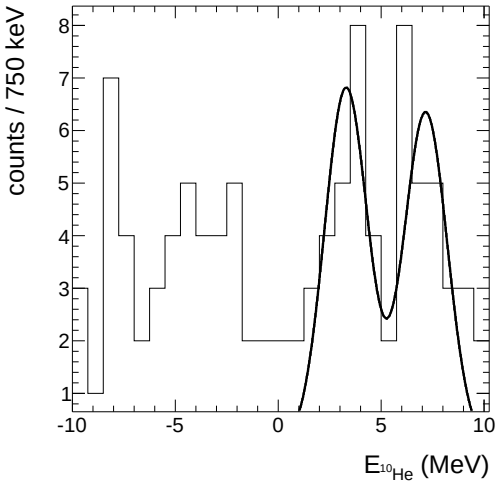

Figure 5.21: *The energy spectrum of ^{10}He obtained in coincidence with ^{6}He in the zero degrees plastic. The black line is the result of a fit by the sum of two Gaussian whose widths, positions and amplitude were free parameters. The fit gives a first state at 3.3(3) MeV and a second state at 6.3(4) MeV.*

These two structures are centered at energies 3.3(3) MeV and 6.3(4) MeV, with a width close to the value given by the simulations, to be compared to the peaks extracted in the double-charge exchange experiment of Ostrowski *et al* [OBG+94]

(see Fig.1.8) located at 4.31 MeV and 7.87 MeV respectively. The strong background and low statistics makes hazardous the extraction of angular distributions. One can not the absence of structure in the -2 to 2 MeV region.

5.5 Discussion

The present results give a first hint of the behavior in the region of interest, however further investigation of the data, using more sophisticated models of reactions to have a better description of the observed angular distribution is needed. Still, we can make a few observations.
N.K. Timofeyuk, in [Tim10], performed an extensive study in the light nuclei region using the inhomogeneous equation (see App.B for details) to predict the overlap wave functions of $\langle$A|A-1$\rangle$ nuclei and the associated spectroscopic factors. The latter show systematic deviation from the corresponding shell-model values. In the case of the $\langle^{9}\mathrm{Li}|^{8}\mathrm{He}\rangle$ the spectroscopic factor obtained from the inhomogeneous equation is 0.385, to be compared with a value of 0.935 in the corresponding shell-model. This tends to show that more correlations are taken into account in the inhomogeneous equation evaluation. The value of 0.18(8) extracted in our study is even lower.

The ^{10}He first resonant state position has been confirmed at $E_R = 1.4 \pm 0.3$ MeV above the ^{8}He+n+n threshold. No calculation exist on the $\langle^{11}\mathrm{Li}|^{10}\mathrm{He}\rangle$ overlap, and the very small spectroscopic factor found in the present work suggest that the ^{10}He structure is very different from the one of ^{11}Li with an overlap of 0.13$\pm$0.03. This information is of first importance in our understanding of the halo formation mechanism. As explained in [PBVB09], the neutron halo binding mechanism in ^{11}Li could be understood as a phonon exchange through the polarization of the ^{9}Li core. The removal of a proton from this core could vanish the attractive potential between the two valence neutrons and lead to an unbound structure.

Combined with existing results [WSR^{+}08] obtained for $\langle^{7}\mathrm{Li}|^{6}\mathrm{He}\rangle$ and $\langle^{8}\mathrm{Li}|^{7}\mathrm{He}\rangle$ ground-state overlaps, the plot of evolution of experimental spectroscopic factors for $\langle^{A}\mathrm{Li}|^{A-1}\mathrm{He}\rangle$ up to the neutron dripline can be deduced, it is presented on Fig.5.22.

A clear decreasing trend is observed when going far from stability. This indicates that the structural changes when going from a ^{A}Li isotope to the corresponding $^{A-1}$He are becoming more and more radical far from stability.

Our spectroscopic factors have been extracted in a DWBA analysis using standard form-factors. when available, it will be of great interest to check if the above conclusions remain with ab initio form-factors, and to better understand the origin of this trend.

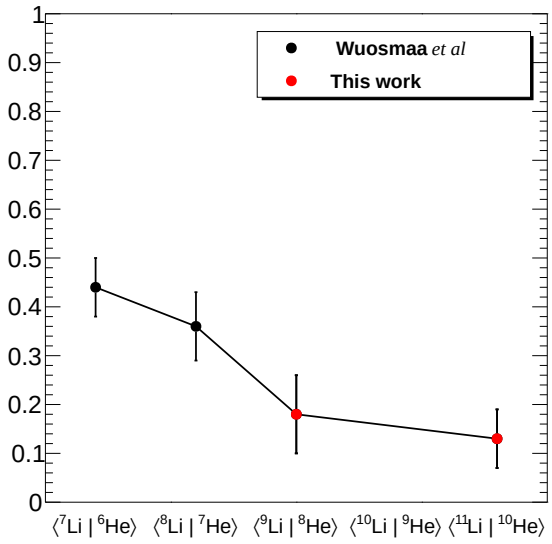

Figure 5.22: *Behavior of the $\langle A,Z|A\text{-}1,Z\text{-}1\rangle$ overlap for Lithium isotopes when going away from stability. The experimental value for the $\langle {}^{7}Li|{}^{6}He\rangle$ and$\langle {}^{8}Li|{}^{7}He\rangle$ come from [WSR+08]. The ^{10}Li being unbound no data are available for the $\langle {}^{10}Li|{}^{9}He\rangle$. The black line is a guide to the eyes.*

Conclusion

In this work we have revisited the spectroscopy of the unbound ^{10}He by means of the ^{11}Li(d,^{3}He) reaction at 50 AMeV studied in missing mass method with the MUST2 array at the RIPS beam line of RIKEN.

The experimental part of this study relies on new detection set-up using very thin silicon detectors of large area. For the first time, the applicability of these detectors, in conjunction with high granularity position sensitive detectors, was proved. The methodology used in the data analysis, *i.e.* the thickness determination and correction, was implemented successfully.

The transfer reaction approach led to clear results on the ^{10}He first resonant state position, found in this work at 1.4(3) MeV, in agreement with most of the previous experimental works on ^{10}He. No evidence was found in favor of the predicted narrow resonance near the ^{8}He+n+n threshold. More importantly, the extraction of a spectroscopic factor, hardly obtained from other reaction mechanisms, allows a strong conclusion on the $\langle^{11}\text{Li}|^{10}\text{He}\rangle$ overlap, found to be 0.13(3). This value sheds light on the significant differences existing between the ^{10}He barely unbound system and the loosely bound ^{11}Li. The role played by the ^{9}Li core in the binding mechanism of the neutron halo is here expressed.

Additional data obtained using ^{9}Li beam offer the opportunity to discuss the evolution of the wave function overlaps when going away from stability. The significant decrease of the spatial overlap denonstrates how the exotic nuclei exhibit very specific structures that can not be described by a standard mean field, shell model-like, approach. Our work provided differential cross-sections that can be used as direct benchmark of our understanding of the microscopic structure of nuclei. *Ab initio* calculations for this region of mass are anticipated within this scope.

In the near future, the ^{10}He could be studied through another kind of direct reaction, namely the α-cluster quasi-free scattering. Taking advantage of the high rate of the ^{14}Be beam now available at RIKEN/RIBF, states in the ^{10}He could be populated the the ^{14}Be(p,pα) reaction. The large acceptance spectrometer SAMURAI would be a great advantage to study the various decay channels, contrary to the present study where the detection of the heavy residue with a plastic telescope was clearly a limitation.

The development of tool dedicated to simulations and analysis, NPTool, also

play an important role in the approach of this experiment. The field is moving towards powerful machines for beams production and new detections system with many channels such as the GASPARD+PARIS γ-particle detector setup, that will be used for the study of direct reaction at SPIRAL2. This will imply more complex analysis and urge for proper and standardised analysis and simulations software, of which NPTOOL can represent a starting point.

Appendix A

NPTool

A.1 Introduction

The simulation (see chap.3) aimed initially to define the best set-up for the present experiment. Various parameters have been taken into account, from detector position to material used in the target or the plastic scintillator. Since the particle of interest may decay in various channel, the simulations have to deal with all those cases. A new tool, NPTool, has been designed to fit these modularity needs, both on event generator and geometry. The development of NPTool, both on analysis part and simulation took around one year and half for the first version, since, a few releases have been published, increasing operability, portability and ease of use.

The core of the project is a C++ library, NPLib, that hold classes design within the nuclear physicist scope. Two body kinematics, energy loss, and data handling, can be used within NPTool, or in any other users program (including root macro), allowing a variety of application.

Today's and tomorrow's challenge in nuclear physics is about dealing with complicate set-up and a large number of channels. The community needs efficient tools that allow to solve the rising problem of data analysis and detection understanding. New detection systems, like AGATA or GASPARD, means a complete change in our approach of extracting relevant information from the large amount of data collected during experiments.

A.2 Methodology

NPTool aimed at providing an universal framework to develop Geant4 simulation of detectors and data analysis using the CERN ROOT libraries. Basically the philosophy is to help physicist to develop their detector geometry and analysis in an homogeneous way so that they can mix their work when needed without doing any modification. In NPTool every detector are treated on the same foot, simulation and analysis of heterogeneous (different kind of detector) experimental set-up is as easy as homogeneous set-up (only one kind of detector). Also, nearly every parameter, from the reaction studied, to the position and configuration of detectors,

can be set-up using a couple of human-readable configuration files. Predicting performances of a complex setting of detectors by taking into account various physics aspects is a hard task in which every aspect needs to be treated carefully. Nuclear physics experiments tend to look at more and more exotic physics cases that lead us to have more and more complex set-up and strong physical background. NPTool is developed in the same spirit as many project from High Energy Physics, and more generally, free software. The main idea is to mutualize skills and works in a common space. NPTool is distributed under the General Public License version 3 (GPLv3) and can be copied, distributed and modify the project freely.

The base of the methodology is to segment the code in specific purpose objects. The powerful C++ language is especially suited for this and as much as possible the offered possibilities are used. For each specific task, a *class* object is implemented, owning it's own variables and methods. The interplay between the different objects is described in the following part.

A.3 Version control

Because NPTool aimed to be a community tool, with many contributors working in parallel the project adopted at its early stage a version control methodology. Version control, also known as Revision control and source control, aimed to managed the various source code of the project through the assistance of a software keeping track of the modification. Each version of the code is stored in the repository and receives a version number as presented in Fig.A.1. Developers add a version of the software performing a *commit*, the version control software add to the repository only the fraction of the code that changed with respect to the previous versions.

The repository is stored on a server a IPNOrsay (`ipnvcs.in2p3.fr`), in read only version for non registered users. Monotone is a free distributed version control system, among other like svn or cvs for the most common. We chose to use Monotone to manage our project because it was offering to perform commit on a locally stored data base, allowing to work even without connection to the repository server. At every commit, the developer must also write a small abstract of the change and the aim of the changes.

The aim is to encourage correct programming behavior within the collaboration, namely frequent committing, per review evaluation, ... This approach has been successfully adopted in large scale software project (ROOT, Linux,...) and gives excellent results.

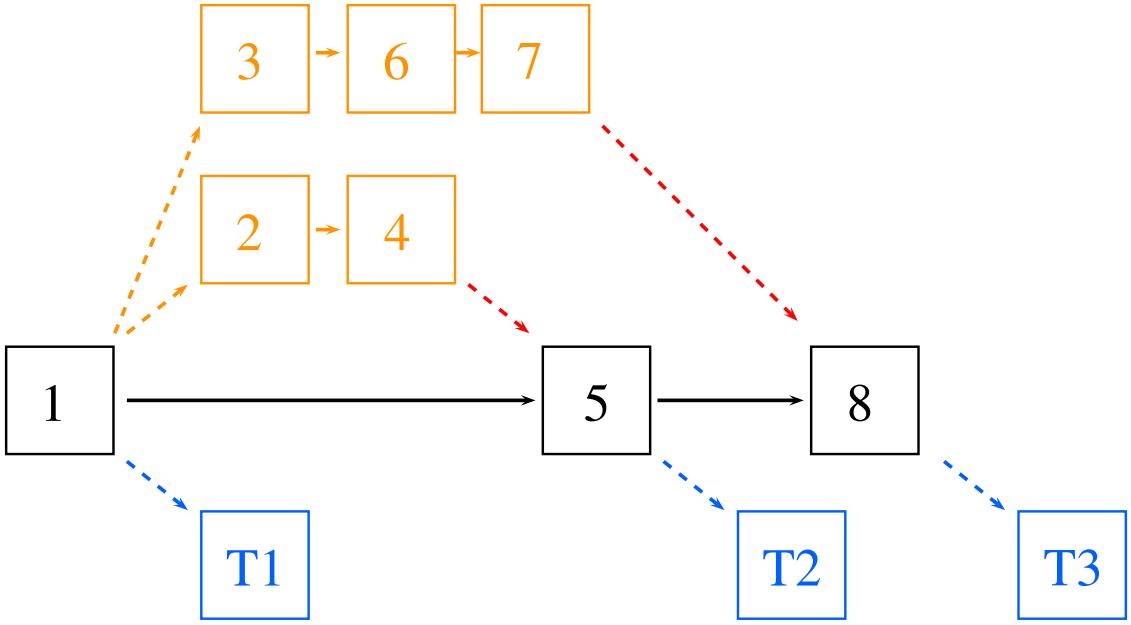

Figure A.1: *Version control repository architecture: The trunk (black) contain fully functional versions of the code. Development are performed in branches (orange) and merged (red) to the trunk when finished. For each version of the trunk, a tag (blue) is defined, allowing the user to find the desired version easily in the repository.*

A.4 NPlibrary

The core of NPTool is the NPlibrary that regroups various classes used in the different part of the code, or with user macro. Most of those classes are describing the way data are stored in Root TTree, but some tools are also provided.

A.4.1 Physics tool: NPNucleus, NPReaction, NPEnergyLoss

NPNucleus

This very simple class implemented various method allowing to define a nuclei and parse a table to define its mass. The table used actually is the Audi mass table of 2003 [AWT03]. The table contain various information, such as mass excess, spin parity of ground state, ... The class allows to instantiate a nuclei only using a string name, for instance "4He" for α-particle, the class will then read the available data in the mass table and load them in the memory. A set of function allows the user to compute the mass and access those information, but also to change it. The user's change will not be saved in the table, and will be effective only in the limited scope of the execution.

Note that the mass given (in the 2003 Audi table) for the unbound nuclei corresponds to the first resonance state of this nuclei.

NPReaction

This class deals with two body kinematics. It basically contains four NPNucleus, and computes the associated variable such as the reaction Q value. In addition, kinematic calculation can be performed using the beam energy. The class is designed to be used in both simulation and analysis environment assuring a consistent way of working. A method, *KineRelativistic*, allowing to compute the laboratory angles and energies of the outgoing particle, giving the center of mass angle, is used for simulation purpose. On the other hand, the method *ReconstructRelativistic* allowing to deduce excitation energy of the nuclei of interest using as inputs the laboratory angle and energy of the other nuclei, is used for analysis purpose.

NPEnergyLoss

Designed to handle energy loss dE/dx table and to perform various calculations, this class find application at every stage of the experiment. It is successfully used in the fully automatic calibration algorithm of the MUST2 DSSD (see Sec.4.4.1) to evaluate the energy loss of α-particles in the dead layer, or in the NPAnalysis project to correct energy loss in the target. The class is able to read file coming from the LISE++ program, the SRIM program and the NPSimulation program. The program used a slicing algorithm performing calculation on infinitesimal path of the particle and interpolation of the $dE/dx(E)$ function. It can slow down particle crossing a thickness of material e using n slices of material:

$$E_{final} = E_{intial} - \int_{\delta=0}^{e} \frac{dE}{dx}(E_\delta)dx \approx E_{intial} - \sum_{1}^{n} \frac{dE}{dx}(E_n) \cdot \frac{e}{n} \tag{A.1}$$

In the same way, one can compute the initial energy of a particles crossing a known thickness of material:

$$E_{initial} = E_{final} + \int_{\delta=0}^{e} \frac{dE}{dx}(E_\delta)dx \approx E_{final} + \sum_{1}^{n} \frac{dE}{dx}(E_n) \cdot \frac{e}{n} \tag{A.2}$$

One needs to use a sufficiently large n so the integral approximation by a sum is valid. On the other hand, the calculation time increase linearly with n. Good results are obtained for $e/n \sim 1 - 0.1\mu m$

Finally the class allows to evaluate the initial energy using the ΔE and the material thickness e: using a dichotomic algorithm trial energy E_T of the particle is tested until the associate ΔE_T matched ΔE.

A.4.2 Handling tool: VDetector, DetectorManager, CalibrationManager

VDetector

The VDetector class is a virtual one. *Virtual classes* could be seen as template objects. The virtual class defined a whole set of properties, like members and

methods which can be overridden by subclasses through inheritance mechanism. Therefore, the virtual classes are a powerful object to define general way of coding. The VDetector class is a template for all kind of detector object, defining the features each of them need to implement, in its own way:

Features:

DetectorData A pointer to the TDetectorData, containing the raw data

PhysicsData A pointer to the TDetectorPhisics, containing the physical data

Methods:

ReadConfiguration Reads a NPTOOL input file to configure the detector

AddParameterToCalibrationManager Adds the list of calibration parameters to the calibration manager (see below)

InitializeRootInputRaw Initializes the input branches of Raw data type to the input TChain

InitializeRootInputPhysics Initializes the input branches of Physics data type to the input TChain

InitializeRootOutput Initializes the output branches of Physics data type to the input TChain

BuildPhysicalEvent Builds Physics data using raw data.

BuildSimplePhysicalEvent Builds Physics data using raw data in a fast and approximate way (typically used for online analysis)

ClearEventPhysics Clears the Physics data object

ClearEventData Clears the Raw data object

All detectors are managed by a single entity, the DetectorManager, regardless of their specific nature.

DetectorManager

The DetectorManager hold a single object, a Standard Template Library (STL) vector of VDetector. The DetectorManager is calling the method of all the detectors on the appropriate time. Adding a new detector does not need to implement the associate calls of method , only the methods themselves.

CalibrationManager

The CalibrationManager manage a list of file and a list of parameter. The files are read once to load all the parameters in memory. At any time the detector class can access the calibration parameter through methods and use them. The class is designed to be able to load any order of polynomial calibration parameters.

A.5 NPSimulation

NPSimulation is the Geant4 based part of NPTool. The program rely on Geant4 for managing geometry, tracking, material definition, energy loss table computation, and so on. Geant4 is a *Monte Carlo* based simulation program, where the user can generate particles which are tracked within user-defined volumes and materials. Some specific virtual classes have been developed to provide nuclear physicists with a ready to use dedicated framework. Nuclear physics event generator has been implemented, allowing to simulate most standard physics cases for nuclear structure study. More generator can be easily added to suit nearly any physics inheriting from a virtual class VEventGenerator. At present the following event generator have been implemented:

- Isotropic Source of light ion (from proton to alpha)
- Beam Event of any kind of nucleus
- Transfer Reaction to a nucleus's bound state
- Transfer Reaction to an unbound state decaying by phase space
- Pure phase space event

These event generators generate charged particles, neutron and gamma, following accurate physics. Kinematic, spatial and energetic beam spread, target position and angle, are taken into account, allowing a deep understanding of the experimental interplay of each parameters. The following methods need to be implemented for an event generator:

ReadConfiguration Reads a NPTOOL input file to configure the event generator

GenerateEvent Performs all the needed calculation and generate Geant4 particles

InitializeRootOutput Initializes the branch need to keep in the output tree the information on the initial state of each generated event

The detection geometry is also of prior interest in simulation making, so various detectors has been implemented with help of various collaborators:

```
%%%%%%%%%%%%%%%%%%%%%%%%%%%%%
% 9Li(d,3He)8He input file
Transfert
Beam= 9Li
Target= 2H
Light= 3He
Heavy= 8He
ExcitationEnergyHeavy= 0.0
ExcitationEnergyLight= 0.0
BeamEnergy= 450
BeamEnergySpread= 0
SigmaX= 3.955
SigmaY= 2.396
MeanX= 0.205
MeanY= 1.76
SigmaThetaX= 0.513
SigmaPhiY= 0.7612
CrossSectionPath= Li9(d3He)8He.dat
ShootLight= 1
ShootHeavy= 1
%%%%%%%%%%%%%%%%%%%%%%%%%%%%%
```

Figure A.2: *Example of an input file used to define an event generator, here a transfer reaction, in NPSimulation. Comment line starts with the % character.*

- MUST2
- 20um thick SSSD detector
- Plastic Scintillator
- S1 Silicon annular (Micron)
- W1 Silicon annular (Micron)
- Eden Neutron detector
- GASPARD
- PARIS
- HYDE

All of them derived from the class VDetector, and have the following methods:

ReadConfiguration Reads a NPTOOL input file to configure the detector geometry

ConstructDetector Constructs the Geant4 volume needed for the tracking of the particles

InitializeScorers Scorers are read out objects that store informations on the particles interaction in the associate volume

ReadSensitive Reads out the scorer and fill the output file

InitializeRootOutput Initializes the branch needed in the output file

The input of both a geometry of detection and an event generator allows the user to simulate its experiment. The output of the Simulation is an experimental-like file that can be analyzed just like any experimental data.

NPSimulation is currently used in various laboratory in the world to work on prospect for future detector such as GASPARD and for preparation of upcoming experiments.

```
%%%%%%%%%%%%%%%%%%%%%%%%%%%%%%%%%%%%
GeneralTarget
Target
THICKNESS= 13.1
RADIUS= 45
MATERIAL= CD2
ANGLE= 0
X= 0
Y= 0
Z= 0

%%%%%%%%%%%%%%%%%%%%%%%%%
MUST2Array
%%%%%%% Telescope 1 %%%%%%%
M2Telescope
X1_Y1= 10.85 105.03 146.16
X1_Y128= 22.8 9.84 175.95
X128_Y1= 104.09 105.03 108.76
X128_Y128= 116.04 9.84 138.55
SI= 1
SILI= 0
CSI= 1
VIS= all

%%%%%%% Telescope 2 %%%%%%%
M2Telescope
X1_Y1= -116.04 9.84 138.55
X1_Y128= -22.8 9.84 175.95
X128_Y1= -104.09 105.03 108.76
X128_Y128= -10.85 105.03 146.16
SI= 1
SILI= 0
CSI= 1
VIS= all
%%%%%%%%%%%%%%%%%%%%%%%%%%%%%%%%%%%%
```

Figure A.3: *Example of an input file used to define geometry of detection in both NPSimulation and NPAnalysis. Comment line started with the % character.*

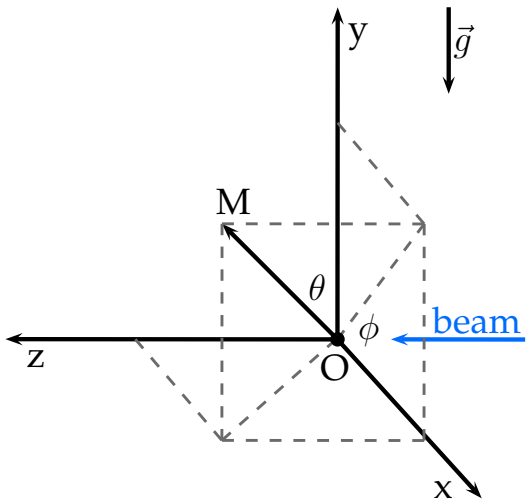

Figure A.4: *The coordinate system used in both NPAnalysis and NPSimulation. The $\vec{g}$ is here to disambiguate the y direction, orthogonal to the floor, in the roof direction.*

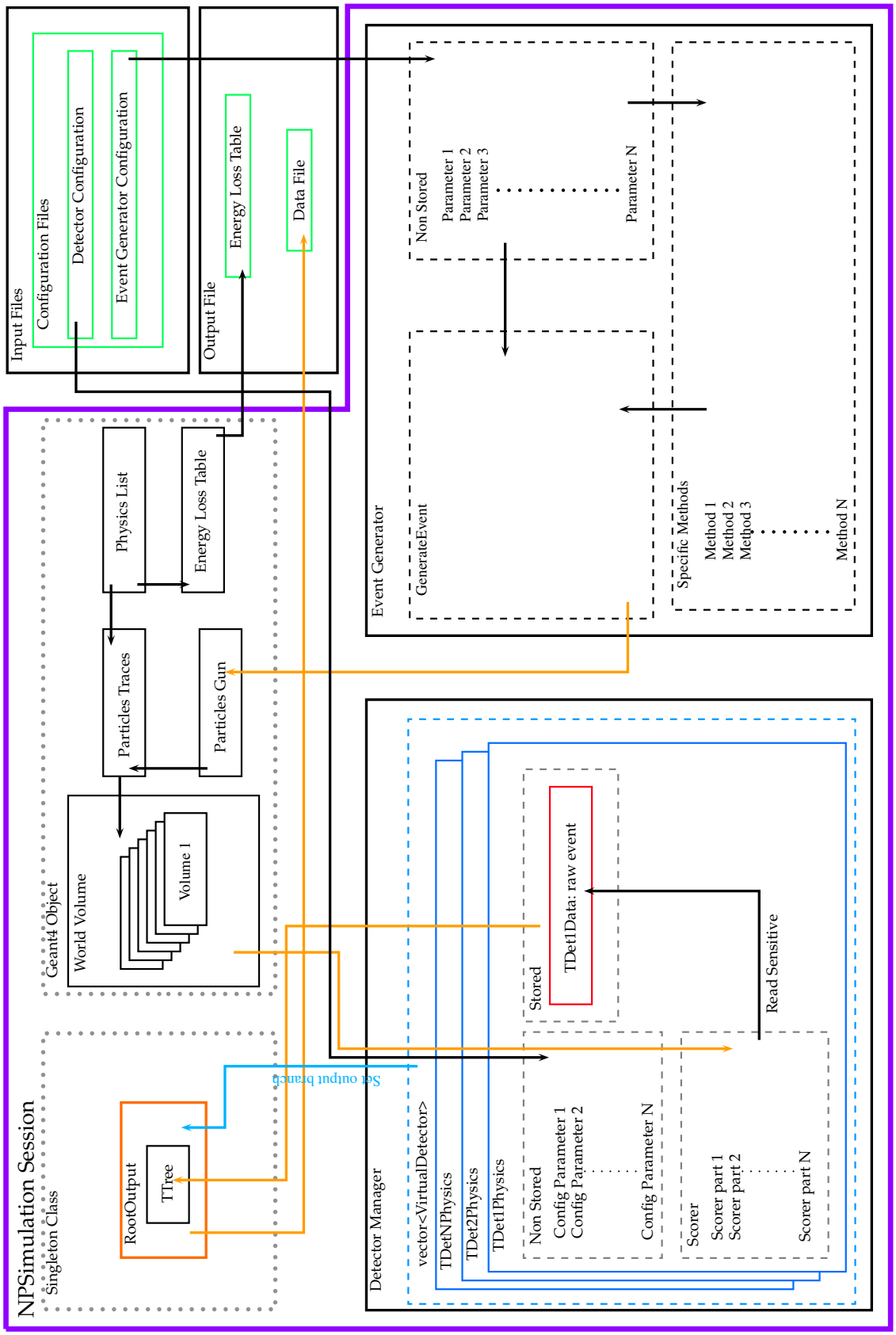

Figure A.5: *Schematic view of the different actors of NPSimulation running.*

A.6 NPAnalysis

NPAnalysis is a ROOT-based software which aims at analyzing experimental data. It's specific architecture rely on the NPlibrary, part of the NPTool package. It is aimed at separate what is, for each detector, common to all experiment and put it a common library. However, because each experiment is unique by definition, users need to create a specific project for each experiment. Once it is done, the common part is automatically called and users just need to code the specific part (energy loss correction, specific data treatment,...). This architecture allowed both a large degree of freedom for analysis, and also a good work mutualisation.

NPAnalysis (or part of it) has been successfully used on different experiment including MUST2 and Spectrometer at GANIL, with VAMOS and Riken, with RIPS and BigRIPS, for offline analysis during the experiment, showing it's adaptivity and efficiency. More recently an experiment on LISE GANIL, used the classes of NPTool in conjunction with the Ganil To Root Utility (GRU) to perform online control and analysis. The transition from the old Fortran-based VisuGAN to the new C++ based VIGRU has been done smoothly during the march-April 2011 MUST2 campaign. The program structure also guarantees a common structure between the different detector and therefore an easier understanding for users.

A.7 Perspective

Through this project, we hope to contribute to the improvement of our methodology in our field. A common and robust way of analyzing data is the best way to lead to a deeper understanding of the nuclear structure. The enthusiasm of contributor and users, as well as the nice result obtain with this tool offer bright perspective to the project.

Many improvements are already planned, leading to an even easy to use version of the tool. Among them the perspective of a website and forum to federate the user-developer community is foreseen. The aim is to obtain fully configurable analysis and simulation classes for all the detection used in the community. The consistency of the approach, as well as the knowledge mutualisation is a decisive step in the our approach of the experimental nuclear structure study.

The increasing number of channels and complexity of our experiments call for fast and effective tool for analysis, while the *do it yourself* methodology should be dropped.

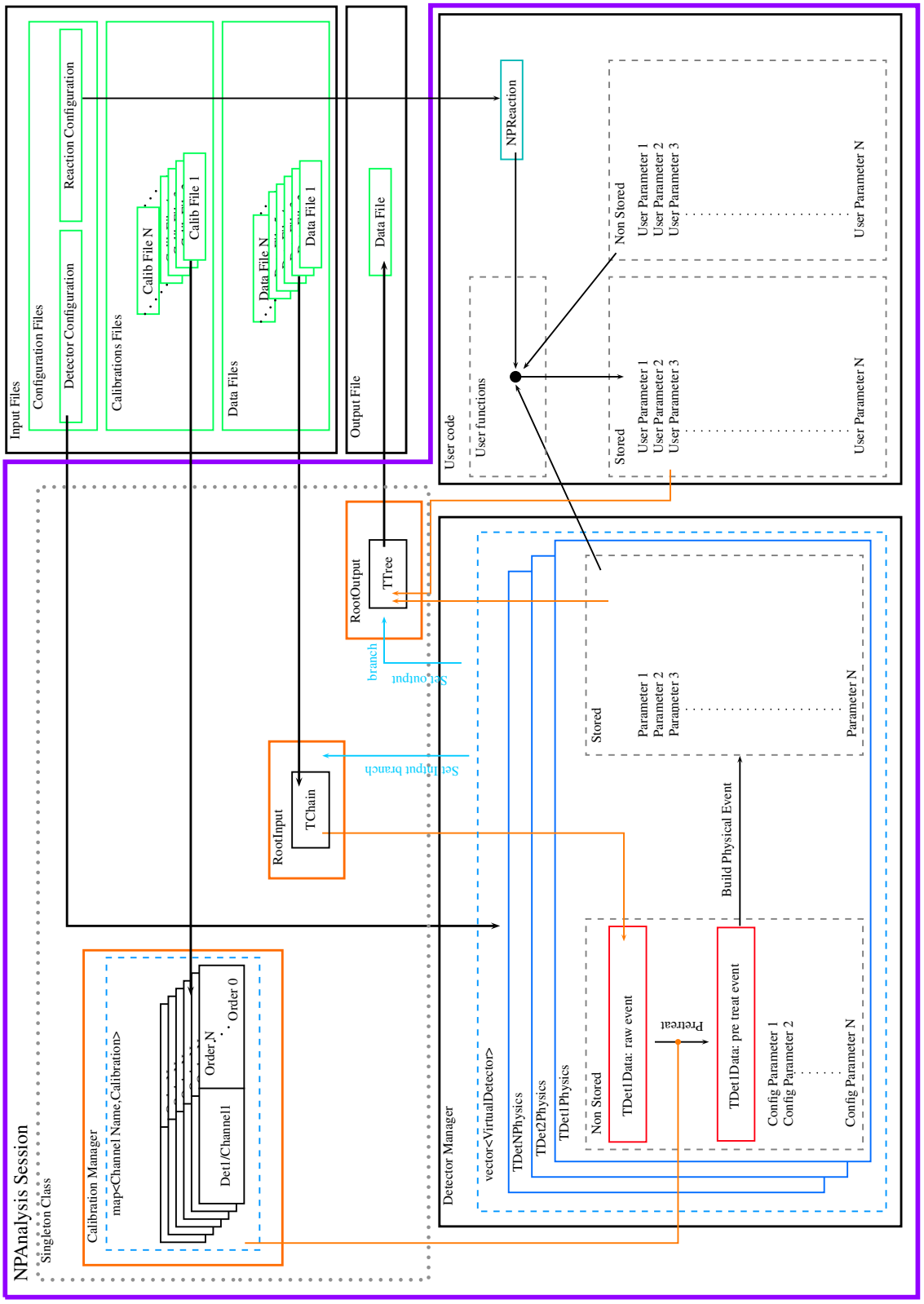

Figure A.6: *Schematic view of the different actors of NPAnalysis project running.*

Appendix B

The inhomogeneous equations

The angular distribution of transfer reaction carried information on the wave function of the transferred particles. To be more specific, among other terms, this distribution is sensible to the overlap of the initial and final wave function:

$$\frac{d\sigma}{d\Omega} \propto S_{AB} S_{ab} \tag{B.1}$$

Where the quantities S_{ij} are defined as :

$$S_{ij} = \int_0^\infty r^2 I_{ij}^2(r) dr = \int_0^\infty r^2 \langle \Psi_i | \Psi_j \rangle dr \tag{B.2}$$

S_{ab} is known in the case of *standard* reactions such as (d,p) or (d,^{3}He). These overlaps are some times considered as shell occupancies, considering the transfer of a single nucleon. In a more general approach, we will consider it only the probe of closeness between A and B nuclei states. Today's modern nuclear models, as described earlier, can gives access to the nuclear wave function and allow the calculation of such overlaps. However, these overlaps calculations, called *direct evaluation*, are model depended and in most phenomenological models, the wave function is given by a linear combination of Slater determinants in truncated spaces. If these model are good at predicting the energies of the states, they are missing informations on the radial shape of the wave functions, especially at long range. Because the transfer reaction occurred preferentially at long range, the small impact parameter favoring other mechanism, these *direct evaluation* is lacking accuracy. Moreover the contribution of the discarded space is generally non-negligible, even for closed shell nuclei. This remark does not stand for the case of *ab inito* calculations, which even if limited to very light nuclei, gives the correct wave functions.

However, there is other way to evaluate $I_{ij}(r)$ without knowledge of the wave functions. This method, called the *inhomogeneous equation* rely on simple hypothesis. One can write the Schrödinger equation for the initial and final state and deduce the following relations between the initial and final wave functions:

$$\begin{cases} H_A|\Psi_A\rangle = E_A|\Psi_A\rangle & (a) \\ H_B|\Psi_B\rangle = E_B|\Psi_B\rangle & (b) \end{cases} \tag{B.3}$$

with H_N expressed as the kinetic T_N energy operator and the nuclear potential of the nuclei V_N:

$$H_N = T_N + V_N \tag{B.4}$$

Multiplying eq.B.3(a) by $\langle\Psi_B|$ and eq.B.3(b) by $\langle\Psi_A|$, we can obtain:

$$\begin{cases} \langle\Psi_B|H_A|\Psi_A\rangle = \langle\Psi_B|E_A|\Psi_A\rangle & (a) \\ \langle\Psi_A|H_B|\Psi_B\rangle = \langle\Psi_A|E_B|\Psi_B\rangle & (b) \end{cases} \tag{B.5}$$

We need now to express H_A in terms of H_B and *vis versa*:

$$\begin{cases} H_A = H_B + T_{rel} + (V_A - V_B) & (a) \\ H_B = H_A + T_{rel} + (V_B - V_A) & (b) \end{cases} \tag{B.6}$$

putting eq.B.5 and eq.B.6 we obtain :

$$\begin{cases} \langle\Psi_B|H_B + T_{rel} + (V_A - V_B)|\Psi_A\rangle = E_A\langle\Psi_B|\Psi_A\rangle & (a) \\ \langle\Psi_A|H_A + T_{rel} + (V_B - V_A)|\Psi_B\rangle = E_B\langle\Psi_A|\Psi_B\rangle & (b) \end{cases} \tag{B.7}$$

Simplified using eq.B.3 relation :

$$\begin{cases} \langle\Psi_B|E_B + T_{rel} + (V_A - V_B)|\Psi_A\rangle = \langle\Psi_B|E_A|\Psi_A\rangle & (a) \\ \langle\Psi_A|E_A + T_{rel} + (V_B - V_A)|\Psi_B\rangle = \langle\Psi_A|E_B|\Psi_B\rangle & (b) \end{cases} \tag{B.8}$$

The two terms of eq.B.8 give the so called *inhomogeneous equation*:

$$\langle\Psi_B|T_A - T_B - E_A + E_B|\Psi_A\rangle = \langle\Psi_B|V_B - V_A|\Psi_A\rangle \tag{B.9}$$

It is important to stress the following points, no assumption on the wave function, nor the potential, has been made so far. The wave function overlap generates by the resolution this equation as by construction the correct shape when the experimental value of $\epsilon = E_A - E_B$ is used. Here, ϵ and $v = V_A - V_B$ is to be understood as the binding energy of the transferred nucleon to the core and the interaction potential of this nucleon with the core respectively.

An extensive study, comparing the results given by the *direct evaluation*, the *inhomogeneous equation* and the *ab initio* calculations to the available experimental data has been done by N.K. Timofeyuk in [Tim10], giving an overview of what can be done in these field.

Appendix C

Electronics

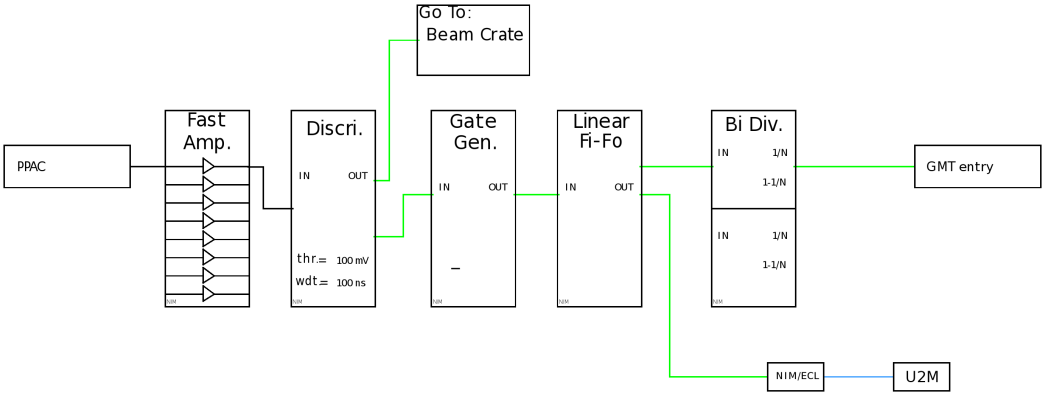

Figure C.1: *PPAC detector electronic chain.*

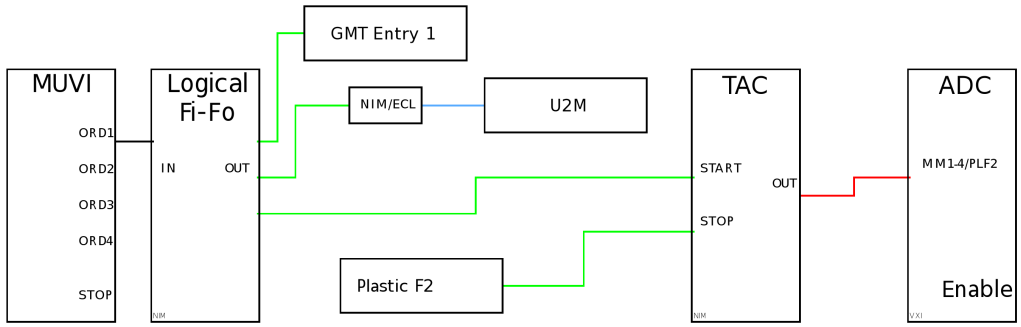

Figure C.2: *MUST2 detector electronic chain.*

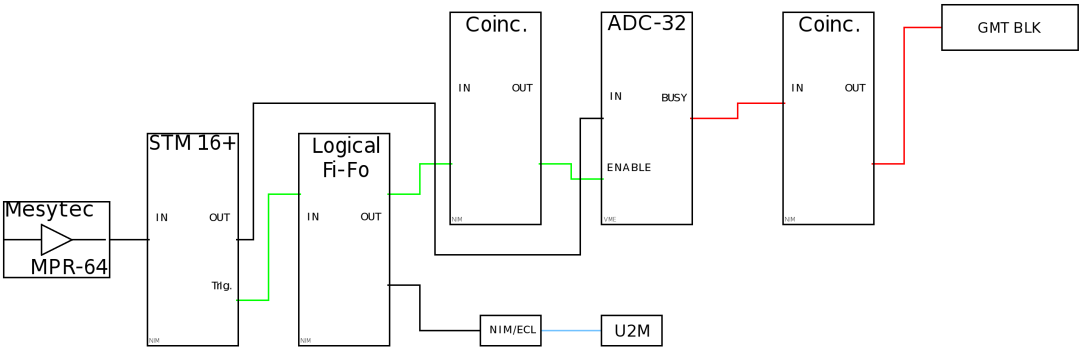

Figure C.3: *20µm SSSD detector electronic chain.*

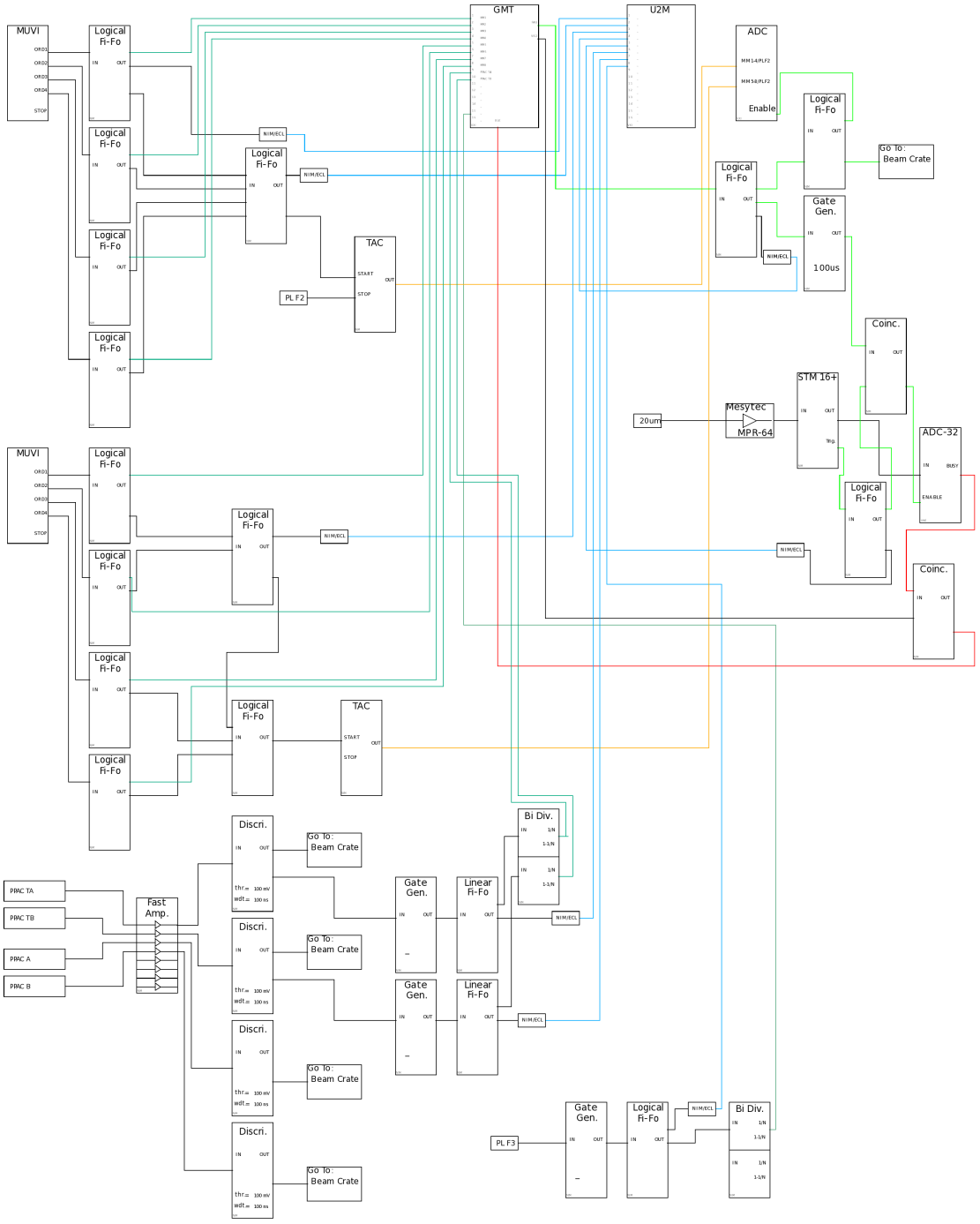

Figure C.4: *Detailed view of the electronic layout.*

Bibliography

[AIO06] S. Aoyama, N. Itagaki, and M. Oi, *Systematic analyses of the $t + t$ clustering effect in he isotopes*, Phys. Rev. C **74** (2006), 017307.

[Aoy02] S. Aoyama, *Theoretical prediction for the ground state of ^{10}he with the method of analytic continuation in the coupling constant*, Phys. Rev. Lett. **89** (2002), 052501.

[Aoy03] Aoyama, *Where is the ground state of ^{10}he?*, Nuclear Physics A **722** (2003), no. 0, C474 – C478.

[AWT03] G. Audi, A.H. Wapstra, and C. Thibault, *The ame2003 atomic mass evaluation: (ii). tables, graphs and references*, Nuclear Physics A **729** (2003), no. 1, 337 – 676, The 2003 NUBASE and Atomic Mass Evaluations.

[BAS+99] Y Blumenfeld, F Auger, J.E Sauvestre, F Marchal, S Ottini, N Alamanos, A Barbier, D Beaumel, B Bonnereau, D Charlet, J.F Clavelin, P Courtat, P Delbourgo-Salvador, R Douet, M Engrand, T Ethvignot, A Gillibert, E Khan, V Lapoux, A Lagoyannis, L Lavergne, S Lebon, P Lelong, A Lesage, V.Le Ven, I Lhenry, J.M Martin, A Musumarra, S Pita, L Petizon, E Pollacco, J Pouthas, A Richard, D Rougier, D Santonocito, J.A Scarpaci, J.L Sida, C Soulet, J.S Stutzmann, T Suomijrvi, M Szmigiel, P Volkov, and G Voltolini, *Must: A silicon strip detector array for radioactive beam experiments*, Nuclear Instruments and Methods in Physics Research Section A: Accelerators, Spectrometers, Detectors and Associated Equipment **421** (1999), no. 3, 471 – 491.

[BH71] H.H. Barschall and W. Haeberli, *Polarization phenomena in nuclear reactions: proceedings, p. 682, by f.d. becchetti and g.w. greenlees*, The University of Wisconsin Press, 1971.

[BJ04] Bjorn and Jonson, *Light dripline nuclei*, Physics Reports **389** (2004), no. 1, 1 – 59.

[BPW11] I. Brida, Steven C. Pieper, and R. B. Wiringa, *Quantum monte carlo calculations of spectroscopic overlaps in $a \leq 7$ nuclei*, *Phys.Rev.C* ***84***(2011), 024319.

[CBB+01] L Chen, B Blank, B.A Brown, M Chartier, A Galonsky, P.G Hansen, and M Thoennessen, *Evidence for an l=0 ground state in ^{9}he*, Physics Letters B **505** (2001), no. 1-4, 21 – 26.

[CCG67] S. W. Cosper, J. Cerny, and R. C. Gatti, *Long-range particles of z = 1 to 4 emitted during the spontaneous fission of ^{252}cf*, Phys. Rev. **154** (1967), 1193–1206.

[DCV80] W. W. Daehnick, J. D. Childs, and Z. Vrcelj, *Global optical model potential for elastic deuteron scattering from 12 to 90 mev*, Phys. Rev. C **21** (1980), 2253–2274.

[Fre07] M. Freer, *The clustered nucleus-cluster structures in stable and unstable nuclei*, Reports on Progress in Physics **70** (2007), 2149–2210.

[GBG+11] G. F. Grinyer, D. Bazin, A. Gade, J. A. Tostevin, P. Adrich, M. D. Bowen, B. A. Brown, C. M. Campbell, J. M. Cook, T. Glasmacher, S. McDaniel, P. Navrátil, A. Obertelli, S. Quaglioni, K. Siwek, J. R. Terry, D. Weisshaar, and R. B. Wiringa, *Knockout reactions from p-shell nuclei: Tests of Ab Initio structure models*, Phys. Rev. Lett. **106** (2011), 162502.

[GGTA+09] M.S. Golovkov, L.V. Grigorenko, G.M. Ter-Akopian, A.S. Fomichev, Yu.Ts. Oganessian, V.A. Gorshkov, S.A. Krupko, A.M. Rodin, S.I. Sidorchuk, R.S. Slepnev, S.V. Stepantsov, R. Wolski, D.Y. Pang, V. Chudoba, A.A. Korsheninnikov, E.A. Kuzmin, E.Yu. Nikolskii, B.G. Novatskii, D.N. Stepanov, P. Roussel-Chomaz, W. Mittig, A. Ninane, F. Hanappe, L. Stuttg, A.A. Yukhimchuk, V.V. Perevozchikov, Yu.I. Vinogradov, S.K. Grishechkin, and S.V. Zlatoustovskiy, *The ^{8}he and ^{10}he spectra studied in the (t,p) reaction*, Physics Letters B **672** (2009), no. 1, 22 – 29.

[Gir11] S. Giron, *Etude de la réaction d'intrt astrophysique ^{60}fe(n,γ)^{61}fe par réaction de transfert (d,p)*, Ph.D. thesis, Université Paris-Sud XI, 2011.

[Gle04] N. Glendenning, *Direct nuclear reactions.*, World Scientific Publishing, Co. Pte. Ltd., 2004.

[GRCD+05] L. Giot, P. Roussel-Chomaz, C. E. Demonchy, W. Mittig, H. Savajols, N. Alamanos, F. Auger, A. Gillibert, C. Jouanne, V. Lapoux, L. Nalpas, E. C. Pollacco, J. L. Sida, F. Skaza, M. D. Cortina-Gil, J. Fernandez-Vasquez, R. S. Mackintosh, A. Pakou, S. Pita, A. Rodin, S. Stepantsov, G. M. Ter Akopian, K. Rusek, I. J. Thompson, and R. Wolski, *Investigation of* ^{6}He *cluster structures*, Phys. Rev. C **71** (2005), 064311.

[GZ08] L. V. Grigorenko and M. V. Zhukov, *Problems with the interpretation of the ^{10}he ground state*, Phys. Rev. C **77** (2008), 034611.

[HJS49] Otto Haxel, J. Hans D. Jensen, and Hans E. Suess, *On the "magic numbers" in nuclear structure*, Phys. Rev. **75** (1949), 1766–1766.

[IMA+00] H. Iwasaki, T. Motobayashi, H. Akiyoshi, Y. Ando, N. Fukuda, H. Fujiwara, Zs. Flp, K.I. Hahn, Y. Higurashi, M. Hirai, I. Hisanaga, N. Iwasa, T. Kijima, A. Mengoni, T. Minemura, T. Nakamura, M. Notani, S. Ozawa, H. Sagawa, H. Sakurai, S. Shimoura, S. Takeuchi, T. Teranishi, Y. Yanagisawa, and M. Ishihara, *Low-lying intruder state in 12be and the melting of the n=8 shell closure*, Physics Letters B **491** (2000), no. 1-2, 8 – 14.

[ITH68] Kiyomi Ikeda, Noboru Takigawa, and Hisashi Horiuchi, *The systematic structure-change into the molecule-like structures in the self-conjugate 4n nuclei*, Progress of Theoretical Physics Supplement **E68** (1968), 464–475.

[JAA+10a] H.T. Johansson, Yu. Aksyutina, T. Aumann, K. Boretzky, M.J.G. Borge, A. Chatillon, L.V. Chulkov, D. Cortina-Gil, U. Datta Pramanik, H. Emling, C. Forssèn, H.O.U. Fynbo, H. Geissel, G. Ickert, B. Jonson, R. Kulessa, C. Langer, M. Lantz, T. LeBleis, K. Mahata, M. Meister, G. Mnzenberg, T. Nilsson, G. Nyman, R. Palit, S. Paschalis, W. Prokopowicz, R. Reifarth, A. Richter, K. Riisager, G. Schrieder, N.B. Shulgina, H. Simon, K. Smmerer, O. Tengblad, H. Weick, and M.V. Zhukov, *Three-body correlations in the decay of ^{10}he and ^{13}li*, Nuclear Physics A **847** (2010), no. 1-2, 66 – 88.

[JAA+10b] H.T. Johansson, Yu. Aksyutina, T. Aumann, K. Boretzky, M.J.G. Borge, A. Chatillon, L.V. Chulkov, D. Cortina-Gil, U. Datta Pramanik, H. Emling, C. Forssn, H.O.U. Fynbo, H. Geissel, G. Ickert, B. Jonson, R. Kulessa, C. Langer, M. Lantz, T. LeBleis, K. Mahata, M. Meister, G. Mnzenberg, T. Nilsson, G. Nyman, R. Palit, S. Paschalis, W. Prokopowicz, R. Reifarth, A. Richter, K. Riisager, G. Schrieder, H. Simon, K. Smmerer, O. Tengblad, H. Weick, and M.V. Zhukov, *The unbound isotopes ^{9,10}he*, Nuclear Physics A **842** (2010), no. 1-4, 15 – 32.

[Jam68] F. James, *Monte carlo phase space*, CERN Academic training programme, 1968.

[Kal10] T. Al Kalanee, *Etude du noyau ^{9}he via la réaction de tranfert d(^{8}he,p) á 15.4 mev/nucléon*, Ph.D. thesis, Université de Caen, 2010.

[KH01] Y. Kanada-En'yo and H. Horiuchi, *Structure of Light Unstable Nuclei Studied with Antisymmetrized Molecular Dynamics*, Progress of Theoretical Physics Supplement **142** (2001), 205–263.

[KII+92] T. Kubo, M. Ishihara, N. Inabe, H. Kumagai, I. Tanihata, K. Yoshida, T. Nakamura, H. Okuno, S. Shimoura, and K. Asahi, *The riken radioactive beam facility*, Nuclear Instruments and Methods in Physics Research Section B: Beam Interactions with Materials and Atoms **70** (1992), no. 1-4, 309 – 319.

[KOF+01] H. Kumagai, A. Ozawa, N. Fukuda, K. Smmerer, and I. Tanihata, *Delay-line ppac for high-energy light ions*, Nuclear Instruments and Methods in Physics Research Section A: Accelerators,Spectrometers,Detectors and Associated Equipment **470** (2001), no. 3, 562 – 570.

[Kun02] P.D. Kunz, *Dwuck4: Zero range dwba*, 2002.

[KYA+94] A. A. Korsheninnikov, K. Yoshida, D. V. Aleksandrov, N. Aoi, Y. Doki, N. Inabe, M. Fujimaki, T. Kobayashi, H. Kumagai, C. B. Moon, E. Yu. Nikolskii, M. M. Obuti, A. A. Ogloblin, A. Ozawa, S. Shimoura, T. Suzuki, I. Tanihata, Y. Watanabe, and M. Yanokura, *Observation of 10he*, Physics Letters B **326** (1994), no. 1-2, 31 – 36.

[KYO+97] T. Kobayashi, K. Yoshida, A. Ozawa, I. Tanihata, A. Korsheninnikov, E. Nikolski, and T. Nakamura, *Quasifree nucleon-knockout reactions from neutron-rich nuclei by a proton target: p(6he,pn)5he, p(11li,pn)10li, p(6he,2p)5h, and p(11li,2p)10he*, Nuclear Physics A **616** (1997), no. 1-2, 223 – 230, Radioactive Nuclear Beams.

[May48] Maria G. Mayer, *On closed shells in nuclei*, Phys. Rev. **74** (1948), 235–239.

[May49] Maria Goeppert Mayer, *On closed shells in nuclei. ii*, Phys. Rev. **75** (1949), 1969–1970.

[Mes60] A. Messiah, *Mécaninque quantique, tome 2'*, Dunod, 1960.

[MKM+97] Miroslav Morhac, Jan Kliman, Vladislav Matousek, Martin Veselsky, and Ivan Turzo, *Background elimination methods for multidimensional coincidence γ-ray spectra*, Nuclear Instruments and Methods in Physics Research Section A: Accelerators, Spectrometers, Detectors and Associated Equipment **401** (1997), no. 1, 113 – 132.

[Mou08] X. Mougeot, *Spectroscopie des noyaux exotiques ^{6}he, ^{7}he avec les télescopes á pistes must2 et le faisceau spiral d'^{8}he*, Ph.D. thesis, Université Paris 7 - Denis Diderot, 2008.

[MU49] N. Metropolis and S. Ulam, *The monte carlo method*, Journal of the American Statistical Association **44** (1949), 335–341.

[NAA+00] A. Navin, D. W. Anthony, T. Aumann, T. Baumann, D. Bazin, Y. Blumenfeld, B. A. Brown, T. Glasmacher, P. G. Hansen, R. W. Ibbotson, P. A. Lofy, V. Maddalena, K. Miller, T. Nakamura, B. V. Pritychenko, B. M. Sherrill, E. Spears, M. Steiner, J. A. Tostevin, J. Yurkon, and A. Wagner, *Direct evidence for the breakdown of the $N = 8$ shell closure in ^{12}be*, Phys. Rev. Lett. **85** (2000), 266–269.

[NQSB09] Petr Navrátil, Sofia Quaglioni, Ionel Stetcu, and Bruce R Barrett, *Recent developments in no-core shell-model calculations*, Journal of Physics G: Nuclear and Particle Physics **36** (2009), no. 8, 083101.

[NVS+06] T. Nakamura, A. M. Vinodkumar, T. Sugimoto, N. Aoi, H. Baba, D. Bazin, N. Fukuda, T. Gomi, H. Hasegawa, N. Imai, M. Ishihara, T. Kobayashi, Y. Kondo, T. Kubo, M. Miura, T. Motobayashi, H. Otsu, A. Saito, H. Sakurai, S. Shimoura, K. Watanabe, Y. X. Watanabe, T. Yakushiji, Y. Yanagisawa, and K. Yoneda, *Observation of strong low-lying $e1$ strength in the two-neutron halo nucleus ^{11}li*, Phys. Rev. Lett. **96** (2006), 252502.

[OA07] Takaharu Otsuka and Daisuke Abe, *Mean field properties of exotic nuclei and the tensor force*, Progress in Particle and Nuclear Physics **59** (2007), no. 1, 425 – 431.

[OBG+94] A.N. Ostrowski, H.G. Bohlen, B. Gebauer, S.M. Grimes, R. Kalpakchieva, Th. Kirchner, T.N. Massey, W. von Oertzen, Th. Stolla, M. Wilpert, and Th. Wilpert, *Spectroscopy of 10he*, Physics Letters B **338** (1994), no. 1, 13 – 19.

[OFU+01] Takaharu Otsuka, Rintaro Fujimoto, Yutaka Utsuno, B. Alex Brown, Michio Honma, and Takahiro Mizusaki, *Magic numbers in exotic nuclei and spin-isospin properties of the NN interaction*, Phys. Rev. Lett. **87** (2001), 082502.

[OSF+05] Takaharu Otsuka, Toshio Suzuki, Rintaro Fujimoto, Hubert Grawe, and Yoshinori Akaishi, *Evolution of nuclear shells due to the tensor force*, Phys. Rev. Lett. **95** (2005), 232502.

[PBRC+05] E. Pollacco, D. Beaumel, P. Roussel-Chomaz, E. Atkin, P. Baron, J. Baronick, E. Becheva, Y. Blumenfeld, A. Boujrad, A. Drouart, F. Druillole, P. Edelbruck, M. Gelin, A. Gillibert, Ch. Houarner, V. Lapoux, L. Lavergne, G. Leberthe, L. Leterrier, V. Le Ven, F. Lugiez, L. Nalpas, L. Olivier, B. Paul, B. Raine, A. Richard, M. Rouger, F. Saillant, F. Skaza, M. Tripon, M. Vilmay, E. Wanlin, and M. Wittwer, *Must2: A new generation array for direct reaction studies*, The European Physical Journal A - Hadrons and Nuclei **25** (2005), 287–288, 10.1140/epjad/i2005-06-162-5.

[PBVB09] G. Potel, F. Barranco, E. Vigezzi, and R.A. Broglia, *Direct observation of the glue pairing the halo of the nucleus* ^{11}*Li*, ArXiv e-prints (2009), 252502.

[PCO+06] S. D. Pain, W. N. Catford, N. A. Orr, J. C. Angélique, N. I. Ashwood, V. Bouchat, N. M. Clarke, N. Curtis, M. Freer, B. R. Fulton, F. Hanappe, M. Labiche, J. L. Lecouey, R. C. Lemmon, D. Mahboub, A. Ninane, G. Normand, N. Soić, L. Stuttge, C. N. Timis, J. A. Tostevin, J. S. Winfield, and V. Ziman, *Structure of* ^{12}Be*: Intruder d-wave strength at* $n = 8$, Phys. Rev. Lett. **96** (2006), 032502.

[Pie05] Pieper, *Quantum monte carlo calculations of light nuclei*, Nuclear Physics A **751** (2005), no. 0, 516 – 532, Proceedings of the 22nd International Nuclear Physics Conference (Part 1).

[Ram09] A. Ramus, *Etude des noyaux instables* ^{19}*o et* ^{25}*ne par réaction de transfert à l'aide du dispositif must2-tiara-vamos-exogam*, Ph.D. thesis, Université Paris-Sud XI, 2009.

[Sat83] G. R. Satchler, *Direct nuclear reactions.*, Clarendon Press, international series of monographs on physics, 68 Ed., 1983.

[SIB+09] D. Suzuki, H. Iwasaki, D. Beaumel, L. Nalpas, E. Pollacco, M. Assié, H. Baba, Y. Blumenfeld, N. De Séréville, A. Drouart, S. Franchoo, A. Gillibert, J. Guillot, F. Hammache, N. Keeley, V. Lapoux, F. Maréchal, S. Michimasa, X. Mougeot, I. Mukha, H. Okamura, H. Otsu, A. Ramus, P. Roussel-Chomaz, H. Sakurai, J.-A. Scarpaci, O. Sorlin, I. Stefan, and M. Takechi, *Breakdown of the* $z = 8$ *shell closure in unbound* ^{12}*o and its mirror symmetry*, Phys. Rev. Lett. **103** (2009), 152503.

[Sid11] Sergey Sidorchuk, *New data on the* ^{10}*he energy spectrum obtained in the reaction* ^{3}*h(*^{8}*he,p).*, International Symposium on Physics of Unstable Nuclei (ISPUN), 2011.

[SJZ09] N.B. Shulgina, B. Jonson, and M.V. Zhukov, *11li structure from experimental data*, Nuclear Physics A **825** (2009), no. 3-4, 175 – 199.

[SP08] O. Sorlin and M.-G. Porquet, *Nuclear magic numbers: New features far from stability*, Progress in Particle and Nuclear Physics **61** (2008), no. 2, 602 – 673.

[SSM+03] S Shimoura, A Saito, T Minemura, Y.U Matsuyama, H Baba, H Akiyoshi, N Aoi, T Gomi, Y Higurashi, K Ieki, N Imai, N Iwasa, H Iwasaki, S Kanno, S Kubono, M Kunibu, S Michimasa, T Motobayashi, T Nakamura, H Sakurai, M Serata, E Takeshita, S Takeuchi,

T Teranishi, K Ue, K Yamada, Y Yanagisawa, M Ishihara, and N Itagaki, *Isomeric 0+ state in 12be*, Physics Letters B **560** (2003), 31 – 36.

[STvG92] H. Sagawa, N. Takigawa, and Nguyen van Giai, *Sum rule study of new vibrational modes of excitation in halo nuclei*, Nuclear Physics A **543** (1992), no. 3, 575 – 588.

[TB68] C. Tschalär and Hans Bichsel, *Mean excitation potential of light compounds*, Phys. Rev. **175** (1968), no. 2, 476–478.

[THH+85] I. Tanihata, H. Hamagaki, O. Hashimoto, Y. Shida, N. Yoshikawa, K. Sugimoto, O. Yamakawa, T. Kobayashi, and N. Takahashi, *Measurements of interaction cross sections and nuclear radii in the light p-shell region*, Phys. Rev. Lett. **55** (1985), 2676–2679.

[Tim10] N. K. Timofeyuk, *Overlap functions, spectroscopic factors, and asymptotic normalization coefficients generated by a shell-model source term*, Phys. Rev. C **81** (2010), 064306.

[vBG+95] W. von Oertzen, H. G. Bohlen, B. Gebauer, M. von Lucke-Petsch, A. N. Ostrowski, C. Seyfert, T. Stolla, M. Wilpert, T. Wilpert, D. V. Alexandrov, A. A. Korsheninnikov, I. Mukha, A. A. Ogloblin, R. Kalpakchieva, Y. E. Penionzhkevich, S. Piskor, S. M. Grimes, and T. N. Massey, *Nuclear Structure Studies of Very Neutron-Rich Isotopes of* $^{7-10}$*He,* $^{9-11}$*Li and* $^{12-14}$*Be via Two-Body Reactions*, Nuclear Physics A **588** (1995), 129–134.

[WSR+08] A. H. Wuosmaa, J. P. Schiffer, K. E. Rehm, J. P. Greene, D. J. Henderson, R. V. F. Janssens, C. L. Jiang, L. Jisonna, J. C. Lighthall, S. T. Marley, E. F. Moore, R. C. Pardo, N. Patel, M. Paul, D. Peterson, Steven C. Pieper, G. Savard, R. E. Segel, R. H. Siemssen, X. D. Tang, and R. B. Wiringa, *Structure of* ^{7}He *by proton removal from* ^{8}Li *with the (d,* ^{3}He*) reaction*, Phys. Rev. C **78** (2008), 041302.

[WT67] S. L. Whetstone and T. D. Thomas, *Light charged particles from spontaneous fission of* ^{252}*cf*, Phys. Rev. **154** (1967), 1174–1181.

[Yuk35] Hideki Yukawa, *On the interaction of elementary particles.*, Proc. Phys. Math. Soc. (Japan) **17** (1935), no. 48.